# Observing the Dark Universe with Weak Gravitational Lensing

Naomi Clare Robertson

Balliol College

University of Oxford

A thesis submitted for the degree of

*Doctor of Philosophy*

Trinity 2019

# Observing the Dark Universe with Weak Gravitational Lensing

Naomi Clare Robertson

Balliol College
University of Oxford

*A thesis submitted for the degree of*
*Doctor of Philosophy*

Trinity 2019

We are now entering into an era of huge cosmological data sets, with observations testing the current paradigm to high accuracy. By combining different probes of cosmology, we can access new information about our Universe and investigate the systematic effects that plague our ability to measure cosmology accurately. In this thesis we use weak gravitational lensing as a tool to measure the large scale structure in the Universe.

First, we present the theoretical framework in which this thesis is set. We then detail the methodology required to measure the cross-correlation between galaxy weak lensing and cosmic microwave background (CMB) weak lensing data sets. In particular we highlight the impact of the complicated nature of galaxy weak lensing data and investigate ways to improve the signal-to-noise of the cross-correlation measurement using simulations.

We measure the CMB lensing/galaxy weak lensing power spectrum using the latest CMB lensing data from the Atacama Cosmology Telescope (ACT) and galaxy weak lensing data from the Kilo Degree Survey (KiDS), making a detection at $5\sigma$ significance. We compare our measured cross-spectrum to the cosmological parameters inferred from the *Planck* and KiDS experiments. We then present fits for the matter density and the amplitude of matter fluctuations, marginalising over the galaxy weak lensing systematic biases. We forecast the expected signal-to-noise using the next data release from ACT and use simulated fields to investigate the impact on estimating cosmological parameters with that data set.

Finally, we measure the masses of clusters selected from ACT CMB data via the Sunyaev-Zel'dovich effect using weak gravitational lensing data from KiDS, making a $20\sigma$ detection of the lensing signal. We present an estimate of the mass bias for a set of stacked clusters as well as the highest signal-to-noise individual clusters. We also describe tests of systematic effects and analysis choices.

# Statement of Originality

The work presented in this thesis was undertaken at the Department of Astrophysics at the University of Oxford between October 2015 and October 2019 under the supervision of Professor Jo Dunkley and Professor Lance Miller. It was funded by a Science and Technologies Research Council studentship. I hereby declare that no part of this thesis has been submitted in support of another degree, diploma, certificate or other qualification at the University of Oxford or elsewhere. Except where otherwise stated, or where reference is made to the work of others, the work in this thesis is entirely my own.

Chapters 2 and 3 present work I led due to be submitted to the Monthly Notices of the Royal Astronomical Society, for which I will be the first author.

Chapter 4 presents work due to be submitted to the Monthly Notices of the Royal Astronomical Society, for which I will be the first author. I led all aspects of this work except the implementation of the halo model which was undertaken by Cristóbal Sifon.

Naomi Clare Robertson, *October 2019*

# Acknowledgements

Firstly I would like to thank my wonderful supervisor Jo Dunkley, whose enthusiasm and optimism meant I always bounced out of every meeting – I have learnt so much over these past four years from Jo and it has always been fun. Also to Lance Miller whose wealth of lensing knowledge provided many interesting insights and valuable discussions. I would also like to thank the fabulous Catherine Heymans, who first introduced me to the field of gravitational lensing and has continued to be a source of brilliant ideas throughout my studies. And to David Alonso, for literally always being on hand to help when things were not working, in the most calm and patient way. I would further like to thank my examiners, Matt Jarvis and Joe Zuntz, for their time and effort spent reading my thesis and an interesting viva discussion.

Thanks must also go to the ACT collaboration, particularly Cristóbal, Nick, Mat, Blake, Andrina, Matt, Omar and Alex, from whom I have learnt so much about CMB science and in the KiDS collaboration Ami, Marika, Joachim, Henk and Elisa. An extra big thank you must go to Alex Amon - another island girl albeit a more tropical one - for not only being my go to lensing guru and making conferences hella' more fun, but also for the supportive chats and cheering me on when I needed it most.

At Princeton, I'm grateful for all the astrophysics graduate students and Polly, who made me feel so at home during my time there. And at Oxford, I'd like to thank Joe for the spicy music suggestions, my dis-functional family at Marlborough Road – Paul, Sergio, Catherine and Sam – and to Marius, Ollie, Nicole and Ben. Also the Balliol crew, Fanny, Leea, Debby, Phil, Rahul, Rob, Claire, Josh, Alban and Mansi for the many adventures in Oxford and further afield. At Oxford a huge thank you to Ashling and Jonathan Patterson – I am certain when I say this thesis would not have been possible without you both.

A thank you to the Mrs Maclean, Flossy MacDonald, Mr Holmes and Louise Dyer who encouraged my interest in science and maths throughout my high school years and always did more than what was required of them to give me the best opportunities.

Throughout my PhD I have been lucky to be supported by Kat, Livi and Claire – the original astro crew – and also the brilliant and hilarious Steph, who has been there from proof reading PhD applications and practice interviews over breakfast, to all the wee messages of encouragement sent across the water.

Thank you to Craig whose hard work inspires me everyday to try my best and always reminds me of where I have come from. And also for the practical stuff like making sure I got sleep, vegetables and fresh air during the last few months of writing.

Finally, a huge thank you to my family – Mum, Dad, Amy, Dave, Nancy, Brèagha, Grandma and Grandpa – who are beyond brilliant. To wee Nancy, for all the cuddles and smiles and my 100 year old Pompa for always taking an interest in my studies of 'astrology'. I thank Amy for the sisterly love and totally geeking out over maths and science with me – you have been my number one role model from day one and I am so grateful I have you to look up to. Lastly but most importantly, I would also like to thank my Mum and Dad who taught me to be curious, aim high, try my best, keep my chin up and never to take anything too seriously. To Mum, for all the pre-exam pep talks, post cards and making sure I always have a Mrs Rimmer's cake in the freezer. And to Dad for reading every essay, report, and application I have ever written, the hours and hours of exam revision testing and the long drives up and down the road.

A' mhuir, tha i ciùin

Tha i fiadhaich, tha i farsainn
Tha i lainn, tha i dìomhair
Tha i gamhlasach is domhainn.
O, ach sinn, tha sinn dall
'S chan eil againn ach beatha
Tog an seòl, tog an ràmh
Gus am faigh sinn astar ann.

*Cearcall A' Chuain*
*Calum agus Ruaraidh Dòmhnallach*

# Contents

# List of Figures

# Chapter 1

# Introduction

In this thesis we are mainly concerned with the large scale properties of the Universe and its evolution. Here, we briefly review the current understanding of the evolution of the Universe – from the Big Bang through to the structure we see today. We then present an overview of weak gravitational lensing, the results of which will be used in this thesis. Finally we report the current status of observational cosmology including experiments and results.

## 1.1 The Cosmological Model

In the currently favoured cosmological model, the Universe began in a Hot Big Bang, 13.8 billion years ago (Planck Collaboration, 2018). It is thought that this was followed by a period of exponential expansion – referred to as inflation (Guth, 1981; Starobinskiĭ, 1979) – making the Universe isotropic, such that the Universe looks the same in all directions, when seen by the late-time observer, at separations which would not have been causally connected in a standard Big Bang model. Within this model, very small irregularities produced by quantum fluctuations were present in the mass distribution. These fluctuations are thought to have been amplified during inflation and became classical perturbations that seeded the Large Scale Structure (LSS) we see in the Universe today (Peebles, 1980; Springel et al., 2005), discussed in section 1.1.2. It is predicted that after inflation, there was a period of reheating followed by the formation of light nuclei which were formed via a process of nucleosynthesis – it is expected that most of the helium-4 in the Universe was produced at this time along with small amounts of deuterium, helium-3 and lithium-7 (Peebles, 1966; Wagoner et al., 1967). After this radiation dominated period, matter became the dominant component. For some time, baryons are expected to still be coupled to photons. It is only once the Universe had expanded sufficiently such that the scattering rate was lower than the expansion rate that ions and electrons combined to produce neutral atoms and the Universe became transparent – we refer to this period as recombination (Peebles, 1968). The photons from this last scattering surface, we see today as the Cosmic Microwave Background (CMB) - an isotropic black-body spectrum of radiation (Dicke et al., 1965; Penzias & Wilson, 1965). After recombination, baryonic matter falls into the gravitational potential wells created by dark matter and the process of hierarchical merging and collapse follows, which ignites the first stars and galaxies and eventually produces the LSS we observe today (Lyth & Liddle, 2009).

Throughout this section we follow the derivations presented in Peacock (1999) and Dodelson (2003).

### 1.1.1 Concordance Model of Cosmology

The concordance model of cosmology is the currently accepted and most commonly used cosmological model. We begin with the Friedmann-Lemaître-Robertson-Walker (FLRW) metric (Friedmann, 1924; Lemaître, 1933; Robertson, 1935; Walker, 1937), which can be used to describe an expanding universe which is both isotropic and homogeneous (the same everywhere) (Liddle, 2003), represented by the line element

$$ds^2 = -c^2dt^2 + a^2(t)\left[\frac{dr^2}{1-kr^2} + r^2(d\theta + \sin^2\theta d\phi^2)\right], \tag{1.1}$$

where $\{r, \theta, \phi\}$ are the spherical polar coordinates such that $r$ is the comoving radial distance. The expansion of the Universe means that in the past the distances between galaxies was smaller than it is now, this is described by the scale factor $a(t)$, and its present day value is set to one such that at earlier times $a < 1$. The curvature of space is described by constant $k$ which is equal to/greater-than/less-than zero for a flat/closed/open geometry of the Universe.

To understand the history of the Universe we need to explain how the scale factor evolves with time. This dependence is determined by the energy density in the Universe. The Hubble rate defines how the scale factor changes and is given by

$$H(t) \equiv \frac{\dot{a}(t)}{a(t)} . \tag{1.2}$$

The present value of $H(t_{\text{now}}) = H_0$ is referred to as the Hubble constant. More generally, the evolution of the expansion of the Universe is derived from Einstein's gravitational field equations and described by the Friedmann equation,

$$\left(\frac{\dot{a}}{a}\right)^2 = \frac{8\pi G}{3}\rho - \frac{kc^2}{a^2} + \frac{\Lambda}{3} , \tag{1.3}$$

fluid equation,

$$\dot{\rho}c^2 + 3H(\rho c^2 + p) = 0 , \tag{1.4}$$

and acceleration equation

$$\frac{\ddot{a}}{a} = -\frac{4\pi G}{3}\left(\rho + \frac{3p}{c^2}\right) + \frac{\Lambda}{3} , \tag{1.5}$$

where $\rho$ is the density, $p$ is the pressure of the fluid content of the Universe and $\Lambda$ is the cosmological constant, which is the energy density of space. The discovery of the accelerated expansion of the Universe (Schmidt et al., 1998; Perlmutter et al., 1999) implied the need for a positive non-zero value of $\Lambda$. Studies have since shown that nearly 70% of the Universe can be accounted for by a supposed 'dark energy' – the cosmological constant is the simplest example of dark energy (Peebles & Ratra, 2003). Here we assume it to be constant, although there are a variety of other dark energy models in which this is not the case (Copeland et al., 2006).

The Friedmann equation can be re-expressed in terms of the Hubble rate as

$$H^2(a) = \frac{8\pi G}{3}\left(\rho_m + \rho_\gamma + \rho_k + \rho_\Lambda\right) . \tag{1.6}$$

Here the density $\rho$ is conveyed as the sum of the energy components in matter ($m$) and radiation ($\gamma$), the density of curvature can be written as $\rho_k = -kc^2/8\pi G a^2$ and the density of dark energy is given by $\rho_\Lambda = \Lambda/8\pi G$.

Accepting the Friedmann equation, there is therefore always a critical density that will generate $k = 0$ making the spatial part of the metric look Euclidean,

$$\rho_c = \frac{3H^2}{8\pi G} . \tag{1.7}$$

A Universe with a density larger than $\rho_c$ will be spatially closed, and a Universe with a density less than $\rho_c$ will be spatially open. The density parameter can then be used to express each component of the energy density in terms of the critical density as

$$\Omega_i(a) = \frac{\rho_i(a)}{\rho_c} . \tag{1.8}$$

If the dependence of the density parameter on the scale factor, and therefore time, is not specified then it is taken to be the present value when $a = 1$. The sum of these components,

$$\Omega \equiv \Omega_m + \Omega_\gamma + \Omega_\Lambda , \tag{1.9}$$

is a crucial cosmological parameter since its value establishes the future of the Universe.

For matter only interacts gravitational $p = 0$, whereas a relativistic gas (for example a photon gas) has $p \propto \rho/3$. In the case of cosmological constant, $p = -\rho$ – if a vacuum has non-zero energy density, it must also have a non-zero pressure. The proof for this comes from conservation of energy: while the Universe expands, there must be just enough work done to keep the energy density constant. Using the equation of state parameter $w$, we can define the relationship between the pressure and density of each component of the Universe, as

$$p = w\rho c^2 \,. \tag{1.10}$$

For constant values of $w$, the fluid equation can be integrated to get the evolution of the fluid density which is dependent on time. The equation of state for each fluid component, as described above, is unique with

$$\begin{aligned} &w_m \approx 0 \quad (\text{matter})\,, \\ &w_r = 1/3 \quad (\text{radiation})\,, \\ &w_\Lambda = -1 \quad (\text{cosmological constant})\,. \end{aligned} \tag{1.11}$$

The matter density term is predominantly dark matter (which we expect to only interact gravitationally, see section 1.1.5 for more detail), but also includes baryons and neutrinos which do not have zero pressure. Therefore the equation of state parameter for matter is only approximately zero. We find that the density depends on the scale factor as

$$\begin{aligned} &\rho_m \propto a^{-3}\,, \\ &\rho_\gamma \propto a^{-4}\,, \\ &\rho_\Lambda = \text{constant}\,. \end{aligned} \tag{1.12}$$

From the relationships given above we can see which components dominate at different times. In the early Universe after a period of inflation, the Universe was radiation dominated until the epoch of matter-radiation equality. This is the period when the energy density in matter equals the energy density in radiation, after which matter became the dominant component. We expect photons to decouple when the Universe was already well into the matter dominated era, since the formation of neutral hydrogen is only energetically favoured once the Universe had sufficiently expanded and cooled. At current times the Universe is thought to be dominated by dark energy. It is still being explored in alternative models whether dark energy acts as a cosmological constant or has some dependence on time. The dependence of each component on the scale factor, given above, will affect the production of LSS and the development of CMB anisotropies, since perturbations grow at different rates during different eras.

In an expanding Universe, galaxies are moving away from each other, so we should find that galaxies are seen to be moving away from us and their emitted light should be observed at a longer wavelength. Using the FLRW metric we can derive the cosmological redshift due to the expansion of the Universe. Since light travels along null geodesics and considering a radial emission, the metric becomes

$$dr = -c\frac{dt}{a(t)}\,. \tag{1.13}$$

Considering light emitted from a galaxy at a time $t_e$ which is then observed at $t_o$, the comoving distance is

$$r = \int_{t_e}^{t_o} \frac{cdt}{a(t)}\,. \tag{1.14}$$

A similar equation can be written for light emitted at a later time $t_e + \Delta t_e$ and observed at $t_o + \Delta t_o$. Since $r$ is comoving and therefore does not change as the Universe expands we can equate the two cases. For a small $t_o$ and a small expansion rate compared to the speed of light it follows that

$$\frac{\lambda(t_e)}{a(t_e)} = \frac{\lambda(t_o)}{a(t_o)}, \tag{1.15}$$

where we have used $\lambda = c\Delta t$, for the wavelength of light emitted or observed from the galaxy and $\Delta t$ is the time lapsed between two crests of the light waves being. The redshift is defined as

$$z = \frac{\lambda(t_o) - \lambda(t_e)}{\lambda(t_e)} \tag{1.16}$$

and since $a(t_o) = 1$ for the present, we find

$$a = \frac{1}{1+z}. \tag{1.17}$$

Spectral features produced by distant galaxies are observed to be shifted towards the red part of the spectrum as a product of the Universe expanding. Thus a shift in spectral lines tells us the redshift of a galaxy, which is a measure of the scale factor at the time of emission.

The FLRW metric implies that physical distance are related to comoving distances with the time dependent scale factor. The comoving distance between Earth and a source at redshift $z$ is

$$\chi(z) = \int_0^z \frac{dz'}{H(z')}. \tag{1.18}$$

We also define conformal time

$$\eta = \int_0^t \frac{dt'}{a(t')} = \int_z^\infty \frac{dz'}{H(z')}, \tag{1.19}$$

which is a coordinate-independent measure of time.

### 1.1.2 Structure Formation

In this section we describe the process that produces the structure we observe in the Universe, which in general terms refers to any departures from homogeneity. This process of structure formation depends on the background cosmology and thus by examining structure we can constrain cosmological models.

The inhomogeneities that seeded the structure we see today are believed to have arisen from quantum fluctuations during an era of inflation. This idea predicts that structure evolved from adiabatic Gaussian fluctuations. The perturbations have randomly distributed locations and therefore it is most useful to understand the stochastic properties of the distribution. To quantify the patterns we see in the LSS we use the dimensionless density perturbation field

$$\delta(\boldsymbol{x}) = \frac{\rho(\boldsymbol{x}) - \bar{\rho}}{\bar{\rho}} \,. \tag{1.20}$$

Newtonian physics is sufficient for describing the evolution of non-relativistic perturbations in the matter dominated era, which are at scales that have already entered the horizon (Lyth & Liddle, 2009). For an ideal fluid of zero pressure, perturbation $\delta$ is related to the gravitational potential, $\Phi$ via the Poisson equation,

$$\nabla^2\Phi = 4\pi G a^2 \bar{\rho}\delta \,. \tag{1.21}$$

From relativistic perturbation theory and assuming $\delta \ll 1$, the density fluctuations grow as

$$\delta(t) \propto a^2(t) \,, \tag{1.22}$$

during the radiation dominated era, and after matter-radiation equality as

$$\delta(t) \propto a(t) \,. \tag{1.23}$$

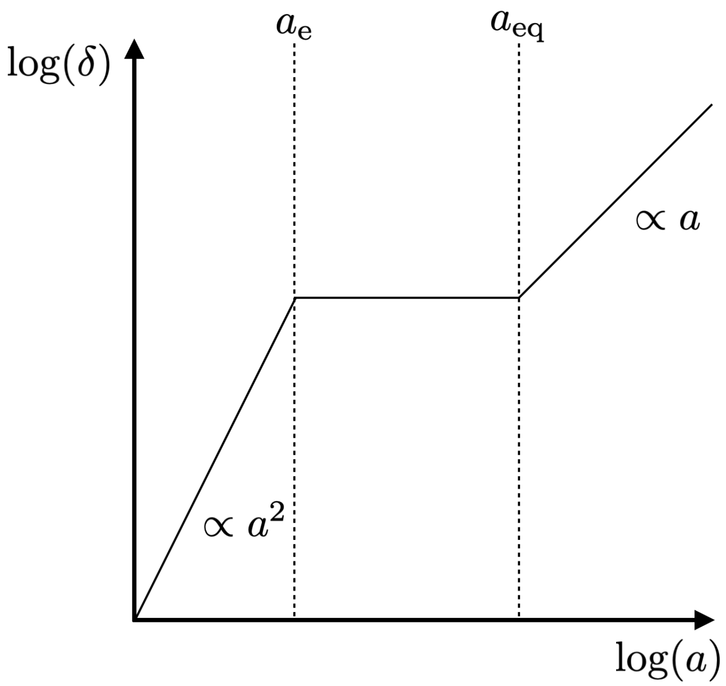


Figure 1.1: A schematic showing the suppression of fluctuation growth that occurs when a density perturbation enters the horizon during the radiation dominated era, prior to matter-radiation equality.

These relations are valid for a flat Universe and at early times when $\Omega_\Lambda = 0$. The results given above for the matter and radiation dominated eras can be combined to state that while $\Omega = 1$ the gravitational potential perturbations are independent of time. From the Poisson equation $-k^2\Phi/a^2 \propto \bar{\rho}\delta$, recall that during radiation and matter domination $\rho \propto a^{-4}$ and $\rho \propto a^{-3}$ respectively, so that in both cases $\rho\delta \propto a^{-2}$ implying

$$\Phi = constant\,. \tag{1.24}$$

That is, the metric fluctuations arising from potential perturbations are fixed for perturbations that have wavelengths larger than that of the horizon size, $d_H$ defined as the region over which radiation can travel.

At late times, density perturbations grow by means of the growth function $g(a)$, as

$$\delta(a) = \delta_0 a \frac{g(a)}{g(a_0)}\,, \tag{1.25}$$

which is found by computing the linear growth factor of matter perturbations, $D(a)$, by solving the differential equation,

$$\frac{d}{da}\left(a^3 H(a)\frac{dD}{da}\right) = \frac{3}{2}\Omega_m(a) a H(a) D\,, \tag{1.26}$$

numerically (e.g., Chisari et al., 2019). The growth function is then defined as $g(a) \equiv D(a)/a$.

Figure 1.1 displays a schematic of the growth history for matter density fluctuations. For scales larger than the horizon, $\varphi > d_H$, perturbations in matter and radiation evolved together, such that at early times fluctuations grew at the same rate regardless of wavenumber. This growth terminated once the horizon had grown larger than the wavelength of the perturbation. In the case of baryons, this was due to radiation pressure and for collisionless matter (i.e. dark matter), the fast expansion driven by radiation halted any further collapse until matter-radiation equality. This is referred to as the Mészáros effect (Meszaros, 1974). The result is a complete suppression of the amplitude of fluctuations that were inside the horizon prior to matter-radiation equality. Collisionless matter collapsed under gravity once matter dominated, however, ionised baryons remained bound to photons and thus continued to oscillate. These oscillations were set up by opposing forces in the primordial plasma, where an overdense region would gravitationally pull matter towards it, which would then be counteracted by pressure created from photon-matter interactions (Zel'dovich, 1970; Peebles & Yu, 1970; Eisenstein et al., 2005).

At recombination, baryons dropped into the gravitational potential wells formed by cold dark matter. This presents the basic process of galaxy formation in which the baryonic component of a galaxy inhabits a larger dark matter halo. The superstructure that we observe today was created when the larger scale fluctuations became causally connected as the horizon grew. This is referred to as the 'bottom-up' model where structure forms from a hierarchical process of collapsing and merging. It should be noted that if dark matter is relativistic (or 'hot'), diffusion would remove any small scale fluctuations so that only the largest scale fluctuations remain. This would require a 'top-down' model of structure formation which does not agree with observational evidence (Schmitz, 2009).

#### 1.1.2.1 The Matter Power Spectrum

The most important statistic when considering the LSS (and the cosmic microwave background 1.1.3 ) is the 2-point correlation function in configurational space and the power spectrum in Fourier space. Working in Fourier space is more convenient for statistics of translation-invariant fields as it is simpler to separate linear and non-linear scales. Non-linear scales are problematic to model, particularly because of the presence of baryons that affect the evolution of structure. Also, individual band-power measurements are usually much less correlated in comparison to a configuration-space analysis which makes covariance matrix estimation easier. This is discussed further in section 2.1. The power spectrum of the density perturbation field, $P(k)$, is given by

$$\left\langle \tilde{\delta}(\boldsymbol{k})\tilde{\delta}(\boldsymbol{k}')\right\rangle = (2\pi)^3 P(k)\delta_D^3(\boldsymbol{k}-\boldsymbol{k}')\,, \tag{1.27}$$

where the angled brackets average over the whole distribution, $\delta_D$ is a Dirac delta function and $\tilde{\delta}(\boldsymbol{k})$ is the Fourier transform of $\delta(\boldsymbol{x})$ defined by

$$\tilde{\delta}(\boldsymbol{k}) = \int d^3\boldsymbol{x}\delta(\boldsymbol{x})e^{-i\boldsymbol{x}\cdot\boldsymbol{k}}\,. \tag{1.28}$$

The wavenumber $\boldsymbol{k}$ is connected to the fluctuation wavelength $\varphi$ by $k = 2\pi/\varphi$. The power spectrum describes the spread, or variance, in a distribution.

For a density fluctuation with wavelength $\varphi$, it enters the horizon when

$$\varphi = \frac{c}{a_{\mathrm{e}} H(a_{\mathrm{e}})}\,, \tag{1.29}$$

where $a_{\mathrm{e}}$ is the scale factor at that time and $H$ is the Hubble factor. This comes from the definition of the proper size of the particle horizon $\sim ct$, where we have used $H \propto t^{-1}$. This is true for both the radiation and matter dominated eras, in which $a \propto t^{2/3}$ and $a \propto t^{1/2}$ respectively. The extra factor of $a$ is needed to convert from proper to comoving units. The Hubble factor can also be written as

$$H^2(t) = H_0^2 \Big[a^{-4}(t)\Omega_{r,0} + a^{-3}(t)\Omega_{m,0} - a^{-2}(t)\frac{kc^2}{H_0^2} + \Omega_\Lambda\Big] \tag{1.30}$$

where the zero subscript denotes the current values of cosmological parameters. Considering the radiation dominated era, $H(a) \propto a^{-2}$ so that from equation 1.29

$$\varphi \propto a_{\mathrm{e}}(t_{\mathrm{e}} \ll t_{\mathrm{eq}})\,, \tag{1.31}$$

where $t_e$ corresponds to the time of entering the horizon such that $a_e \equiv a(t_e)$. During matter dominated times $H(a) \propto a^{-3/2}$ which gives

$$\varphi \propto a_{\mathrm{e}}^{1/2}(t_{\mathrm{eq}} \ll t_{\mathrm{e}} \ll t_0)\,. \tag{1.32}$$

These relationships can be used to inform us about the shape and evolution of the power spectrum. Using the dependence of the density perturbations on the scale factor, shown in equations 1.22 and 1.23, with the definition of the power spectrum from equation 1.27, the initial power spectrum $P_i$ has changed by the time of entering

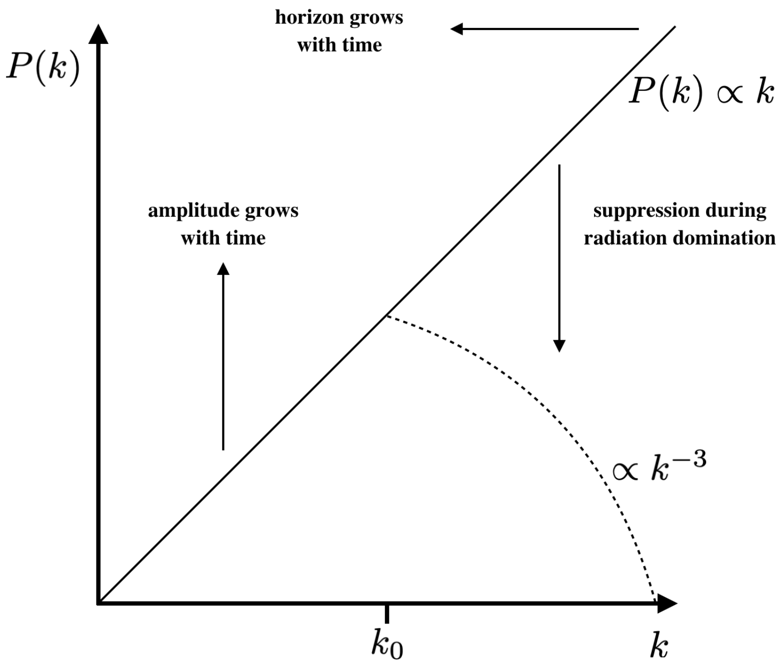


Figure 1.2: The above figure illustrates how the Mészáros effect alters the initial power spectrum. The solid line corresponds to the Harrison-Zel'dovich spectrum.

the horizon as

$$
\begin{aligned}
P_{\mathrm{e}}(k) &\propto a_{\mathrm{e}}^4 P_i(k) \propto \frac{1}{k^4} P_i(k)\,(t_{\mathrm{e}} \ll t_{\mathrm{eq}})\,, \\
P_{\mathrm{e}}(k) &\propto a_{\mathrm{e}}^2 P_i(k) \propto \frac{1}{k^4} P_i(k)\,(t_{\mathrm{eq}} \ll t_{\mathrm{e}} \ll t_0)\,.
\end{aligned} \tag{1.33}
$$

At the time of entering the horizon, the total power of the density fluctuations is assumed to be scale invariant, $k^3 P_{\mathrm{e}} = \text{constant}$. Substituting in that $P_e(k) \propto k^{-4} P_i(k)$, the power spectrum must therefore scale as $P_i(k) \propto k^{n_s}$, for a spectral index of $n_s = 1$. This is shown as the solid line in Fig. 1.2, referred to as the Harrison-Zel'dovich spectrum (Harrison, 1970; Zel'dovich, 1972).

For a fluctuation which entered the horizon prior to matter-radiation equality, the growth is suppressed by

$$
f = \left(\frac{a_{\mathrm{e}}}{a_{\mathrm{eq}}}\right)^2 . \tag{1.34}
$$

Using equation 1.29 and that $H(a) \propto a^{-2}$ during the radiation dominated era, a fluctuation that entered the horizon during this period would be suppressed by a factor $f \propto k^{-2}$. From our earlier discussion of the Mészáros effect, we expect that the smallest scales (large $k$) are the first to impacted and their amplitude suffers the strongest suppression. Conversely the largest physical scales (small $k$) that enter the horizon post matter-radiation equality evolve unimpaired. Hence there is a turnover in the power spectrum at a characteristic scale, $k_0$, which is determined by the size of horizon at matter-radiation equality. The is illustrated in Fig. 1.2. The small $k$ scales will be unimpeded and continue to evolve as

$$P(k) \propto k \, (k \ll k_0) \, . \tag{1.35}$$

The power spectrum at large $k$ scales are suppressed by a factor of $f^2$ such that

$$P(k) \propto k^{-3} \, (k \gg k_0) \, . \tag{1.36}$$

This is shown as the dashed curve in Fig. 1.2.

The scale dependence of the density perturbation power spectrum can be encapsulated in the linear transfer function $T_k$. The transfer function describes the evolution of perturbations through the epochs of horizon crossing and the radiation-matter transition. In principle there is a different transfer function for each component of the Universe, however at late time the transfer function for the different types of matter converges to the same value, which does not vary with time at low redshift. The late-time transfer function is important for making predictions about the observed density field.

Some key aspects of the transfer function are shown in Fig. 1.3. In all adiabatic cases, the transfer function tends towards unity for large scales, this corresponds to a universal growth rate meaning that the amplitude of potential perturbations is constant. The main down-turn in the Transfer function is due to the Mészáros

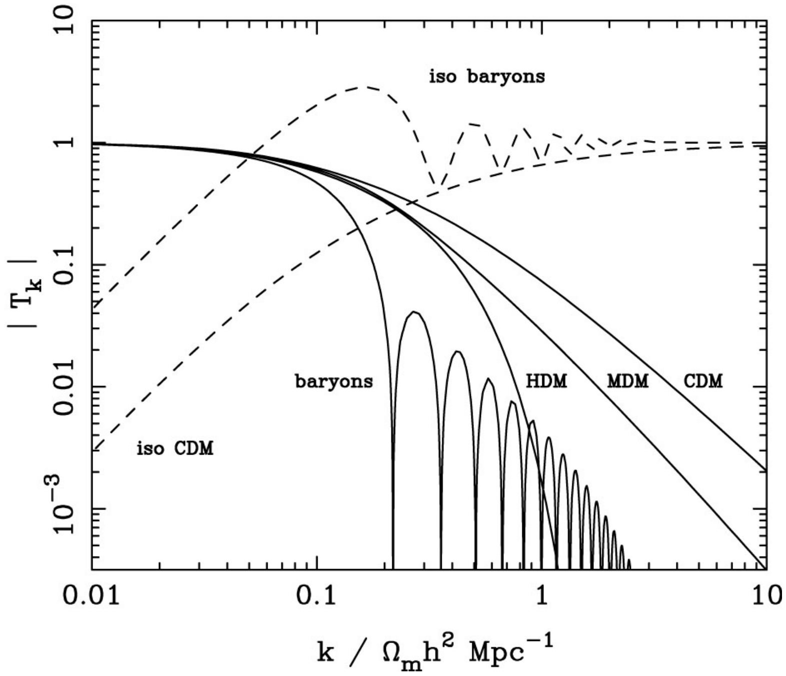


Figure 1.3: The transfer function for a variety of adiabatic models, where $T_k \mapsto 1$ at small $k$. Possible matter contents are displayed for pure baryons, pure cold dark matter and pure hot dark matter. (Peacock, 1999)

effect occurring because the Universe is dominated by radiation at early times. The different gradients for hot, warm and cold dark matter are due to different free-streaming lengths. Random particle velocities can erase perturbations, so for hot dark matter – which is relativistic – more small scale modes are removed.

The horizon size at matter-radiation equality also impacts the baryon component of the transfer function. The largest scales will experience a single acoustic oscillation of order the size of the horizon at equality because the sound speed is around the size of $c$. For a baryon only Universe, there would be large fluctuations in the transfer function. These fluctuations correspond to the number of oscillations completed prior to matter domination, when the pressure due to radiation declines. These features have not been seen in data, which is a reason for concluding that a considerable portion of the Universe's matter budget is collisionless dark matter. Some level of oscillations still occur even for the case of baryons being only a sub-component.

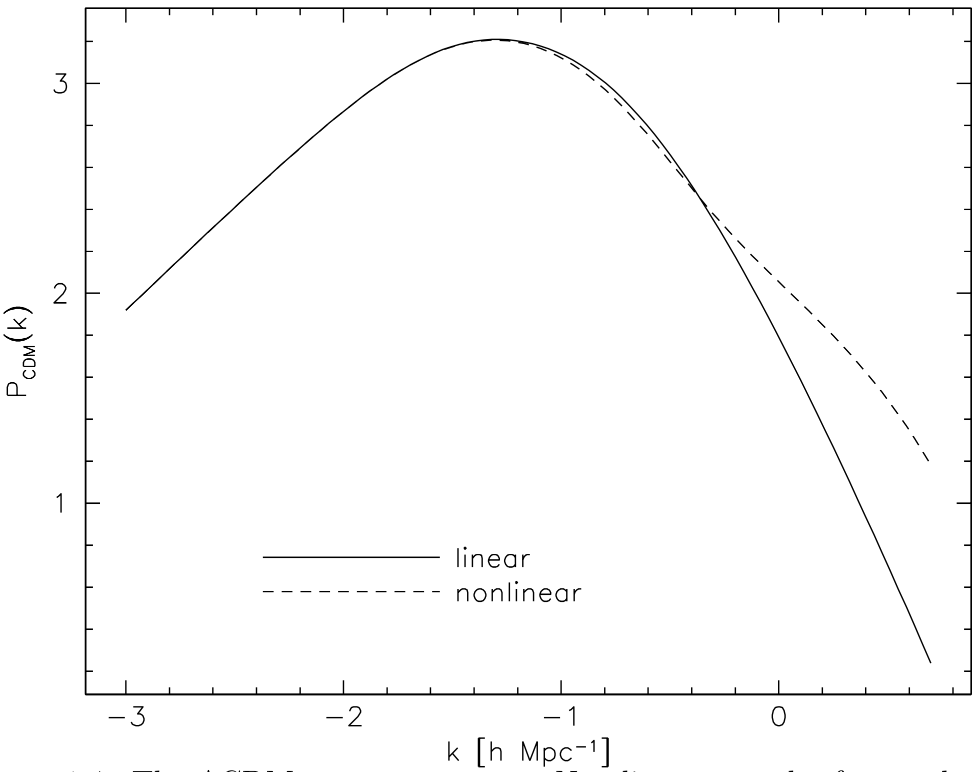


Figure 1.4: The ΛCDM power spectrum. Non-linear growth of perturbations adds power at small scales (large $k$). (Peacock, 1999)

Dark matter has a smoothly decreasing transfer function at matter-radiation equality, however baryons have an oscillating transfer function. The result is that the spatial distribution of each component is different at this time. After the sound speed reduces, gravity pulls both of them together and their transfer functions are the same. Considering baryons are expected to be 5% of the total content, the transfer function has oscillations of order a few percent imposed onto it.

At large enough scales, the matter power spectrum is found by solving the equation of linear perturbation theory. However, at small scales, perturbation theory no longer holds and thus the linear power spectrum must be modified. Essentially this correction is required because the collapse of structure eventually stabilises, which in effect increases the amplitude of the linear power spectrum at small scales (large $k$). We refer to this as the 'non-linear' matter power spectrum, shown in Fig. 1.4 in comparison to the linear power spectrum. The non-linear evolution of the density fluctuations is essential for modelling weak gravitational lensing by the LSS

There are a variety of approaches that can be implemented to predict the matter power spectrum, including approximate analytical expressions for the transfer function (Bardeen et al., 1986; Eisenstein & Hu, 1998), which dictates the form of the power spectrum. Alternatively and more accurately, fitting functions from numerical simulations (Smith et al., 2003; Takahashi et al., 2012) are more often used to describe the non-linear matter power spectrum.

### 1.1.3 The Cosmic Microwave Background

Prior to recombination, when the Universe was still in a radiation dominated phase, oscillations that were smaller than the Jeans' length ($M_J \equiv ct/\sqrt{3}$), were in a bound plasma of photons and baryons where the attraction due to gravity is then counterbalanced by radiation pressure. These oscillations cease at recombination and produce temperature fluctuations which we see as the Cosmic Microwave Background (CMB).

The CMB presents a snapshot of the Universe when it was only about 300,000 years old. At a redshift of 1100, the photons of the CMB stopped scattering off electrons and could then travel freely through space. The collisions with electrons guarantee that the photons were in equilibrium and will thus have a blackbody spectrum.

Early observations of the CMB presented a very smooth early Universe, corroborating the idea of a smooth big bang (Mather et al., 1990). Subsequent observations revealed anisotropies which were the small perturbations in the cosmic plasma (Smoot et al., 1992). Measuring the locations of peaks in the CMB power spectrum informs us about the characteristic angular scale of the fluctuations which directly relates to the geometry of the Universe. Taking the ratio of the amplitude of peaks at different oscillation modes contains information about the baryon fraction (Planck Collaboration, 2018).

Fluctuations in the 2D temperature field can be treated in an analogous way to the fluctuations in the density field. The fluctuations can be imagined as existing on the inside of a sphere and so the observed temperature $T$ varies with angle. Since the temperature perturbation field is created from the density perturbations, it retains the property of being a Gaussian random field. Thus, the temperature is expanded in spherical harmonics as

$$\frac{\delta T}{T}(\hat{\boldsymbol{q}}) = \sum a_\ell^m Y_{\ell m}(\hat{\boldsymbol{q}})\,, \tag{1.37}$$

where $(\hat{\boldsymbol{q}})$ is the unit vector which determines the direction on the sky. From the orthonormality relation $\int Y_{\ell m} Y^*_{\ell' m'} d^2 q = \delta_{\ell\ell'}\delta_{mm'}$, the variance in the temperature, averaging across the sky is

$$\left\langle \left(\frac{\delta T}{T}\right)^2 \right\rangle = \frac{1}{4\pi}\sum_{\ell,m}\langle |a_\ell^m|^2\rangle \equiv \frac{1}{4\pi}\sum_\ell (2\ell+1)C_\ell\,. \tag{1.38}$$

In practice the observed sky is only one realisation of the random field, and each $a_\ell^m$ is drawn from its associated Gaussian. The power spectrum can still be accurately measured at small scales (large $\ell$), but at small $\ell$ (large scales) there is a considerable and inescapable modelling uncertainty that arises from only being able to observe one CMB. This is also true for density perturbations and is referred to as cosmic variance.

In addition to measuring the temperature field, the polarisation of photons also contains cosmological information. The three so-called Stokes' parameters are usually used to describe the polarisation, but assuming circular polarisation is not present, only $Q$ and $U$ parameters remain. Polarisation has direction on the sky, such that a more complicated set of basis function, referred to as spin-weighted spherical harmonics, are required to expand $Q$ and $U$. The polarisation field is more often described in the $E$ and $B$ basis, where $E$ corresponds to the curl-free part of the field and $B$ to the gradient-free part. Therefore, overall there are four power spectra that can be measured, the auto spectra $C_\ell^{TT}, C_\ell^{EE}, C_\ell^{BB}$ and cross-correlation between the temperature and $E$ polarisation $C_\ell^{TE}$. The $B$ polarisation is uncorrelated with the other fields since it has opposite parity.

There are three processes which create the primary CMB anisotropies. This includes gravitational (Sachs-Wolfe) perturbations, when a photon from a overdense region must escape a potential well and is therefore redshifted. The second being intrinsic (adiabatic) perturbations produced from high-density regions, where the coupling between matter and radiation compresses the radiation and produces a higher temperature. Finally the velocity (Doppler) perturbations which cause a Doppler shift in frequency because the plasma has a velocity greater than zero at the time of recombination. There may also be a fourth mechanism which is from a background of primordial gravitational waves produced during inflation (Polnarev, 1985) – these are yet to be observed.

In addition to the primary mechanisms listed above, there are also secondary effects which are interactions that occur along the line of site, i.e. redshifts less than 1100. The integrated Sachs-Wolfe effect results from potential perturbations evolving (Sachs & Wolfe, 1967; Rees & Sciama, 1968). This is only important just after recombination when radiation is still influential and at late times when $\Lambda$ is dominant, since the potential stays constant in the linear regime during matter domination (Dodelson, 2003). On small scales, non-linear structure leaves imprints on the CMB through the Sunyaev-Zel'dovich effect (Sunyaev & Zeldovich, 1970; Rephaeli, 1995) – where the CMB photons are scattered off hot gas – and also couples modes together through gravitational lensing (Stompor & Efstathiou, 1999) (explained in full in section 1.2).

### 1.1.4 Galaxy Clusters

Density perturbations have larger amplitudes at smaller scales. Any region which is denser than the average density will be gravitationally bound, decouple from the expansion of the Universe and virialise. This process produces sub-galaxy size objects which then group together to make galaxies which further group together to create clusters. Galaxy clusters pinpoint the positions of peaks in the large-scale cosmic web. They consist of hundreds to thousands of galaxies, a diffuse ionised intra-cluster medium (ICM) and dark matter – which correspond to 3%, 13% and 85% of the total mass respectively (Allen et al., 2011). The dynamical time-scales of clusters are almost as long as the age of the universe, so they therefore contain information about their formation. Also, high redshift observations can be made because clusters are so bright at optical wavelengths and the detection method applied in the millimetre regime has a weak dependence on redshift, and thus we can view them at an earlier stage in their evolution. Thus, the growth and development of clusters can be used to trace structure formation in the Universe.

For a given cluster sample, the expected number of clusters in a mass bin $a$, redshift bin $z_i$ and solid angle $\Delta\Omega$ is given by

$$\bar{N}(M_a, z_i) = \frac{\Delta\Omega}{4\pi} \int_{z_i}^{z_i+1} dz \frac{dV}{dz} \int_{\ln M_a}^{\ln M_{a+1}} d\ln M \frac{dn(M,z)}{d\ln M}\,, \tag{1.39}$$

where cosmology enters via the halo mass function and the comoving volume element $dV/dz$ which depends on $\Omega_m$, $h$ and $w(z)$ (Allen et al., 2011). The halo mass function is sensitive to the growth of perturbations in the matter density field through $\sigma_8$ and the growth function $g(z)$. The amplitude of mass fluctuations is described by the parameter $\sigma_8$, which is defined as the standard deviation of the (linear) density field smoothed on a comoving scale of 8Mpc/$h$,

$$\sigma_8^2(z) \equiv \sigma^2(R = 8\text{Mpc}/h, z) = \int_0^\infty \frac{dk}{k} \Delta^2(k,z) \mathcal{W}^2(k, R = 8\text{Mpc}/h)\,, \tag{1.40}$$

where $\mathcal{W}$ is the Fourier transform of a top-hat function with a width of 8Mpc/$h$ and $\Delta(k)$ is the dimensionless matter power spectrum. This was originally parameterised this way as a convenient way to normalise the matter power spectrum.

### 1.1.5 Cosmic Inventory

The Universe is made up of numerous constituents. In the early Universe, radiation was the dominant component until matter-radiation equality at $z \sim 3200$. In the common picture the Universe remained matter dominated until $z \sim 0.7$ – after this vacuum energy takes over as the dominant part (Peacock, 1999).

The matter component can be split further into baryons and dark matter. *Baryons* constitute all the visible parts of the Universe and yet they only make up 5% of the total energy budget. We expect baryons to trace the underlying dark matter distribution. They have little impact on the matter power spectrum, although they do produce two signature effects in that the power spectrum is suppressed at small scales and they will introduce small oscillations in the transfer function at around $k \sim 0.1h\mathrm{Mpc}^{-1}$ (Dodelson, 2003).

In 1933, Zwicky studied the Coma cluster and found that the cluster would break up if only luminous matter was present (Zwicky, 1933). Many studies of galaxies followed, finding that the rotation velocity of stars in a given galaxy was constant at all radii, even though the density of light emitting matter decreased as a function of radius (Rubin et al., 1980). By the 1980's there was a wealth of evidence concluding that some extra non-luminous matter – later coined '*dark matter*' – in an outer halo was required to explain the rotation curves of galaxies. These dark halos had to be 5-10 times the mass of the luminous component of the galaxy.

Since dark matter is expected to only interact gravitationally, this does leave open the possibility for a modification to gravity rather than a new particle being required to explain the missing mass problem described above. Dark matter is expected to have nearly zero pressure and temperature and hence is usually referred to as 'cold'. If dark matter is 'hot' then the thermal velocities would be high enough to smear out galaxy clusters and so hot dark matter has been ruled out. 'Warm' dark matter on the other hand would only remove dwarf galaxies and larger halos, like our own

Milky Way, would be unaffected (Blumenthal et al., 1984).

Potential baryonic candidates have been suggested in the form of brown and white dwarf stars. However, if this was the case they would have been seen in micro-lensing events within our own galaxy and the nearby Andromeda galaxy M31 (for example Bahcall et al., 1994; Graff & Freese, 1996; Alcock et al., 1997). The currently favoured view is that they are a fundamental particle which hold no charge since they are expected to pass through matter without experiencing any interaction. Weakly Interacting Massive Particles (WIMPs) are well motivated and commonly occur in many extensions to the standard model of particle physics. They have therefore been the most promising candidate. However, terrestrial searches for their signatures have yet produce any detection. An alternative candidate is an axion-like particle which also appears in extensions to the standard model and its presence has been shown to solve various problems in particle physics. Other dark matter model options include warm dark matter, self-interacting dark matter, baryon-scattering dark matter, fuzzy dark matter, primordial black holes and light relics. These models can be distinguished by their impact of structure formation. For further details on potential dark matter candidates see the review Bertone et al. (2005).

As well as cold dark matter we also include *neutrinos* in our cosmic inventory. In the standard picture, there are three species of neutrinos which are weakly interacting. From the standard model of particle physics, neutrinos are predicted to be massless. However from observations of flavor oscillations in solar and atmospheric neutrinos, they must contain mass. Neutrinos impact cosmology by contributing to the expansion history of the Universe through their energy density and by altering the evolution of matter perturbations (Lesgourgues & Pastor, 2006).

The final component of our Universe, *dark energy*, dominates our Universe at late times. Evidence for the accelerated expansion of the Universe was first seen in observations of type Ia supernovae that were found to be fainter than anticipated (Schmidt et al., 1998; Perlmutter et al., 1999). This has since been cemented independently through measurements of the CMB (Spergel et al., 2003), inhomogeneities in the matter distribution (Cole et al., 2005), the integrated Sachs-Wolfe effect (Boughn & Crittenden, 2004), baryon acoustic oscillations (Eisenstein et al., 2005), weak lensing (Contaldi et al., 2003) and gamma-ray bursts (Kodama et al., 2008). Within the structure of General Relativity this accelerated expansion must be driven by a new form of energy density component with a negative pressure. From measurements of the CMB and theoretical predictions we anticipate the density of the Universe to be very close to the critical density. However we actually observe it to be about $1/3\rho_c$, so the remaining 2/3 must be in some smooth non-clustered form. This elusive component of the Universe has been coined dark energy. Dark energy produces a turnover in the matter power spectrum on scales much larger than that predicted by CDM alone. The amplitude of the power spectrum increases as the dark energy content goes up. The growth factor also depends on the dark energy model (Dodelson, 2003).

Observational evidence to date has been inline with a cosmological constant $\Lambda$ (for example Planck Collaboration, 2018). However, from a theoretical perspective the value of $\Lambda$ is orders of magnitudes less than the values predicted from Particle Physics (Weinberg, 1989). Other models include an evolving dark energy or a deviation from General Relativity (for example Caldwell et al., 1998; Liddle & Scherrer, 1999; Peebles & Ratra, 2003).

## 1.2 Gravitational Lensing

### 1.2.1 Overview

In 1937 when Zwicky noted that observations of the Coma cluster indicated the existence of dark matter, he also went on to predict that the mass of the cluster could be measured via the lensing effect the cluster has on background galaxies (Zwicky,

Figure 1.5: Here are two examples where gravitational lensing is visible. Left: a combined optical and X-ray (shown in pink) image of quasar RX J1131-1231. Due to the presence of a foreground elliptical galaxy, four images of the quasar are seen in the X-ray data from the Chandra satellite, with an Eisten ring clearly visible in the optical data from the Hubble Space Telescope. Right: Hubble Space Telescope image of galaxy cluster RX J1347.5-1145. The massive cluster acts as a lens, resulting in background galaxies appearing as giant arcs around the cluster. *Image credit: NASA*

1937). Gravitational lensing arises from variations in the distribution of matter, which disturbs the path followed by light from distant sources. Large scale density fluctuations create a tidal gravitational field that results in photons being deflected differentially. As a consequence, the images of distant galaxies we observe appear distorted. This effect is the same as looking at these galaxies through a magnifying glass where the refractive index varies across space, such that images are distorted and magnified. The amount of distortion is determined by the size and shape of the matter distribution along the line-of-sight – such that the more massive the lens the stronger the lensing distortion. From our concordance model of cosmology, the majority of mass along the line-of-sight is dark matter. Therefore gravitational lensing is a way in which dark matter in the Universe can effectively be mapped. Investigating the lensing effect at different epochs therefore contains information about the effect of dark energy on the evolution of structure.

Gravitational lensing can create visibly striking phenomena in the form of giant arcs around massive galaxy clusters, and multiple images of distant quasars due to lensing by elliptical galaxies. These very noticeable deflection effects, shown in Fig. 1.5 are referred to as 'strong' lensing and only occur for the most massive lenses. However, all structure in the Universe will cause the properties of distant sources to be only slightly modified by the deflection – we refer to this as the 'weak' lensing regime (for a recent review, see Kilbinger, 2015). Although this effect is not visible by eye, we can detect it statistically. The distant light sources we refer to could be a variety of objects, however in this thesis we are concerned with the weak gravitational lensing of light from galaxies and the CMB due to the LSS, described in section 1.1.2.

In the case of the CMB, the most distant source, lensing modifies the statistical properties of CMB anisotropies, by introducing correlations between CMB modes that would otherwise be independent. Therefore both distant galaxies and the CMB provide a tool for inferring properties of the LSS.

We start with a brief qualitative discussion of the two types of galaxy weak lensing utilised in this thesis. This is then following by a mathematical description of gravitational lensing, deriving the deflection angle and observables. Although this prescription is specific to galaxy lensing it is largely transferable to the case of CMB lensing. Finally, we include an introduction to CMB lensing, outlining methods used to recover the lensing information from CMB data. In this section we follow the more detailed derivations of Bartelmann & Schneider (2001) and Lewis & Challinor (2006).

### 1.2.2 Cosmic Shear

As light from distant galaxies travels through the LSS, it experiences tiny deflections. When projected onto a 2D plane, these galaxy distortions will be coherent, towards a given direction that depends on the intervening matter along the line-of-sight. Since this is an incredibly weak effect, we require measurements of many galaxies over large areas of sky, to make a statistically significant measurement. This is achieved by measuring the correlation between galaxy shapes – referred to as 'cosmic shear'.

Cosmic shear measures the clustering of the LSS from the highly non-linear, non-Gaussian sub-Mpc regime, out to very large, linear scales of more than 100Mpc. By measuring the correlation of galaxy shapes at and between different redshifts, the evolution of the LSS can be traced, enabling us to detect the effect of dark energy on the growth of structure. Since gravitational lensing is not sensitive to the dynamical state of the intervening masses, it yields a direct measure of the total mass.

Cosmic shear is now a well established cosmological tool, providing constraints on the matter density parameter $\Omega_m$ and the amplitude of matter fluctuations $\sigma_8$ (e.g Hildebrandt et al., 2018; Hikage et al., 2019; Troxel et al., 2018; Heymans et al., 2013). The methodology has evolved significantly over time since the first detection (Bacon et al., 2000; Van Waerbeke et al., 2000; Wittman et al., 2000). To be able to produce these constraints on cosmology requires measuring the shapes of galaxies to infer the distortion (or 'shear') due to lensing, estimating the distance to galaxies and using a series of other data and simulations to calibrate the shape and redshift values. A rigorous procedure is required to mitigate systematic effects which can bias results. For example, the telescope itself produces complicated patterns which can imitate the lensing signal. This is referred to as the Point Spread Function (PSF) which for ground based observations also includes the effect of the atmosphere, which blurs the images of galaxies. The PSF is corrected for by making observations of stars and using this information to model the distortion induced during the observation process (Kaiser et al., 1995; Hirata & Seljak, 2003).

Additional difficulties which are consequential for cosmic shear include the intrinsic alignment between galaxies due to the tidal fields they inhabit (Hirata & Seljak, 2004; Chisari et al., 2015). This effect breaks our assumption that in the absence of lensing all galaxies are randomly orientated, and therefore needs to be included in the modelling procedure. Recently, the impact of photometric redshift estimation has been shown to be substantial for current cosmic shear analyses (Joudaki et al., 2019). This is partially due to the fact that as surveys become larger and deeper, the community has fewer suitable spectroscopic galaxy catalogues available to use for calibration (Bolzonella et al., 2000; Benítez, 2000; Ilbert et al., 2006; Brammer et al., 2008; Choi et al., 2016; Wright et al., 2018). A final limiting factor is the software used to estimate the shapes of galaxies. Although this is deemed a minor issue for current surveys, as the number density of sources increases in future, effects such as the blending of galaxy images will require novel techniques (Mandelbaum et al., 2018).

### 1.2.3 Galaxy-galaxy Lensing

Galaxy-galaxy lensing measures the correlation between the position of a foreground lensing galaxy and the shape of a more distant galaxy (for example Leauthaud et al., 2017; Prat et al., 2018; Amon et al., 2018). The methodology is also applicable when considering any other foreground lensing halo, like a galaxy cluster. Considering a single halo, more distant galaxies will appear to be aligned tangentially around the halo, with the strength of alignment decreasing with increasing distance from the lens. The level of tangential alignment is determined by the lensing halo, thus we can use this method to infer properties of the halo and the relationship between galaxies or clusters and the halos they inhabit (Velander et al., 2014). By measuring the average tangential shear in annuli around the lens we can build a density profile which contains information about how the mass is distributed inside the lensing halo. The distortions are weak and therefore we are required to average over many similar lens systems so that the shape noise decreases. Therefore in practice we investigate the population of lensing halos in a statistical manner. An example of this is shown in Fig. 1.6, which shows the average galaxy-galaxy lensing signal measured around BOSS-LOWZ luminous red galaxies (LRGs), using weak lensing data from the Canada

France Hawaii Telescope Lensing Survey (Heymans et al., 2012).

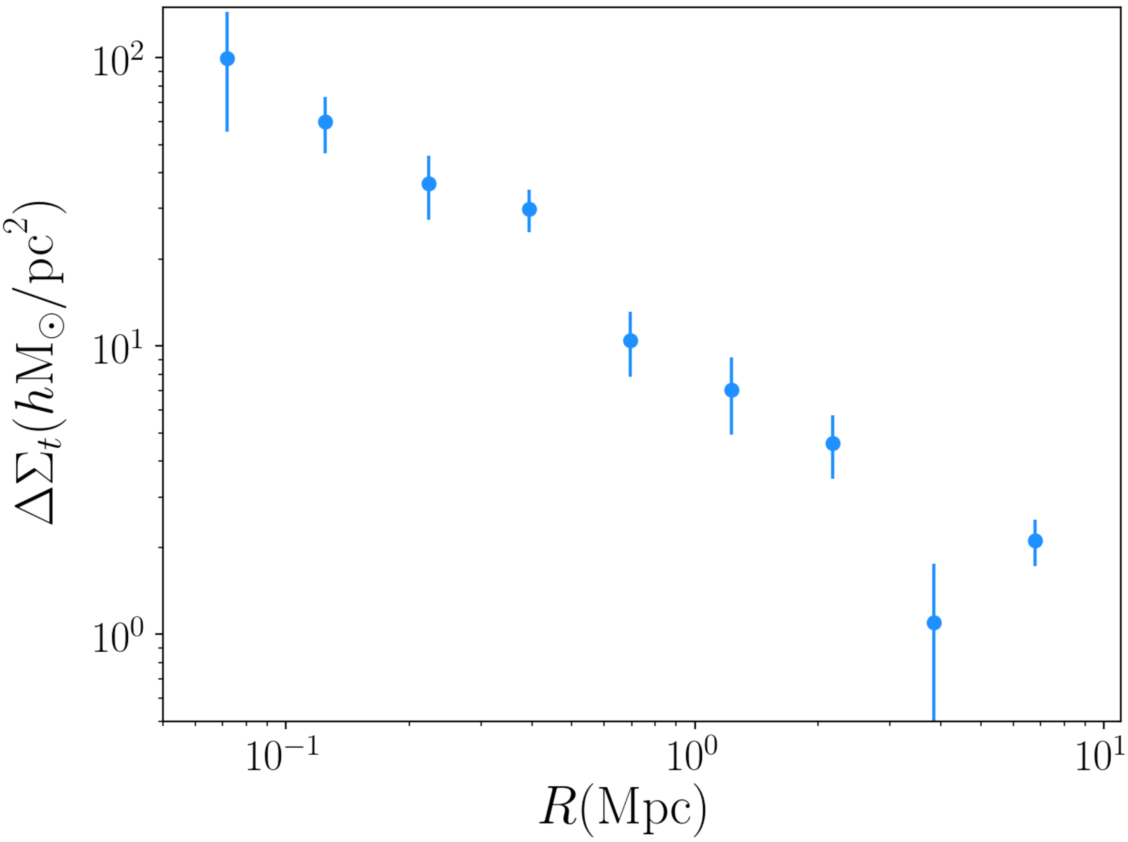


Figure 1.6: Galaxy-galaxy lensing signal measured around BOSS-CMASS luminous red galaxies (LRGs), using weak lensing data from the Canada France Hawaii Telescope Lensing Survey (Heymans et al., 2012). Here we present the lensing signal in terms of the excess surface density $\Delta\Sigma_t$, which is the average tangential shear weighted by the lensing efficiency, as a function of radius $R$. We define and use this quantity in chapter 4.

Since in galaxy-galaxy lensing we take the average tangential shear value in annuli around a lens, this measurement is less affected by systematics such as the PSF which introduce correlations between shapes across an entire observed field. However, this method can be impacted by the poor photometric redshift information for the source galaxies. If the galaxies are estimated to be behind the lens but this is not the case, this will act to dilute the signal (Sheldon et al., 2004; Mandelbaum et al., 2005; Singh et al., 2017). To interpret the galaxy-galaxy lensing signal, we require a theoretical description of the density profile. To date, the main density profile being used in weak lensing is the Navarro-Frenk-White (NFW) profile (Navarro et al., 1997), whose tangential shear profile has been derived analytically in Wright & Brainerd (2000). This profile description is sufficient in the context of isolated lenses. However we know that lensing halos are part of the cosmic web, which will in-turn impact weak lensing observables. An established approach is to implement a halo model (Mo & White, 1996; Cooray & Sheth, 2002; Cacciato et al., 2014), which can account for the impact of satellite halos (Sifón et al., 2018). Alternatively, simulations can also be used to model the lensing signals of halos (Battaglia et al., 2010).

### 1.2.4 The Deflection Angle

A gravitational lensing system can be described by the configuration shown in Fig. 1.7, where $\boldsymbol{\beta}$ is the true position angle of the source, $\boldsymbol{\theta}$ is the angle at which it is observed and $D_d$ and $D_s$ are the distances between the observer and the lens and the observer and the source respectively. The first assumption we make is the thin lens approximation which says that the light ray is instantaneously deflected at the lens plane. This is a reasonable assumption to make and holds provided the spread of the lensing mass along the line-of-sight is much smaller than the angular diameter distances involved. Considering the deflection due to a point mass, provided the light passes sufficiently far away from the strong gravitational field such that the impact parameter $|\boldsymbol{\xi}|$ is much bigger than the Schwarzschild radius of the lens ($|\boldsymbol{\xi}| \gg R_s = 2GM/c^2$), then from General Relativity the deflection angle $\hat{\boldsymbol{\alpha}}$ is related to the impact parameter $\boldsymbol{\xi}$ by

$$|\hat{\boldsymbol{\alpha}}| = \frac{4GM}{c^2|\boldsymbol{\xi}|}\,, \tag{1.41}$$

where $G$ is the gravitational constant and $M$ is the mass causing the deflection. From the condition that $|\boldsymbol{\xi}|| \gg R_s$, we see that the deflection angle must be small, $|\hat{\boldsymbol{\alpha}}| \ll 1$.

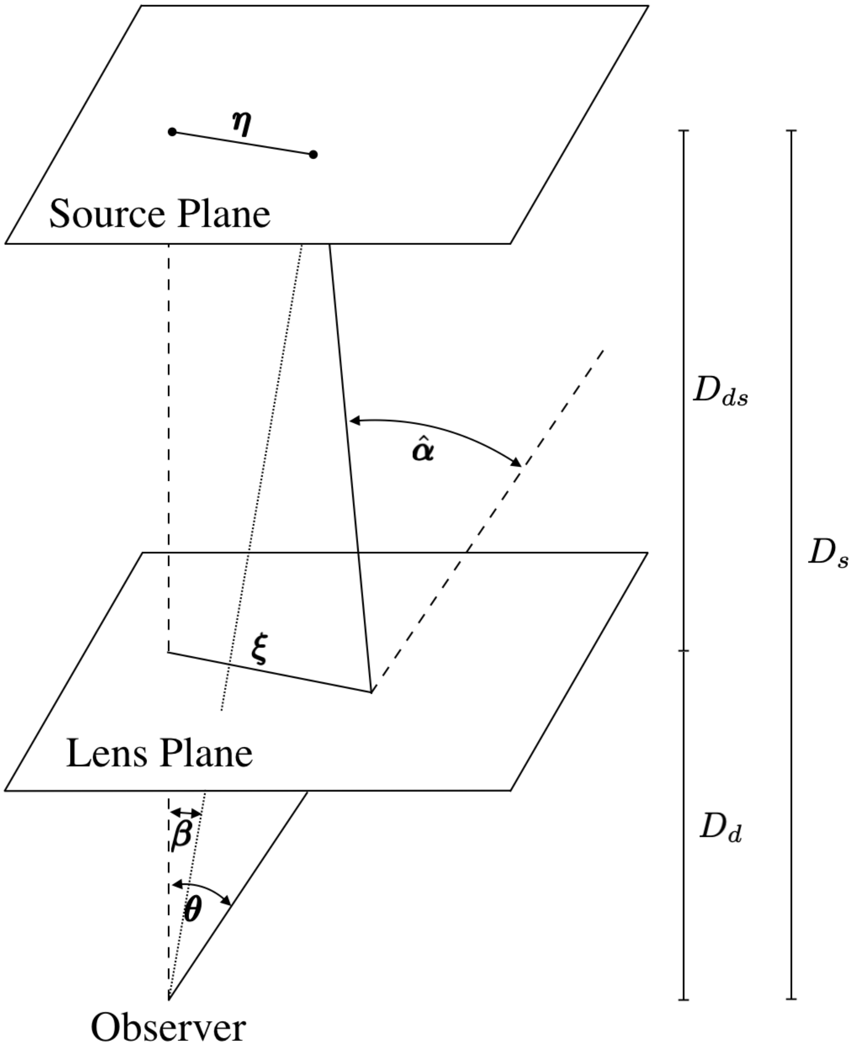


Figure 1.7: A standard lensing configuration between the source, lens and observer. $\boldsymbol{\beta}$ is the true position angle of the source, $\boldsymbol{\theta}$ is the angle at which it is observed and $D_d$ and $D_s$ are the angular diameter distances between the observer and the lens and the observer and the source respectively.

This implies that the strength of the Newtonian gravitational field, $\Phi$, is small,

$$\frac{\Phi}{c^2} \ll 1\,. \tag{1.42}$$

This is the weak field limit. In this limit the General Relativity field equations can be linearised. The deflection angle due to a collection of point masses is then the vectorial sum of the individual deflection angles resulting from each point mass.

A 3D mass distribution with a volume density $\rho(\boldsymbol{r})$ is composed of cells of size $dV$ which contain mass $dm = \rho(\boldsymbol{r})dV$. The spatial trajectory of a light ray passing the mass distribution, is described by $(\xi_1(\lambda), \xi_2(\lambda), r_3(\lambda))$, where the coordinates are chosen such that the light ray travels in the direction $r_3$. The path of the light is bent due to the presence of the mass distribution, but for a small deflection, we can approximate to a straight line in the vicinity of the deflecting mass – this corresponds to a 'thin' lens. Near the lens $\boldsymbol{\xi}(\lambda) \approx \boldsymbol{\xi}$, where $\boldsymbol{\xi} = (\xi_1, \xi_2)$. For a lensing mass element, $dm$, at $\boldsymbol{r}' = (\xi_1', \xi_2', r_3')$, the total deflection angle is then

$$\begin{aligned} \hat{\boldsymbol{\alpha}}(\xi) &= \frac{4G}{c^2} \sum dm(\xi_1', \xi_2', r_3') \frac{\boldsymbol{\xi} - \boldsymbol{\xi}'}{|\boldsymbol{\xi} - \boldsymbol{\xi}'|^2} \\ &= \frac{4G}{c^2} \int d^2\xi' \int dr_3' \rho(\xi_1', \xi_2', r_3') \frac{\boldsymbol{\xi} - \boldsymbol{\xi}'}{|\boldsymbol{\xi} - \boldsymbol{\xi}'|^2} \,, \end{aligned} \tag{1.43}$$

where $\hat{\boldsymbol{\alpha}}$ is a 2D vector. For a two-dimensional mass element $dm = \Sigma(\xi')d^2\xi'$ we can define the surface mass density

$$\Sigma(\boldsymbol{\xi}) \equiv \int dr_3 \rho(\xi_1, \xi_2, r_3) \,, \tag{1.44}$$

which is the mass density projected on to a plane perpendicular to the approaching light ray. This leads to a deflection angle

$$\hat{\boldsymbol{\alpha}} = \frac{4G}{c^2} \int d^2\xi' \Sigma(\boldsymbol{\xi}') \frac{\boldsymbol{\xi} - \boldsymbol{\xi}'}{|\boldsymbol{\xi} - \boldsymbol{\xi}'|^2} \,. \tag{1.45}$$

This equation is legitimate provided that the deflection of a light ray is small relative to the scale on which the mass distribution changes significantly, which is true for gravitational lensing by galaxies and galaxy clusters.

Using the set-up in Fig. 1.7 we can relate the true position of the source to its observed position on the sky. In the small angle approximation, the two-dimensional position of the source on the source plane is given by

$$\boldsymbol{\eta} \approx \frac{D_s}{D_d}\boldsymbol{\xi} - D_{ds}\hat{\boldsymbol{\alpha}}\,. \tag{1.46}$$

Since $\boldsymbol{\eta} = D_s\boldsymbol{\beta}$ and $\boldsymbol{\theta} = \boldsymbol{\xi}/D_d$ we can re-write the above equation as

$$\boldsymbol{\beta} = \boldsymbol{\theta} - \boldsymbol{\alpha}\,, \tag{1.47}$$

which gives us the lens equation, where $\boldsymbol{\alpha} = \frac{D_{ds}}{D_s}\hat{\boldsymbol{\alpha}}$ is the scaled deflection angle. If the lens equation has multiple solutions there are multiple images and the lens can be described as 'strong'.

We can express a quantity called the convergence to quantify this condition, which is defined as

$$\kappa(\boldsymbol{\theta}) = \frac{\Sigma(D_d\boldsymbol{\theta})}{\Sigma_c}\,, \tag{1.48}$$

where $\Sigma_c$ is the critical surface density defined as

$$\Sigma_c = \frac{c^2}{4\pi G}\frac{D_s}{D_d D_{ds}}\,. \tag{1.49}$$

The convergence is measured via the stretching of solid angle on the sky, and since surface brightness is conserved, the result is an amplification of the source flux. If the surface mass density is greater than this critical value, which is equivalent to $\kappa \geq 1$, this corresponds to the strong lens regime. Therefore $\Sigma_c$ essentially distinguishes between 'strong' and 'weak' lensing systems. From our definition of convergence the scaled deflection angle can be written as

$$\boldsymbol{\alpha}(\boldsymbol{\theta}) = \frac{1}{\pi}\int d^2\theta'\kappa(\boldsymbol{\theta}')\frac{\boldsymbol{\theta} - \boldsymbol{\theta}'}{|\boldsymbol{\theta} - \boldsymbol{\theta}'|^2}\,. \tag{1.50}$$

Considering the identity $\nabla_\theta \ln|\boldsymbol{\theta}| = \boldsymbol{\theta}/|\boldsymbol{\theta}|^2$, we can show that the scaled deflection angle is given by

$$\boldsymbol{\alpha}(\boldsymbol{\theta}) = \frac{1}{\pi} \int d^2\theta' \kappa(\boldsymbol{\theta}') \nabla_\theta \ln |\boldsymbol{\theta} - \boldsymbol{\theta}'| \,. \tag{1.51}$$

Defining the lensing potential as

$$\psi(\boldsymbol{\theta}) = \frac{1}{\pi} \int d^2\theta' \kappa(\boldsymbol{\theta}') \ln |\boldsymbol{\theta} - \boldsymbol{\theta}'| \,, \tag{1.52}$$

the scaled deflection angle is then the gradient of the lensing potential

$$\boldsymbol{\alpha}(\boldsymbol{\theta}) = \nabla_\theta \psi(\boldsymbol{\theta}) \tag{1.53}$$

such that the mapping from $\boldsymbol{\theta}$ to $\boldsymbol{\beta}$ is a gradient mapping. Additionally, using the identity $\nabla_\theta^2 \ln |\boldsymbol{\theta}| = 2\pi\delta_D(\boldsymbol{\theta})$, where $\delta_D$ is the two-dimensional Dirac delta function, we have

$$\nabla_\theta^2 \psi = 2\kappa(\boldsymbol{\theta}) \,. \tag{1.54}$$

The deflection angle can also be considered in terms of the gravitational potential itself. Considering the line integral of the gravitational acceleration perpendicular to the direction of light propagation, $a_\perp$,

$$\hat{\boldsymbol{\alpha}} = \frac{2}{c^2} \int a_\perp dz \,, \tag{1.55}$$

where the acceleration is due the gravitational potential of the lens $\Phi$ such that $a_\perp = \nabla_\perp \Phi$ so that

$$\hat{\boldsymbol{\alpha}} = \frac{2}{c^2} \int \nabla_\perp \Phi dz \,. \tag{1.56}$$

Since $\boldsymbol{\xi} = D_d \boldsymbol{\theta}$ and from equation 1.53

$$\boldsymbol{\alpha} = d_d \nabla_\xi \psi \,, \tag{1.57}$$

which leads to

$$\psi = \frac{D_{ds}}{D_d D_s} \frac{2}{c^2} \int \Phi(\xi, z) dz \,, \tag{1.58}$$

where the gravitational potential is related to the density via the Poisson equation $\nabla_\xi^2 \Phi = 4\pi G \rho(\boldsymbol{\xi}, z)$.

### 1.2.5 Magnification, Shear and Image Distortion

The flux of source images is affected by the gravitational deflection because the cross-sectional area of a package of light is distorted by differential deflection. Photon number is conserved, so the flux of an image is established from this cross-sectional distortion. The shapes of the source images are also adapted as a result of this.

Liouville's theorem – which says that the phase space density is unchanged during the photon propagation provided no absorption or emission of photons takes place – implies that surface brightness must be conserved. Therefore, if the surface brightness in the source plane is given by $I_\nu^{(s)}(\boldsymbol{\beta})$ (which is what we would observe in the absence of light deflection), then the surface brightness in the lens plane is

$$I_\nu(\boldsymbol{\theta}) = I_\nu^{(s)}[\boldsymbol{\beta}(\boldsymbol{\theta})] \,, \tag{1.59}$$

for an observed frequency $\nu$. For an infinitesimal source with a surface brightness, $I_\nu$, which is not gravitationally lensed, it subtends a solid angle $d\omega^*$. The monochromatic flux from the source is

$$S_\nu^* = I_\nu d\omega^* \,. \tag{1.60}$$

If the source is gravitationally lensed, the observed flux is then

$$S_\nu = I_\nu d\omega \,, \tag{1.61}$$

and so the deflection modifies the flux of the observed image by a factor

$$|\mu| = \frac{S_\nu}{S_\nu^*} = \frac{d\omega}{d\omega^*}\,, \tag{1.62}$$

which does not depend on the frequency of the deflected light. The ratio of the solid angles is given by

$$\frac{d\omega}{d\omega^*} = \frac{d^2\boldsymbol{\theta}}{d^2\boldsymbol{\beta}}\,, \tag{1.63}$$

for an element of source $d^2\boldsymbol{\theta}$ mapped on to an area of image $d^2\boldsymbol{\beta}$. Therefore lensing effectively focuses the light towards our telescopes, so that we measure the light that would propagate towards us in the absence of lensing plus the extra photons that are deflected towards us as a result of lensing.

For a source which is much smaller than the angular size on which the properties of the lens vary, the lens mapping can locally be linearised and therefore we can define the Jacobian matrix of the lens equation as

$$\mathcal{A}(\boldsymbol{\theta}) = \frac{\partial\boldsymbol{\beta}}{\partial\boldsymbol{\theta}}\,, \text{with components}\,, \mathcal{A}_{ij} = \frac{\partial\beta_i}{\partial\theta_j}\,. \tag{1.64}$$

Thus the magnification factor is given by

$$|\mu| = \frac{1}{\det\mathcal{A}}\,, \tag{1.65}$$

for a small source. The magnification factor can be positive or negative which corresponds to positive or negative parity images. From the lens equation the Jacobian matrix can be written in the form

$$\begin{aligned}\mathcal{A}_{ij} &= \frac{\partial}{\partial\theta_j}(\theta_i - \alpha_i(\boldsymbol{\theta}) \\ &= \delta_{ij} - \frac{\partial\alpha_i(\boldsymbol{\theta})}{\partial\theta_j} \\ &= \delta_{ij} - \frac{\partial^2\psi(\boldsymbol{\theta})}{\partial\theta_i\partial\theta_j}\end{aligned} \tag{1.66}$$

$$\mathcal{A}(\boldsymbol{\theta}) = \begin{pmatrix} 1-\kappa-\gamma_1 & \gamma_2 \\ \gamma_2 & 1-\kappa+\gamma_1 \end{pmatrix}, \tag{1.67}$$

where we have introduced complex shear which has a magnitude $\gamma$ and orientation $\phi$,

$$\gamma = \gamma_1 + i\gamma_2 = |\gamma|e^{2i\phi}, \tag{1.68}$$

which can be decomposed into two components, given by

$$\gamma_1 = \frac{1}{2}\left(\frac{\partial^2\psi}{\partial\theta_1^2} - \frac{1}{2}\frac{\partial^2\psi}{\partial\theta_2^2}\right) = \gamma\cos 2\phi\,, \tag{1.69}$$

and

$$\gamma_2 = \frac{\partial^2\psi}{\partial\theta_1\partial\theta_2} = \gamma\sin 2\phi\,. \tag{1.70}$$

The magnification factor is therefore given by

$$\mu = \frac{1}{(1-\kappa)^2 - |\gamma|^2}\,. \tag{1.71}$$

Fig. 1.8 shows the outcome of applying convergence and shear to a circular source. The Jacobian lensing matrix can be re-written in a different form

$$\mathcal{A}(\boldsymbol{\theta}) = (1-\kappa)\begin{pmatrix} 1-g_1 & -g_2 \\ -g_2 & 1+g_1 \end{pmatrix}, \tag{1.72}$$

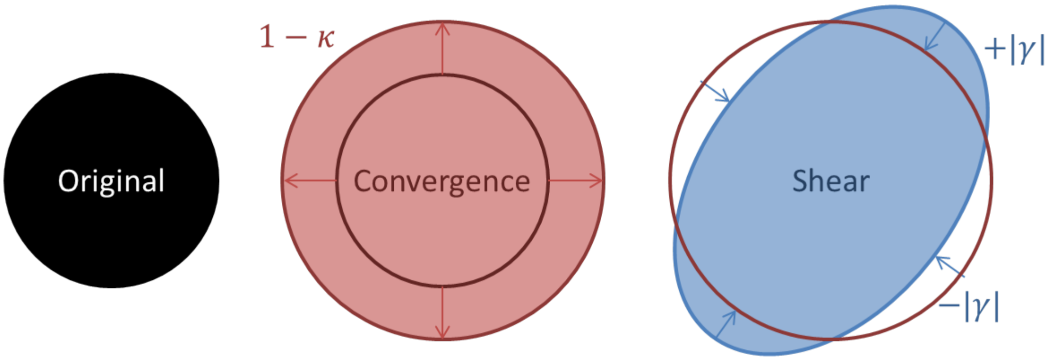


Figure 1.8: Gravitational lensing has the effect of magnifying and distorting the image of galaxy. The convergence term in equation 1.72, corresponds to an isotropic stretching, but does not change the shape of the galaxy image. The shear term corresponds to change in shape.

where we have used the reduced shear, $g = g_1 + ig_2$, which is defined as

$$g = \frac{\gamma}{1-\kappa} = \frac{|\gamma|}{1-\kappa} e^{2i\phi} \,. \tag{1.73}$$

From equation 1.72 it can be seen that the $(1-\kappa)$ factor corresponds to an isotropic stretching of the image but does not change the shape. The reduced shear contains information about the change in shape between the source image and the observed image. Showing results from Bartelmann & Schneider (2001), a circular source with unit radius is mapped onto an ellipse, with axes $|(1-\kappa)(1+|g|)|^{-1}$ and $|(1-\kappa)(1-|g|)|^{-1}$, and the orientation of the ellipse comes from the phase $\phi$ of $g$.

From our definition of the lensing potential, we can write the complex shear in terms of $\kappa$ as

$$\gamma(\boldsymbol{\theta}) = \frac{1}{\pi} \int d^2\theta' \mathcal{D}(\boldsymbol{\theta} - \boldsymbol{\theta}') \kappa(\boldsymbol{\theta}') \,, \tag{1.74}$$

with

$$\mathcal{D}(\boldsymbol{\theta}) = \frac{\theta_2^2 - \theta_1^2 - 2i\theta_1\theta_2}{|\boldsymbol{\theta}|^4} = \frac{-1}{(\theta_1 - i\theta_2)^2} \,. \tag{1.75}$$

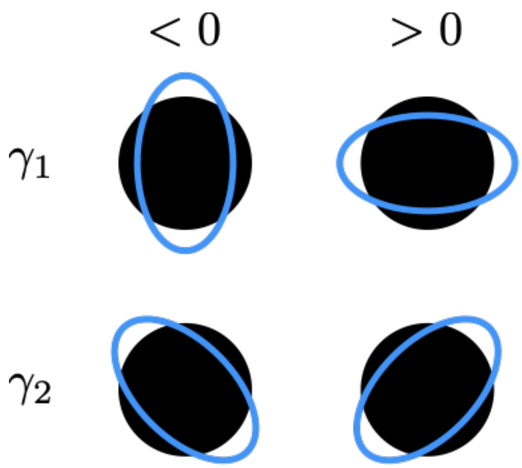


Figure 1.9: How the value of each shear component corresponds to galaxy shape.

### 1.2.6 Observing Weak Lensing

Having determined the relationships between the lensing potential $\psi$, convergence $\kappa$ and shear $\gamma$, we now aim to connect these quantities to properties we can measure from observations.

The quadrupole moment $Q_{ij}$ of a galaxy with a surface brightness $I(\boldsymbol{\theta})$ is given by

$$Q_{ij} = \frac{\int d^2\theta w[I(\boldsymbol{\theta})]I(\boldsymbol{\theta})\theta_i\theta_j}{\int d^2\theta w[I(\boldsymbol{\theta})]I(\boldsymbol{\theta})}, \tag{1.76}$$

where $w[I(\boldsymbol{\theta})]$ is a weighting function. The complex ellipticity is defined as $e = e_1 + ie_2$ where

$$\begin{pmatrix} e_1 \\ e_2 \end{pmatrix} = \frac{1}{Q_{11} + Q_{22}} \begin{pmatrix} Q_{11} - Q_{22} \\ 2Q_{12} \end{pmatrix}. \tag{1.77}$$

For a perfect ellipse, we can relate the ellipticity to the axial ratio $\tau$ at position angle $\phi$ as

$$\begin{pmatrix} e_1 \\ e_2 \end{pmatrix} = \frac{\tau^2 - 1}{\tau^2 + 1} \begin{pmatrix} \cos 2\phi \\ \sin 2\phi \end{pmatrix}, \tag{1.78}$$

where $\phi$ is measure anti-clockwise from the positive x-axis. By transforming the image quadrupole moment using the lensing Jacobian, as

$$Q^s_{ij} = \mathcal{A}_{il} Q_{lm} \mathcal{A}_{mj} \,, \tag{1.79}$$

we can relate the ellipticity of the image to the ellipticity of the source, which we require to be able to measure the lensing induced distortion. The complex ellipticity of the source $e^s$ can then be written as

$$e^s = \frac{e - 2g + g^2 e^*}{1 + |g|^2 - 2\mathcal{R}(ge^*)} \,, \tag{1.80}$$

where $e^*$ is the complex conjugate of $e$. For a weak lensing system $\kappa \ll 1$ and $|\gamma| \ll 1$, so that the reduced shear is approximately equal to the shear, $|g| \sim |\gamma|$ and $g^2 \approx 0$. In this regime the above equation can be reduced to

$$e_i = e^s_i + 2(\delta_{ij} - e^s_i e_j)\gamma_j \,. \tag{1.81}$$

This linear approximation has been shown to be suitable for $z < 1$ and $\theta > 5'$. However, the full non-linear equation should be used in practice since current surveys are reaching these limits. We continue with this result for ease of demonstration.

It is a fairly good approximation, neglecting intrinsic alignments (introduced in section 1.2.2), to assume that over a large region of sky, the intrinsic ellipticity of galaxies will be random so that when averaging over many galaxies $\langle e^s \rangle = 0$. In a left handed coordinate system $(x \to -x, y \to y)$, $e_1$ does not change but $e_2$ flips its sign. As a result any correlation between $e_1$ and $e_2$ will produce a null result $\langle e_1 e_2 \rangle = 0$. Noting this property of parity, when averaging over many source galaxies where the shear is constant, we find

$$\langle e_i \rangle = 2(1 - \langle e^s_i e_i \rangle)\gamma \,. \tag{1.82}$$

In the case of weak lensing $\langle e^s_i e_i \rangle \approx \langle e^2_i \rangle$, which can be estimated from the ellipticity dispersion of a large source galaxy sample as $\langle e_1^2 \rangle \approx \langle e_2^2 \rangle = \sigma_e^2$. For a sample of sources which are circular prior to being lensed $e^s = 0$, $\langle e_i e_i^s \rangle = 0$ the relationship between shear and ellipticity is given by

$$\gamma \simeq \frac{1}{2}\langle e \rangle \equiv \frac{1}{2}\langle e_1 + ie_2 \rangle \,. \tag{1.83}$$

In this thesis the shapes of the galaxies are estimated using a Bayesian likelihood-based method (Miller et al., 2013), in which a model of a galaxys surface brightness distribution is fitted to the data. These galaxy profiles are convolved with a model for the PSF which is based on fitting to images of stars. Galaxies are modelled as an exponential disk plus a bulge component. From the fitting procedure an estimate of the ellipticity and a weight which accounts for the uncertainty in the ellipticity are produced for each galaxy – together they form an estimate of the shear.

### 1.2.7 Weak Lensing by the Large Scale Structure

In the case of weak lensing by LSS, the mass in the LSS structure is located along the entire line-of-sight from the source to the observer. Thus our assumption that the lens is small compared the distance between the source and observer is not the case.

The propagation equation for a set of light rays, where one is a fiducial light ray, in Minkowski space with no perturbing mass present, is given by

$$\frac{d^2\boldsymbol{x}}{d\chi^2} + k\boldsymbol{x} = 0 \tag{1.84}$$

where $\boldsymbol{x}$ is the comoving separation between the two light rays, $\chi$ is the radial distance from the observer and $k$ is the space-time curvature of the Universe. The boundary condition requires the fiducial ray, which starts at the observer $\chi = 0$, has zero separation from the other light ray $\boldsymbol{x} = 0$, which propagates at an angle $\boldsymbol{\theta}$ meaning $\frac{d\boldsymbol{x}}{d\chi} = \theta$. The solution for the comoving separation vector in the unperturbed case is then

$$\boldsymbol{x}(\boldsymbol{\theta},\chi) = f_k(\chi)\boldsymbol{\theta}\,, \tag{1.85}$$

where $f_k(\chi)$ is the angular distance, which for a flat Universe $f_k(\chi) = \chi$.

When there are overdensities present, light is deflected following

$$\frac{d^2\boldsymbol{x}}{d\chi^2} = \frac{-2}{c^2}\nabla_\perp\Phi\,, \tag{1.86}$$

where $\Phi$ is the Newtonian potential of a localised density perturbation. The solution for the case of weakly perturbed Minkowski space is given by

$$\boldsymbol{x}(\boldsymbol{\theta},\chi) = f_k(\chi)\boldsymbol{\theta} - \frac{2}{c^2}\int_0^\chi d\chi\; f_k(\chi-\chi')\nabla_\perp\Phi[\boldsymbol{x}(\boldsymbol{\theta},\chi'),\chi']\,. \tag{1.87}$$

The overall deflection is then found by subtracting the unperturbed from the perturbed solution as

$$f_k(\chi)\alpha(\boldsymbol{\theta},\chi) = f_k(\chi)\boldsymbol{\theta} - \boldsymbol{x}(\boldsymbol{\theta},\chi)\,, \tag{1.88}$$

to get the deflection angle

$$\alpha(\boldsymbol{\theta},\chi) = \frac{2}{c^2}\int_0^\chi d\chi' \frac{f_k(\chi-\chi')}{f_k(\chi)}\nabla_\perp\Phi[f_k(\chi')\boldsymbol{\theta},\chi']\,. \tag{1.89}$$

Using our previously derived equation relating the deflection angle $\alpha$ to the convergence $\kappa$ we define an analogous effective convergence

$$\begin{aligned}\kappa_e(\boldsymbol{\theta},\chi) &= \frac{1}{2}\nabla_\theta\cdot\boldsymbol{\alpha}(\boldsymbol{\theta},\chi)\\ &= \frac{1}{c^2}\int_0^\chi \frac{f_k(\chi-\chi')f_k(\chi')}{f_k(\chi)}\frac{\partial^2}{\partial x_i\partial x_i}\Phi[f_k(\chi')\boldsymbol{\theta},\chi']\,,\end{aligned} \tag{1.90}$$

where we have used the fact that $\boldsymbol{x}(\chi') = f_k(\chi')\boldsymbol{\theta}$ and $\frac{\partial}{\partial\theta} = f_k(\chi')\frac{\partial}{\partial x}$.

The Newtonian potential $\Phi'$ is connected to the total matter density field, $\rho$ via

Poisson's equation

$$\nabla_\xi^2 \Phi' = 4\pi G \rho \, , \tag{1.91}$$

where $\rho = (1+\delta)\bar{\rho}$ and $\delta$ is the density fluctuation field. This is a linear equation so we can subtract the potential for the smooth background density field

$$\nabla_\xi^2 \bar{\Phi} = 4\pi G \bar{\rho} \, , \tag{1.92}$$

to find the perturbation potential. This is given by

$$\nabla_x^2 \Phi = 4\pi G a^2 \bar{\rho} \delta \, , \tag{1.93}$$

where we have implemented the gradient with respect to comoving coordinates $\nabla_x = a\nabla_\xi$ using the scale factor $a$. As previously shown, during matter domination $\bar{\rho} = a^{-3}\bar{\rho}_0$ such that

$$\nabla_x^2 \Phi = \frac{3\Omega_m H_0^3}{2a} \delta \, , \tag{1.94}$$

where we have used the parameter $\Omega_m = \frac{\rho}{\rho_c}$. From this form of the Poisson equation the effective convergence becomes

$$\kappa_e(\boldsymbol{\theta}, \chi) = \frac{3\Omega_m H_0^2}{2c^2} \int_0^\chi d\chi' \frac{f_k(\chi - \chi') f_k(\chi')}{f_k(\chi)} \frac{\delta[f_k(\chi')\boldsymbol{\theta}, \chi']}{a(\chi')} \, , \tag{1.95}$$

which is simply a weighted integral over the density fluctuations along the trajectory of the unperturbed light. By averaging the three-dimensional convergence, given above, over the normalised redshift distribution of the sources $p(\chi)$ we find the two-dimensional convergence projected along the line-of-sight as

$$\begin{aligned} \bar{\kappa}_e(\boldsymbol{\theta}) &= \int_0^{\chi_H} d\chi' p(\chi') \kappa_e(\boldsymbol{\theta}, \chi') \\ &= \frac{3\Omega_m H_0^2}{2c^2} \int_0^{\chi_H} d\chi' p(\chi') \int_0^{\chi'} d\chi \frac{f_k(\chi' - \chi) f_k(\chi)}{f_k(\chi')} \frac{\delta[f_k(\chi)\boldsymbol{\theta}, \chi]}{a(\chi)} \, , \end{aligned} \tag{1.96}$$

In this thesis we measure the convergence power spectrum, $C^{\kappa\kappa}(\ell)$. The power spectrum is the Fourier transform of the correlation function $\zeta(\theta)$, which is given by $\zeta(\theta) = \langle \bar{\kappa}_e^i(\boldsymbol{\theta})\bar{\kappa}_e^j(\boldsymbol{\theta'})\rangle$. Therefore from equation 1.96, the convergence correlation function is given by

$$\zeta(\theta) = \int d\chi W_i(\chi) \int d\chi' W_j(\chi) \langle \delta[f_k(\chi)\boldsymbol{\theta}, \chi]\delta[f_k(\chi')\boldsymbol{\theta'}, \chi']\rangle \,, \tag{1.97}$$

where we have introduced the weighting function

$$W_i(\chi) = \frac{3\Omega_m H_0^2}{2c^2}\frac{f_k(\chi)}{a(\chi)}\int_\chi^{\chi_H} d\chi' p_i(\chi')\frac{f_k(\chi'-\chi)}{f_k(\chi')} \,. \tag{1.98}$$

The power spectrum of the matter fluctuations $P$ is defined as

$$\langle \hat{\delta}(\boldsymbol{k},\chi)\hat{\delta}^*(\boldsymbol{k},\chi')\rangle = 2\pi^2\delta_D(\boldsymbol{k}-\boldsymbol{k'})P(|\boldsymbol{k}|,\chi) \,. \tag{1.99}$$

We can use equation 1.97 to write the correlation function of the convergence in terms of the matter fluctuation power spectrum

$$\begin{aligned} \zeta(\theta) = & \int d\chi W_i(\chi)\int d\chi' W_j(\chi')\int \frac{d^3k}{(2\pi)^3}\int\frac{d^3k'}{(2\pi)^3} \\ & \langle \hat{\delta}(\boldsymbol{k},\chi)\hat{\delta}^*(\boldsymbol{k},\chi')\rangle e^{-if_k(\chi)\boldsymbol{k}_\perp\cdot\boldsymbol{\theta}} e^{if_k(\chi')\boldsymbol{k'}_\perp\cdot\boldsymbol{\theta'}} e^{-ik_3\chi}e^{ik'_3\chi'} \\ = & \int d\chi W_i(\chi)\int d\chi' W_j(\chi')\int \frac{d^3k}{(2\pi)^3}\int d^3k'\delta_D(\boldsymbol{k}-\boldsymbol{k'}) \\ & P(|\boldsymbol{k}|,\chi) e^{-if_k(\chi)\boldsymbol{k}_\perp\cdot\boldsymbol{\theta}} e^{if_k(\chi')\boldsymbol{k'}_\perp\cdot\boldsymbol{\theta'}} e^{-ik_3\chi}e^{ik'_3\chi'} \,. \end{aligned} \tag{1.100}$$

Assuming small scale power in the density fluctuations that produce correlation when $\chi \approx \chi'$, we have

$$\zeta(\theta) = \int d\chi W_i(\chi)W_j(\chi)\int\frac{d^3k}{(2\pi)^3}P(|\boldsymbol{k}|,\chi)e^{-if_k(\chi)\boldsymbol{k}_\perp\cdot(\boldsymbol{\theta}-\boldsymbol{\theta'})}e^{-ik_3\chi}\int d\chi' e^{ik_3\chi'} \,. \tag{1.101}$$

Since $\int d\chi' e^{ik_3\chi'} = 2\pi\delta_D(k_3)$, and setting $\boldsymbol{\phi} = \boldsymbol{\theta}' - \boldsymbol{\theta}$,

$$\zeta(\phi) = \int d\chi W_i(\chi) W_j(\chi) \int \frac{d^2 k_\perp}{(2\pi)^2} P(|\boldsymbol{k}|, \chi) e^{i f_k(\chi) \boldsymbol{k}_\perp \cdot \boldsymbol{\phi}} . \tag{1.102}$$

The power spectrum $C^{\kappa\kappa}(\ell)$ is then given by

$$\begin{aligned} C^{\kappa\kappa}(\ell) &= \int d^2\phi e^{-i\boldsymbol{\ell}\cdot\boldsymbol{\phi}} \zeta(\phi) \\ &= \int d\chi W_i(\chi) W_j(\chi) \int \frac{d^2 k_\perp}{(2\pi)^2} P(|\boldsymbol{k}|, \chi) \int d^2\phi e^{i f_k(\chi)(\boldsymbol{k}_\perp - \boldsymbol{\ell})\cdot\boldsymbol{\phi}} \\ &= \int d\chi W_i(\chi) W_j(\chi) \int \frac{d^2 k_\perp}{(2\pi)^2} P(|\boldsymbol{k}|, \chi) (2\pi)^2 \delta_D(f_k(\chi)\boldsymbol{k}_\perp - \boldsymbol{\ell}) \\ &= \int d\chi \frac{W_i(\chi) W_j(\chi)}{f_k(\chi)^2} P\left(\frac{\ell}{f_k(\chi)}, \chi\right) . \end{aligned} \tag{1.103}$$

This shows that the power spectrum of convergence is essentially the matter power spectrum integrated along the line-of-sight weighted by the redshift distribution of sources.

### 1.2.8 Weak Lensing of the Cosmic Microwave Background

The CMB has travelled from the surface of last scattering, a distance of 14000Mpc away, to present times and therefore has been deflected by the many under and over-densities in the LSS it encounters. Therefore much of our discussion in the previous section, though specified for galaxies, is applicable here. In particular the relationship between convergence, the deflection angle, lensing potential and gravitational potential are all transferable since it is the same underlying physics. For a detailed review of CMB lensing see Lewis & Challinor (2006).

The CMB lensing signal is dominated by LSS between a redshift of 0.5 and 3. Gravitational lensing produces an apparent shift in the angular position of CMB photons. This effectively remaps both the temperature field $\Theta(\boldsymbol{n}) = \Delta T(\boldsymbol{n})/T$ and polarisation defined through the dimensionless Stokes parameters $Q(\boldsymbol{n})$ and $U(\boldsymbol{n})$

(Blanchard & Schneider, 1987). Thus, the deflection changes the statistical properties of the CMB anisotropies by inducing correlations between modes.

The CMB lensing field can be mapped using quadratic estimators, as described by Hu & Okamoto (2002), from measurements of the temperature and polarisation fields of the CMB. We outline this procedure here. For simplicity we focus on the temperature field, but a similar procedure can be performed for the polarisation fields. The remapping of the unlensed temperature field $\tilde{\Theta}$, is given by

$$\Theta(\boldsymbol{n}) = \tilde{\Theta}(\boldsymbol{n} + \boldsymbol{d}(\boldsymbol{n}))\,, \tag{1.104}$$

where $\boldsymbol{n}$ is the direction on the sky and the deflection $\boldsymbol{d}$ is analogous to the deflection angle $\boldsymbol{\alpha}$. The Fourier transform of the temperature is given by

$$\Theta(\boldsymbol{n}) = \int \frac{d^2\boldsymbol{\ell}}{(2\pi)^2}\Theta(\boldsymbol{\ell})e^{i\boldsymbol{\ell}\cdot\boldsymbol{n}}\,. \tag{1.105}$$

such that the change in the temperature field due to lensing potential $\phi$ is described by

$$\delta\Theta(\boldsymbol{\ell}) = \Theta(\boldsymbol{\ell}) - \tilde{\Theta}(\boldsymbol{\ell}) = -\int \frac{d^2\boldsymbol{\ell}}{2\pi}\boldsymbol{\ell}'\cdot(\boldsymbol{\ell}-\boldsymbol{\ell}')\phi(\boldsymbol{\ell}-\boldsymbol{\ell}')\tilde{\Theta}\boldsymbol{\ell}' + \ldots\,, \tag{1.106}$$

plus higher order terms. Assuming that the unlensed temperature field and the potential perturbation field is Gaussian and exhibits statistical isotropy, the unlensed covariance between modes is then

$$\langle\tilde{\Theta}(\boldsymbol{\ell})\tilde{\Theta}(\boldsymbol{\ell}')\rangle = \tilde{C}_\ell^{\Theta\Theta}\delta(\boldsymbol{\ell}+\boldsymbol{\ell}')\,, \tag{1.107}$$

i.e., there is no coupling between modes. We can also define the observed temperature power spectrum

$$\langle\Theta(\boldsymbol{\ell})\Theta(\boldsymbol{\ell}')\rangle \equiv C_\ell^{\Theta\Theta}\delta(\boldsymbol{\ell}+\boldsymbol{\ell}')\,, \tag{1.108}$$

where the power spectrum includes all components of noise too. The effect of the lensing is to mix and correlate Fourier modes of the CMB. For a fixed lensing field, we can consider averaging over an ensemble of realisations as

$$\langle \Theta(\boldsymbol{\ell})\Theta(\boldsymbol{\ell}')\rangle = f_{\Theta\Theta}(\boldsymbol{\ell},\boldsymbol{\ell}')\phi(\boldsymbol{L})\,, \tag{1.109}$$

where $\boldsymbol{L} = \boldsymbol{\ell} + \boldsymbol{\ell}' \neq 0$, and $f_{TT'}$ is the pair response function which measures the correlation between CMB modes as a result of lensing mode $\phi(\boldsymbol{L})$. Since $\phi$ is also statistically isotropic, such that $\langle \phi(\boldsymbol{L})\rangle = 0$, we cannot simply reconstruct lensing from the expectation value of the CMB modes. However, the above equation does suggest that there is a suitable way to average over pairs of multipoles to estimate the lensing deflection field. We now step through this procedure.

From equation 1.105

$$\begin{aligned}\Theta(\boldsymbol{\ell})\Theta(\boldsymbol{\ell}') &= \tilde{\Theta}(\boldsymbol{\ell})\tilde{\Theta}(\boldsymbol{\ell}'') \\ &- \int \frac{d^2\ell''}{2\pi}[\boldsymbol{\ell}''\cdot(\boldsymbol{\ell}-\boldsymbol{\ell}'')\phi(\boldsymbol{\ell}-\boldsymbol{\ell}'')\Theta(\boldsymbol{\ell}')\tilde{\Theta}(\boldsymbol{\ell}'') + \boldsymbol{\ell}''\cdot(\boldsymbol{\ell}'-\boldsymbol{\ell}'')\phi(\boldsymbol{\ell}'-\boldsymbol{\ell}'')\tilde{\Theta}(\boldsymbol{\ell})\tilde{\Theta}(\boldsymbol{\ell}'')] + \dots\,.\end{aligned} \tag{1.110}$$

Taking the expectation value as in equation 1.109

$$\begin{aligned}\langle\Theta(\boldsymbol{\ell})\Theta(\boldsymbol{\ell}')\rangle &= \delta(\boldsymbol{\ell}+\boldsymbol{\ell}')\tilde{C}_\ell^{\Theta\Theta} \\ &- \int \frac{d^2\boldsymbol{\ell}''}{2\pi}[\boldsymbol{\ell}''\cdot(\boldsymbol{\ell}-\boldsymbol{\ell}'')\phi(\boldsymbol{\ell}-\boldsymbol{\ell}'')\delta(\boldsymbol{\ell}'+\boldsymbol{\ell}''\tilde{C}_{\ell'}^{\Theta\Theta} + \boldsymbol{\ell}''\cdot(\boldsymbol{\ell}'-\boldsymbol{\ell}'')\phi(\boldsymbol{\ell}'-\boldsymbol{\ell}'')\delta(\boldsymbol{\ell}+\boldsymbol{\ell}''\tilde{C}_{\ell}^{\Theta\Theta}] + \dots\,,\end{aligned} \tag{1.111}$$

which becomes

$$\langle\Theta(\boldsymbol{\ell})\Theta(\boldsymbol{\ell}')\rangle = \frac{1}{2\pi}[\tilde{C}_\ell^{\Theta\Theta}(\boldsymbol{L}\cdot\boldsymbol{\ell}) + \tilde{C}_{\ell'}^{\Theta\Theta}(\boldsymbol{L}\cdot\boldsymbol{\ell}')]\phi(\boldsymbol{L}) + \mathcal{O}(\phi^2)\,. \tag{1.112}$$

Thus for a fixed lensing realisation, statistical isotropy is no longer true, and the temperature power spectrum is distorted. We can define a lensing estimator which, since the effect of lensing is to couple CMB modes, is quadratic in the observed CMB fields

$$\hat{\phi}_{\Theta\Theta}(\boldsymbol{L}) = A_{\Theta\Theta}(\boldsymbol{L}) \int d^2\boldsymbol{\ell} F_{\Theta\Theta}(\boldsymbol{\ell}, \boldsymbol{L}-\boldsymbol{\ell})\Theta(\boldsymbol{\ell})\Theta'(\boldsymbol{L}-\boldsymbol{\ell})\,, \tag{1.113}$$

where $A_{\Theta\Theta}$ is the normalisation and $F_{\Theta\Theta}$ is a filter which weights pairs of CMB nodes.

In deriving the lensing estimator, $\hat{\phi}$, we require an estimator which is unbiased to first order in the lensing potential, $\langle\hat{\phi}_{\Theta\Theta'}(\boldsymbol{L})\rangle = \phi(\boldsymbol{L})$, and that $\hat{\phi}$ is a minimum variance estimator. The second condition means that $\langle\hat{\phi}_{\Theta\Theta}(\boldsymbol{L})\hat{\phi}_{\Theta\Theta}(\boldsymbol{L}')\rangle$ is minimised with respect to filter $F_{\Theta\Theta}$, which determines the exact form of the filter.

By combining the normalisation and filter terms, we have the generic quadratic estimator

$$\hat{\phi}_{\Theta\Theta}(\boldsymbol{L}) = \int d^2\boldsymbol{\ell} G_{\Theta\Theta}(\boldsymbol{\ell}, \boldsymbol{L}-\boldsymbol{\ell})\Theta(\boldsymbol{\ell})\Theta'(\boldsymbol{L}-\boldsymbol{\ell})\,. \tag{1.114}$$

Here we quote the results from Hu & Okamoto (2002) as

$$A_{\Theta\Theta}(\boldsymbol{L}) = \left[\int d^2\boldsymbol{\ell} F_{\Theta\Theta}(\boldsymbol{\ell}, \boldsymbol{L}-\boldsymbol{\ell}) f_{\Theta\Theta}(\boldsymbol{\ell}, \boldsymbol{L}-\boldsymbol{\ell})\right]^{-1}\,, \tag{1.115}$$

and

$$F_{\Theta\Theta}(\boldsymbol{\ell}, \boldsymbol{L}-\boldsymbol{\ell}) = \frac{f_{\Theta\Theta}(\boldsymbol{\ell}, \boldsymbol{L}-\boldsymbol{\ell})}{2C_\ell^{\Theta\Theta}C_{|\boldsymbol{L}-\boldsymbol{\ell}|}^{\Theta\Theta}}\,, \tag{1.116}$$

which is essentially a signal-to-noise weighting for each pair of modes. Filters for polarisation and cross-terms can be found in a similar manner, which are detailed in Hu & Okamoto (2002).

Now substituting into the equation for the lensing estimator

$$\frac{\hat{\phi}_{\Theta\Theta}(\boldsymbol{L})}{A_{\Theta\Theta}(\boldsymbol{L})} = \int d^2\boldsymbol{\ell} \left[\frac{\tilde{C}_\ell^{\Theta\Theta}(\boldsymbol{L}\cdot\boldsymbol{\ell})}{C_\ell^{\Theta\Theta}}\Theta(\boldsymbol{\ell})\right]\left[\frac{1}{C_{|\boldsymbol{L}-\boldsymbol{\ell}|}^{\Theta\Theta}}\Theta(\boldsymbol{L}-\boldsymbol{\ell})\right]\,, \tag{1.117}$$

which we can evaluate by first noting that this is a convolution in Fourier space and therefore a multiplication in real space.

Here we have demonstrated a standard method for estimating lensing from CMB data, this estimator has been commonly used in CMB lensing analyses (for example Sherwin et al., 2017). However, new techniques which are robust against foreground biases are now feasible and producing results with competitive signal-to-noise (Madhavacheril & Hill, 2018).

## 1.3 Observational Probes of Cosmology

In this section we review the current status of cosmological observations and the next generation of experiments.

### 1.3.1 The Cosmic Microwave Background

The CMB was first discovered in 1965 (Penzias & Wilson, 1965; Dicke et al., 1965), with CMB anisotropies first being revealed by the COBE satellite (Smoot et al., 1992) which solidly rooted the CDM model of the Universe, followed by WMAP (Spergel et al., 2003; Dunkley et al., 2009) which established that fluctuations are largely adiabatic. To date, observations of the CMB have been made from ground based telescopes (mainly in Chile and the South Pole), balloons and space, covering a variety of frequencies, depths, sky coverage and therefore science goals.

The current and next generation of CMB experiments are now considering extensions to the ΛCDM model and open questions including inflation, dark matter, neutrinos, the dark energy equation of state and modifications to General Relativity. These observations also offer the opportunity to investigate the late-time Universe through secondary effects such as weak gravitational lensing of the CMB and galaxy clusters detected via the thermal Sunyaev-Zel'dovich effect. Here we summarise the status of current and future CMB experiments.

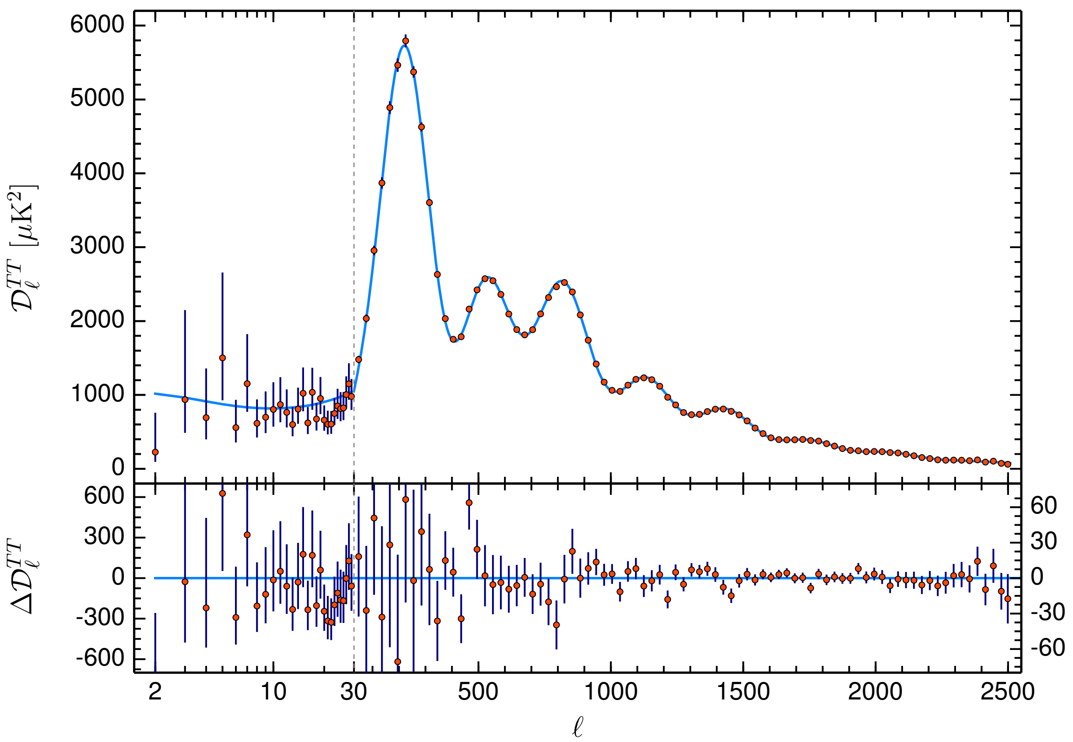


Figure 1.10: The temperature auto-spectrum from Planck Collaboration (2018).

*Planck* is a European Space Agency mission which observed the full sky in a wide range of frequencies (30GHz–857GHz). It was launched in 2009 and observed until 2013 and to date provides the tightest constraints on cosmological parameters. The temperature auto-spectrum is shown in Fig. 1.10. The *Planck* satellite has produced the best measurements of the anisotropy spectra and therefore the tightest constraints (Planck Collaboration, 2018).

The Atacama Cosmology Telescope (ACT) is a six metre microwave telescope located in Northern Chile at an altitude of 5190m. Observations began in 2008 using the MBAC camera, making temperature measurements covering $\sim 100$ deg$^2$ (Louis et al., 2017). This was upgraded to ACTPol in 2013 so that both temperature and polarisation measurements could be made. ACT observes in two frequency channels, 90GHz and 150GHz. Its design means it benefits from high resolution which is important for measuring the large-$\ell$ CMB and makes it an ideal tool for CMB lensing and SZ cluster detections. ACT has undergone a further upgrade to AdvancedACT which is currently mapping a huge area of $\sim 20,000$ square degrees in the south.

The South Pole Telescope (SPT, Hanson et al., 2013; Keisler et al., 2015) is a ten metre telescope located in Antarctica at the Amundson-Scott station. The aim of the project was to measure high resolution CMB fluctuations and detect galaxy clusters through the SZ effect over large areas of sky. Similar to ACT the telescope has undergone various upgrades which include three different cameras, SPT-SZ, SPTpol and SPT-3G, over ten years of observing. SPT benefits from overlapping area with the Dark Energy Survey and has been used in combined cosmology analyses as a result Baxter et al. (2016); Kirk et al. (2016); Omori et al. (2019a,b) and for investigations into the SZ and X-ray cluster mass scaling relations (Dietrich et al., 2019).

PolarBear and Simons Array are a series of dishes in the Atacama desert in Chile (Polarbear Collaboration et al., 2014). PolarBear has a 2.5m telescope and observes a small area of sky in the 95GHz and 150GHz frequency channels. It observes purely polarisation and so has been used primarily in the search for B-modes and understanding gravitational lensing. The cross-correlation between CMB lensing purely from polarisation and galaxy weak lensing with Hyper Suprime Cam was reported in Namikawa et al. (2019) for the first time. Although this was a low signal-to-noise detection, this detection paves the way for future experiments and is important since CMB lensing reconstructed from polarisation should contain fewer systematic effects compared to those reconstructed from temperature measurements.

There are several other experiments that are also focused on detecting primordial gravitational waves using ground based telescopes, including the Background Imaging of Cosmic Extragalactic Polarisation (BICEP, Ade et al., 2018) and Keck array, the Cosmology Large Angular Scale Surveyor (CLASS, Marriage et al., 2014) and the Q-U-I Joint Tenerife Experiment (QUIJOTE, López-Caniego et al., 2014) and balloon experiments SPIDER (Crill et al., 2008) and the E and B Experiment (EBEX, EBEX Collaboration et al., 2018).

Simons Observatory will be the next advancement in CMB ground based experiments, due to see first light in 2020, located at the same site at ACT and the Simons Array in the Atacama desert, Chile (Ade et al., 2019). It will consist of an ACT like 6m telescope, plus three 0.5m telescopes, with the large aperture telescope observing 40% of the sky. It will therefore benefit from large overlap with LSS surveys (see below). Simons Observatory will also cover a wider frequency range over six channels with a total of 60,000 detectors, an order of magnitude greater than any current experiment.

### 1.3.2 Local $H_0$ Estimates

There are two primary approaches for determining the Hubble constant, $H_0$, using data from the local Universe. The first is calibrating stellar luminosities and distances to nearby galaxies, which has mainly been achieved using Cepheid variable stars. The second is calibrating more luminous objects – usually Type Ia supernovae – which extends measurements much further, well into the smooth Hubble flow. The method for measuring distances from Cepheids has been well checked – Cepheids are found in optical data and then observed at longer wavelengths to minimise corrections due to dust extinction. Geometric parallax measurements of Milky Way stars are used to secure the Cepheid distance scale. At larger distances, out to cosmological redshifts of $z \sim 0.1$ , the peak brightness of Type Ia supernovae is measured. These measurements are then calibrated with Cepheid variable stars located in local galaxies that have good observations of Type Ia supernovae (Freedman, 2017).

These local measurements (Benedict et al., 2007; Freedman et al., 2012; Humphreys et al., 2013; Riess et al., 2016) have produced a value of $H_0$ consistent with $73 kms^{-1}\mathrm{Mpc}^{-1}$, with a few percent error budget. The H0LiCoW data set, which uses time delay measurements from gravitational lensing systems has also yielded results consistent with other local Universe $H_0$ measurements (Bonvin et al., 2017). These are currently in tension with the value of $H_0$ inferred from *Planck* primary CMB data, which imply a lower $H_0$ value of $67kms^{-1}\mathrm{Mpc}^{-1}$ (Planck Collaboration, 2018).

### 1.3.3 Weak Gravitational Lensing

The first measurements of weak gravitational lensing by LSS were made in 2000 (Bacon et al., 2000; Van Waerbeke et al., 2000; Wittman et al., 2000). We have already thoroughly introduced this topic in section 1.2, so here we summarise the current status of experiments. Currently there are three collaborations all striving to obtain the tightest constraints on late-time cosmology from weak lensing.

The Kilo Degree Survey (KiDS) is an optical imaging survey, which in its final state will have imaged $\sim 1350\mathrm{deg}^2$ over two regions in four filters $(u, g, r, i)$ (Kuijken et al., 2019; Hildebrandt et al., 2018). KiDS uses the VLT Survey Telescope located in Northen Chile at the Paranal observatory. In parallel, the VISTA Kilo-Degree Infrared Galaxy survey (VIKING) project covers the same area in five near-infrared bands: $Z, Y, J, H, K$, so that the two data sets form a 9-band survey. The number density of galaxies is $\sim 7\,\mathrm{arcmin}^{-2}$ and the redshift range is $0.1 < z < 1.2$. The final data set from KiDS will extend out to a redshift of 2.

The Dark Energy Survey (DES) observed around $5000\mathrm{deg}^2$ of the Southern sky using the four metre Victor M. Blanco Telescope, in Chile, outfitted with the Dark Energy Camera (Troxel et al., 2018). DES observes in five bands – $g, r, i, z$, and $Y$. The number density of galaxies is $\sim 6\,\mathrm{arcmin}^{-2}$ and the redshift range is $0.2 < z < 1.3$.

The Hyper Suprime Cam (HSC) survey is an ongoing five band $(g, r, i, z, y)$ imaging survey using the eight metre Subaru telescope on Mauna Kea in Hawaii (Aihara et al., 2018; Hikage et al., 2019). Once complete it will have covered 1400 square degrees of sky. The number density of galaxies is $\sim 22\,\mathrm{arcmin}^{-2}$ and the redshift

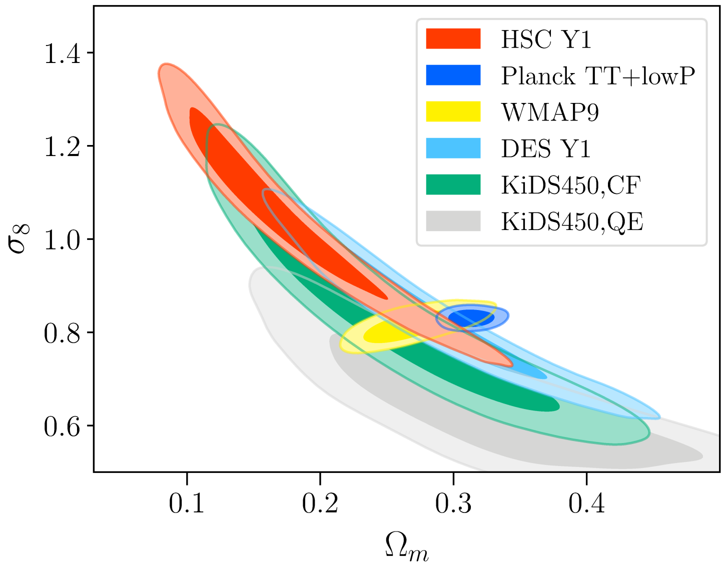


Figure 1.11: Constraints on $\Omega_m$ and $\sigma_8$ from the three current state of the art weak lensing surveys (Hikage et al., 2019). These three surveys show relatively good agreement, with a mild tension with primary CMB measurements from *Planck* (Planck Collaboration, 2018).

range is $0.3 < z < 1.5$.

The current constraints – on $\sigma_8$ and $\Omega_m$ – from the three surveys described above is shown in Fig. 1.11. It is clear that there is a relatively good agreement between these surveys, and a mild tension between weak lensing constraints and primary CMB measurements from *Planck* (Planck Collaboration, 2018).

Soon the next generation of weak lensing experiments will come online covering a huge area of sky. The Large Synoptic Survey Telescope (LSST), located in Chile, will observe 30,000 deg$^2$ of sky in six bands $u, g, r, i, z, y$ and have a number density of 26 arcmin$^{-2}$ (Ivezić et al., 2019). The *Euclid* space telescope is currently being developed by the European Space Agency (Amendola et al., 2013). It is due to be launched in 2022, and over a six year period will observe about a third of the extragalactic sky – avoiding the Milky Way. To obtain accurate photometric redshifts, observations in four other bands will be made from ground based telescopes, so that each galaxy is observed in 7 filters. The predicted number density of galaxies used for weak lensing measurements is 30 arcmin$^{-2}$.

### 1.3.4 The Large Scale Structure

Large Scale Structure (LSS) surveys aim to probe the distribution of galaxies. This is most commonly done by quantifying the degree of clustering observed by measuring correlation functions or power spectra. To measure the clustering signal requires knowing the locations of galaxies in three-dimensions. When measuring the correlation functions of galaxies, baryons imprint a signature feature. In the early Universe ionised gas cannot cluster due to radiation pressure. This pressure generates relativistic sound waves which transmit up to $z \sim 1000$, when the Universe becomes neutral. As a result of the sounds waves, acoustic oscillations can be seen in the CMB anisotropy observations and also imprint faint signature 'bump' on the clustering of galaxies. These features are referred to as Baryon Acoustic Oscillations (BAOs) (Eisenstein et al., 2005).

Measurements of BAOs have so far provided substantial support for the ΛCDM paradigm. Important measurements include the Sloan Digital Sky Survey (SDSS, Eisenstein et al., 2005), 2-degree Field Galaxy Redshift Survey (2dFRGS, Colless et al., 2001), WiggleZ (Blake et al., 2012), 6-degree Field Galaxy Survey (6dFGS, Beutler et al., 2011), the Baryon Oscillation Spectroscopic Survey (BOSS, Anderson et al., 2014) – which produced the first BAO measurements with precision better than 1% – and finally extended BOSS (eBOSS, Zhai et al., 2017). eBOSS is the largest spectroscopic survey to date and uses data from SDSS-IV. It contains around 80,000 galaxies with an effective sample redshift of $z = 0.72$. Upcoming surveys will include the Taipan survey which will observe around 2 million galaxies across 50% of the sky at low redshift. At higher redshifts, the Dark Energy Spectroscopic Instrument (DESI, DESI Collaboration et al., 2016), the 4MOST Cosmology Redshift Survey (de Jong et al., 2012), *Euclid* (Amendola et al., 2013) will observe many more galaxies.

Photometric surveys can also be used to measure galaxy clustering in tomographic redshift bins – for example, this is already being done for DES and is planned for LSST.

### 1.3.5 Galaxy Clusters

Since clusters have multiple components they can be seen across the electromagnetic spectrum. Clusters can be observed primarily in three wavebands  optical, X-ray and millimetre, which provides the opportunity to observe the same objects with independent measurement procedures (Allen et al., 2011). In the optical part of the spectrum, the cluster galaxies, and the gravitational lensing effect of the cluster on the background galaxies can be measured. Radial velocities of cluster galaxies can be gained from accurate measurements of the redshift of constituent galaxies. X-rays are emitted by clusters because a cluster is essentially a massive gravitational potential well that compresses and as a result heats the trapped gas to X-ray temperatures. Thus the X-ray luminosity, the temperature of the X-ray spectrum and element abundances seen in the X-ray spectra can be inferred. Due to the huge amounts of gas found in clusters, which makes up ICM, Comic Microwave Background (CMB) photons are inverse Compton scattered off the ICM causing the Sunyaev-Zeldovich Effect (Sunyaev & Zel'dovich, 1972). Thus we can find clusters with CMB data sets.

Using these methods galaxy cluster samples have been compiled, with the *Planck* satellite producing a catalogue of 1200 clusters through the SZ effect (Planck Collaboration, 2016). Advanced ACT will yield a sample more than twice as large and looking into the future, SO is expected to observe 20,000 clusters (Ade et al., 2019). Optical imaging surveys have also created large catalogues and can probe lower masses, using the cluster red sequence – the DES redmapper catalogue contains 786 clusters (Zhang et al., 2019). Upcoming surveys like LSST and *Euclid* will produce much larger cluster samples (Amendola et al., 2013). Finally in the X-ray, of order a few hundred clusters have been found using the XMM-Newton telescope (Mehrtens et al., 2012) and ROSAT All-Sky Survey (Böhringer et al., 2017). The latest X-ray telescope eROSITA, launched in July 2019, is anticipated to observe 100,000 clusters (Hofmann et al., 2017).

Clusters have been used to infer cosmological parameters from previous samples (e.g., Kaiser, 1986; Peebles et al., 1989; Kaiser, 1991; Barbosa et al., 1996; Komatsu & Kitayama, 1999; Holder et al., 2001; Komatsu & Seljak, 2002; Battye & Weller, 2003; Voit, 2005). From the *Planck* cluster sample, parameter constraints on the $\Omega_m - \sigma_8$ plane have been found to be very mildly in tension with *Planck* primary CMB measurements (Planck Collaboration, 2018). Measuring cluster masses has been shown to be the largest source of uncertainty in cluster cosmology and may explain this small discrepancy (see e.g Vikhlinin et al., 2009; Rozo et al., 2010; Vanderlinde et al., 2010; Sehgal et al., 2011; Benson et al., 2013; Hasselfield et al., 2013; Mantz et al., 2014, 2015; Planck Collaboration, 2016; de Haan et al., 2016). This is the topic of chapter 4.

### 1.3.6 The Big Picture

The cosmological probes described above provide huge support for the $\Lambda$CDM paradigm, and it is quite incredible that such agreement has been shown amongst such a diverse array of observations. However, we have seen some discrepancies in parameter constraints between high and low redshift probes. Although at this stage these tensions are only mild, the next generation of surveys will improve the measurement accuracy such that it may become significant.

If the tension remains new physics may be required which would need to reduce the rate of clustering between recombination and the present. There have been several studies into understanding this tension. Considering the tension between weak lensing and the primary CMB, studies so far (Joudaki et al., 2017; MacCrann et al.,

2015) have shown that known systematic effects do not lead to a large enough shift in parameter constraints, to produce consistent results from both data sets. When considering departures from ΛCDM, including massive neutrinos, non-zero curvature, modified gravity and running of the scalar spectral index have been found not to remedy this tension and in the case of massive neutrinos actually increase the tension between the CMB and type-Ia supernovae $H_0$ measurements. The tension has been shown to be somewhat alleviated with an evolving dark energy, with a time dependent equation of state (Joudaki et al., 2017). This is certainly an open question in cosmology and one that we would like to answer with the next generation of telescopes.

In this thesis we use CMB and weak gravitational lensing data sets together with aim of improving our understanding of cosmology. In Chapter 2 we outline the theoretical framework for the analyses presented in the following chapters. In Chapter 3 we develop the methodology used to measure the cross-correlation power spectrum between CMB lensing and galaxy weak lensing data, and detail analysis choices which can impact the measured signal. In Chapter 3 we present the cross-correlation between CMB lensing from the Atacama Cosmology Telescope and galaxy weak lensing from the Kilo Degree Survey plus expectations for the next data sets from these two experiments. Finally in Chapter 4 we investigate the hydrostatic mass bias – currently the limiting factor in cluster cosmology. To do this, we measure the masses of galaxy clusters, selected via the thermal Sunyaev-Zel'dovich effect, using gravitational lensing. Our conclusions and a discussion of future work is included in Chapter 5.

# Chapter 2

# Pseudo-$C_\ell$ Estimation for Weak Lensing Cross-correlations

## 2.1 Introduction

Interpreting observations of the Universe to extract cosmology requires the use of summary statistics to compress the data. These statistics need to be constructed such that the maximal information is retained and a range of cosmological models can be compared. Gaussian distributed data is fully described by 2-point statistics, making them a natural choice for CMB analyses (Górski, 1994; Bond, 1995; Tegmark, 1997; Tegmark & de Oliveira-Costa, 2001). When considering the late-time density field, non-linear evolution produces higher order correlations, meaning that some information will not be retained in 2-point statistics. However, most of the information in the density field is captured, and as a result this has become the common approach to understanding observations in the context of cosmological models. Consequently, there has been a drive towards optimally measuring 2-point statistics (Bond et al., 1998; Wandelt & Hansen, 2003; Eriksen et al., 2004; Taylor et al., 2008; Bonvin & Durrer, 2011; Asorey et al., 2012; Alsing et al., 2016; Vanneste et al., 2018).

In this chapter we develop a pipeline to measure the cross-correlation power spectrum between CMB lensing and GWL data sets. The power spectrum statistic is a natural choice for CMB analyses since CMB data consists of large smooth maps with simple masks. The covariance on the full-sky is diagonal for Gaussian perturbations with no masking, and decomposing the polarisation signal into divergence-like E and curl-like B modes is somewhat simpler in Fourier[1] space – but still problematic on a cut sky. Galaxy surveys, however, usually cover a much smaller area of sky and suffer from around 10% of an observed region being masked due to bright stars or galaxies, image ghosts, bad CCD pixels or columns and cosmic rays. This produces a complicated mask causing many issues for Fourier space analyses, including a decrease in power since there are a large number of zeros in the masked map. The sharp boundaries of the map also result in mode leakage and independent modes become coupled – this produces a biased estimate of the power spectrum and covariance. As a consequence, most GWL studies have used the real space 2-point correlation function, $\xi_{\pm}(\theta)$ (e.g Heymans et al., 2012; Hildebrandt et al., 2017; Troxel et al., 2018). There are, however, arguments to be made for a Fourier analysis (Hikage et al., 2019), since in the real space 2-point correlation function, linear and non-linear scales of the galaxy shear field are mixed. This is an issue since the baryonic effects that dominate the non-linear scales are poorly understood and therefore difficult to model. Another argument for Fourier space is that the covariance matrix becomes diagonal and is much faster and easier to estimate exactly.

With a power spectrum analysis it is useful to interpolate the shear field, which is sampled by lensed galaxies, into a two-dimensional pixelised map, covering one or more redshift bins. In this case, a mask must be defined by the location of the lensed galaxies in our catalogue. Stars which are located close to galaxies on an image can interfere with the shape measurement of the galaxy and must therefore be masked

[1] In this chapter, the term 'Fourier space' can be interchanged with 'harmonic space' unless specified.

along with any contaminated galaxies – this produces a complicated mask with many features. This masking means that we cannot measure the true power spectrum $C_\ell$. Instead we can measure the pseudo-power spectrum, which is a technique based around estimating an analytical prediction for what this bias is and then correcting for it (e.g., Peebles, 1973; Wandelt et al., 2001; Szapudi et al., 2001; Hivon et al., 2002; Hansen et al., 2002; Chon et al., 2004; Tristram et al., 2005; Asgari et al., 2018). This method relates the observed power spectrum, $\widetilde{C}_\ell$, to the true power spectrum, $C_\ell$, which is predicted from theory, via a mode coupling matrix which describes the effect of a mask applied to data. This estimator is one of a variety of quadratic minimum variance estimators (see Efstathiou, 2004, for a full discussion), which has a large reduction in computational time from analytical and numerical simplifications based on the assumption that the covariance matrix of the data is diagonal in real space. In practice this means that a pseudo-power spectra analysis is appropriate when the power spectra do not vary steeply and the correlation length is smaller than the mask structures. These assumptions are true for the data sets we are interested in.

Several public codes exist which measure pseudo-spectra, including LensCross (Hand et al., 2015), PolSpice (Challinor et al., 2011) and NaMaster (Alonso et al., 2019). LensCross and PolSpice were originally built for CMB analyses, but have also been applied to LSS data sets.

LensCross was used in the first lensing-lensing cross-correlation between ACT CMB lensing and CS82 GWL (Hand et al., 2015) and uses flat-sky approximations. It is built on the CMB power spectrum code described in Louis et al. (2014). This pipeline first converts the smoothed galaxy shear maps into a convergence map, as described in more detail in Sec 2.2. The outer boundary of the binary galaxy mask is then apodised with a Gaussian and the resulting mask is applied to both convergence maps. From the two masked convergence fields, a 2D pseudo-power spectrum is calculated which is then converted into a 1D spectrum by averaging in annuli. The inverse of the binned mode coupling matrix is applied to the estimated 1D spectrum to recover an unbiased estimate of the cross-correlation power spectrum. LensCross is a flat-sky code, so when looking to the next generation of surveys it will no longer be applicable. It also does not allow for different masks for each data set and can only be used with spin-0 fields. It should also be noted that the method for transforming shear into convergence is inaccurate in the presence of a mask.

PolSpice was built to be applied to polarisation fields and thus can be used directly with the spin-2 shear field, bypassing the need for convergence reconstruction. PolSpice is a curved sky code which works with HEALPix (Górski et al., 2005) maps – therefore projection effects must be considered if the data is in another pixelisation format. The code first computes the pseudo-power spectra of the maps and mask, then transforms the results into configuration space. The correlation functions are then premultiplied by an apodisation function in order to reduce correlations between $\ell-$modes which result from partial sky coverage, which is then transformed back into Fourier space. The resulting power spectrum can then be binned appropriately. It was used in the cross-correlation between DES GWL and SPT lensing (Kirk et al., 2016).

Finally, the NaMaster code[2] is more similar to LensCross, handling the effects of the mask through a mode coupling matrix. It is, however, a more flexible software package, since it can applied to a spin-2 field, a different mask and weight map can be used for each field and it has both flat and curved sky options without the need to use a HEALPix pixelisation. This makes it a more natural choice for cross-correlation measurements since the properties of the different data sets can be included in the analysis and will still be relevant to the next generation of surveys. Therefore we choose NaMaster as the basis for our new cross-correlation pipeline.

In this chapter we develop this new pipeline, using NaMaster, and reproduce

[2]https://github.com/LSSTDESC/NaMaster

existing results using public data from the ACT and CS82 surveys (Hand et al., 2015). We then test it further using simulations appropriate for upcoming CMB lensing and GWL data. We test the robustness of the pipeline to the complicated nature of GWL data sets and investigate ways to improve the signal-to-noise of the cross-correlation measurement. The procedure for measuring the cross-correlation power spectra is outlined in section 2.2, including how we theoretically predict the power spectrum and estimate error bars. The simulations and data used in this chapter are explained in section 2.3 and our results presented in section 2.4. We conclude with a discussion of our findings in section 2.5.

## 2.2 Formalism and Methods

In this section we outline the basic formalism for estimating the power spectrum for the CMB lensing/GWL cross-correlation, starting with a GWL data catalogue and a map of CMB lensing convergence. We do this for a flat-sky approximation as the formalism is simpler than the full-sky case. In the flat-sky case, the expansion in spherical harmonics is replaced by an expansion in Fourier modes – this is a small angle approximation which can be used at large $\ell$. This follows the more detailed formalism and results shown in Alonso et al. (2019) and Asgari et al. (2018).

### 2.2.1 Galaxy Weak Lensing Maps

We start from a catalogue of source galaxies which trace the shear field – a galaxy, $i$, has a position on the sky, $[\alpha_i, \delta_i]$, an estimate of two components of shear, $[\gamma_{i,1}, \gamma_{i,2}]$ and a weight, $w_i$. We make a map of the shear field by finding the average value of

$[\gamma_1, \gamma_2]$ from the galaxies located in a pixel centred on $\boldsymbol{\theta}$, as

$$\gamma_n(\boldsymbol{\theta}) = \frac{\sum_i \Theta_i(\boldsymbol{\theta}) w_i \gamma_{i,n}}{\sum_i \Theta_i(\boldsymbol{\theta}) w_i} \quad , \quad \Theta_i(\boldsymbol{\theta}) = \begin{cases} 1, & \text{if galaxy } i \text{ is in the pixel centred on } \boldsymbol{\theta} \\ 0, & \text{otherwise} \end{cases} \tag{2.1}$$

where $n \in \{1, 2\}$. In the flat sky, the shear field is described as,

$$\gamma_\pm(\boldsymbol{\theta}) = \gamma_1(\boldsymbol{\theta}) \pm i\gamma_2(\boldsymbol{\theta}) \,, \tag{2.2}$$

which in Fourier space is given by

$$\gamma_\pm(\boldsymbol{\ell}) = \gamma_1(\boldsymbol{\ell}) \pm i\gamma_2(\boldsymbol{\ell}) \,, \tag{2.3}$$

where $\gamma_{1,2}(\boldsymbol{\ell})$ are the Fourier transforms of $\gamma_{1,2}(\boldsymbol{\theta})$ respectively. The two components of shear are related to the convergence, $\kappa_\pm$, since both are functions of the lensing potential $\psi_\pm$,

$$\kappa_+ = \partial^* \partial^* \partial^{-2} \gamma_+ \quad , \quad \kappa_- = \partial \partial \partial^{-2} \gamma_- \,, \tag{2.4}$$

where

$$\partial \equiv \partial_1 + i\partial_2 \quad , \quad \partial^* \equiv \partial_1 - i\partial_2 \;\; \textit{and} \;\; \partial^2 \equiv \partial \partial^* \,, \tag{2.5}$$

$\partial_{1,2}$ are partial derivatives with respect to $\theta_1, \theta_2$, and the inverse Laplacian operator is given by

$$\partial^{-2} = \int \frac{\mathrm{d}^2\theta}{2\pi} \ln |\boldsymbol{\theta} - \boldsymbol{\theta}'| \,. \tag{2.6}$$

In Fourier space, the GWL convergence can be decomposed into the Fourier transforms of its E-mode and B-mode components, $\kappa_{E,B}(\boldsymbol{\theta})$, as

$$\kappa_\pm(\boldsymbol{\ell}) = \kappa_E(\boldsymbol{\ell}) \pm i\kappa_B(\boldsymbol{\ell}) \,. \tag{2.7}$$

These take the standard definition where the E-mode field is curl-free and the B-mode field is divergence-free; originally introduced for CMB polarisation analyses (Zaldarriaga & Seljak, 1997). Qualitatively this corresponds to galaxy images aligning tangentially around overdensities due to lensing, which produces an E-mode signal but no B-mode, thus we expect it to be zero. We show the relationship between the convergence and shear fields since the theoretical expression for the power spectrum is given in terms of the convergence E and B fields. In Fourier space the relationship between GWL convergence and shear is much simpler, since the Fourier counterparts of the partial derivatives are given by

$$\mathrm{FT}[\partial] = i\hat{\ell} \;\;,\;\; \mathrm{FT}[\partial^*] = i\hat{\ell}^* \,, \tag{2.8}$$

and

$$\hat{\ell} = \ell_x + i\ell_y \;\;,\;\; \hat{\ell}^* = \ell_x - i\ell_y \,, \tag{2.9}$$

such that in Fourier space

$$\kappa_+(\boldsymbol{\ell}) = \hat{\ell}^*\hat{\ell}^*|\hat{\ell}|^{-2}\gamma_+(\boldsymbol{\ell}) \;\;,\;\; \kappa_-(\boldsymbol{\ell}) = \hat{\ell}\hat{\ell}|\hat{\ell}|^{-2}\gamma_-(\boldsymbol{\ell}) \,. \tag{2.10}$$

These equations above can be simplified by replacing $\hat{\ell}$ with

$$\hat{\ell} = \ell e^{-i\varphi_\ell} \;\;,\;\; \ell = |\hat{\ell}| \,, \tag{2.11}$$

where $\varphi_\ell$ is the polar angle of both $\boldsymbol{\ell}$ and $\hat{\ell}$, which gives

$$\kappa_\pm(\boldsymbol{\ell}) = e^{\mp 2i\varphi_\ell}\gamma_\pm(\boldsymbol{\ell}) \,. \tag{2.12}$$

In practice, the shear field, described by $[\gamma_1, \gamma_2]$, is not sampled uniformly across the sky. Instead, we use galaxies as tracers and some parts of the sky contain fewer galaxies or are completely masked due to the effects described in the previous section. We therefore consider a binary mask, $W(\boldsymbol{\theta})$, where a pixel takes the value of 0 if it contains no galaxies and 1 if it contains 1 or more galaxies. This mask multiplies the two-components of shear in real-space as

$$\widetilde{\gamma}_{1,2}(\boldsymbol{\theta}) = W(\boldsymbol{\theta})\gamma_{1,2}(\boldsymbol{\theta})\,, \tag{2.13}$$

which is a convolution in Fourier space

$$\widetilde{\gamma}_{\pm}(\boldsymbol{\ell}) = \int \frac{d^2\ell'}{(2\pi)^2} W(\boldsymbol{\ell}-\boldsymbol{\ell'})\gamma_{\pm}(\boldsymbol{\ell'})\,. \tag{2.14}$$

Using the relationship between $\gamma_{\pm}$ and $\kappa_{\pm}$, we get the following equation for the masked convergence in Fourier space,

$$\widetilde{\kappa}_{\pm}(\boldsymbol{\ell}) = \int \frac{d^2\ell'}{(2\pi)^2} W(\boldsymbol{\ell}-\boldsymbol{\ell'})\kappa_{\pm}(\boldsymbol{\ell'})e^{\mp 2i\varphi_{\ell\ell'}}\,, \tag{2.15}$$

where $\varphi_{\ell\ell'} = \varphi_{\ell} - \varphi_{\ell'}$. To get a relationship between the masked and unmasked E and B components of convergence we add and subtract the above expressions for $\kappa_{\pm}(\boldsymbol{\ell})$ to get,

$$\widetilde{\kappa}_{E}(\boldsymbol{\ell}) = \int \frac{d^2\ell'}{(2\pi)^2}[\kappa_E(\boldsymbol{\ell'})\cos 2\varphi_{\ell\ell'} + \kappa_B(\boldsymbol{\ell'})\sin 2\varphi_{\ell\ell'}] \tag{2.16}$$

$$\widetilde{\kappa}_{B}(\boldsymbol{\ell}) = \int \frac{d^2\ell'}{(2\pi)^2}[-\kappa_E(\boldsymbol{\ell'})\sin 2\varphi_{\ell\ell'} + \kappa_B(\boldsymbol{\ell'})\cos 2\varphi_{\ell\ell'}]\,. \tag{2.17}$$

These equations show that in Fourier space, masking the data leads to the mixing of E and B-mode components. These masking effects must be accounted for if an estimator is to produced unbiased results. This is discussed in section 2.2.2.

The pseudo-$C_\ell$ code, NaMaster, used in this work was built to analyse CMB data sets, which consist of a temperature (scalar field) and polarisation (spin-2 field) measurements. From equation 2.12, the E and B-modes of convergence can be written in terms of the two components of the shear field $[\gamma_1, \gamma_2]$, i.e. for flat-sky:

$$\kappa_E(\boldsymbol{\ell}) \equiv \gamma_E(\boldsymbol{\ell}) = \gamma_1(\boldsymbol{\ell}) \cos 2\varphi + \gamma_2(\boldsymbol{\ell}) \sin 2\varphi \tag{2.18}$$

$$\kappa_B(\boldsymbol{\ell}) \equiv \gamma_B(\boldsymbol{\ell}) = -\gamma_1(\boldsymbol{\ell}) \sin 2\varphi + \gamma_2(\boldsymbol{\ell}) \sin 2\varphi\,. \tag{2.19}$$

Hence, in the context of GWL analyses, $\{\gamma_1, \gamma_2\}$ are analogous to the Stokes parameters $\{Q, U\}$ (Zaldarriaga & Seljak, 1997). Although mathematically equivalent, we distinguish between $\kappa_E$ and $\gamma_E$. Using $\kappa_E$ corresponds to reconstructing the convergence field from shear first – this requires inverse Fourier transforming into real-space before then measuring the cross-correlation and throwing away the B-mode information. Alternatively, $\gamma_E$ corresponds to using $[\gamma_1, \gamma_2]$ directly in the cross-correlation measurement.

### 2.2.2 The Pseudo-Power Spectrum Estimator

In this chapter we are interested in the cross-correlation between the convergence measured from CMB lensing which we will refer to as $\kappa_C$, and the shear field from GWL which we will refer to as $[\gamma_E, \gamma_B]$. The cross-correlation power spectrum, $C(l)^{\kappa_C \gamma_E}$, is defined as the normalised angular average, given by

$$\langle |\kappa_C(\boldsymbol{\ell}) \gamma_E^*(\boldsymbol{\ell})| \rangle = (2\pi)^2 \delta_D(\boldsymbol{\ell} - \boldsymbol{\ell}') C(l)^{\kappa_C \gamma_E}\,, \tag{2.20}$$

such that the expected average $C(l)^{\kappa_C \gamma_E}$ is

$$\langle C(l)^{\kappa_C \gamma_E} \rangle = \frac{1}{A} \int_0^{2\pi} \frac{\mathrm{d}\varphi_l}{2\pi} \langle |\kappa_C(\boldsymbol{\ell}) \gamma_E^*(\boldsymbol{\ell})| \rangle\,, \tag{2.21}$$

where the integral is an averaging over a finite area, $A$ and the Dirac delta function is substituted for,

$$\delta_D(0) \approx \frac{A}{(2\pi)^2}\,. \tag{2.22}$$

The full Dirac delta function is recovered in the full-sky limit.

For the masked fields discussed above, we can only measure a pseudo-power spectrum, $\widetilde{C}^{\kappa_C\gamma_E}(\ell)$. This is given by the same equation, but the $\kappa_C$ and $\gamma_E$ fields are replaced by their corresponding masked fields to give

$$\begin{aligned}\langle\widetilde{C}^{\kappa_C\gamma_E}(\ell)\rangle =& \frac{1}{A}\int\frac{\mathrm{d}\varphi_\ell}{2\pi}\int\frac{\mathrm{d}^2\ell'}{(2\pi)^2}W_{\mathrm{CMB}}(\boldsymbol{\ell}-\boldsymbol{\ell'})\int\frac{\mathrm{d}^2\ell''}{(2\pi)^2}W^*_{\mathrm{GAL}}(\boldsymbol{\ell}-\boldsymbol{\ell''})\\ &\times\langle|\kappa_C(\boldsymbol{\ell'})\times[\gamma^*_E(\boldsymbol{\ell''})\cos2\varphi_{\ell\ell''}+\gamma^*_B(\boldsymbol{\ell''})\sin2\varphi_{\ell\ell''}]|\rangle\,.\end{aligned} \tag{2.23}$$

Here $W_{\mathrm{CMB}}$ corresponds to the CMB survey window and $W_{\mathrm{GAL}}$ can be either a binary mask or galaxy weight map, which is constructed by summing the weight associated with galaxies in each pixel. Using the definition for the power spectrum, the pseudo-power spectrum can be given in terms of the true power spectrum,

$$\begin{aligned}\langle\widetilde{C}^{\kappa_C\gamma_E}(\ell)\rangle =& \frac{1}{A}\int\frac{\mathrm{d}\varphi_\ell}{2\pi}\int\frac{\mathrm{d}^2\ell'}{(2\pi)^2}W_{\mathrm{CMB}}(\boldsymbol{\ell}-\boldsymbol{\ell'})W^*_{\mathrm{GAL}}(\boldsymbol{\ell}-\boldsymbol{\ell'})\\ &\times[C^{\kappa_C\gamma_E}(\ell')\cos2\varphi_{\ell\ell'}+C^{\kappa_C\gamma_B}(\ell')\sin2\varphi_{\ell\ell'}]\,,\end{aligned} \tag{2.24}$$

for the E-mode of the cross-correlation and a similar equation can be written for the cross-correlation with the GWL B-mode shear field. The power spectrum in the above equation only depends on $|\boldsymbol{\ell'}|$ and the masks and trigonometric functions only depends on the polar angles $\varphi_\ell$ and $\varphi_{\ell'}$. Thus the integral over $\varphi_\ell$ can be taken to be independent of cosmology. Thus the masking effect can be modelled using a mode mixing matrix, $\mathcal{M}_{\ell\ell'}$. This can be computed in terms of the Fourier coefficients of the mask,

$$\mathcal{M}(\ell,\ell') = \frac{1}{(2\pi)^2A}\int_0^\pi \mathrm{d}\nu W_{\kappa_C\gamma_E}(L(\ell,\ell',\nu))M_\nu(\nu)\,, \tag{2.25}$$

where $\nu$ is the angle between $\boldsymbol{\ell}$ and $\boldsymbol{\ell'}$, and $W_{\kappa_C\gamma_E}$ corresponds to the power spectrum of the mask,

$$W_{\kappa_C\gamma_E}(L) = \int_0^{2\pi} \frac{\mathrm{d}\varphi_\ell}{2\pi} W_{CMB}(\boldsymbol{L}) W^*_{\mathrm{GAL}}(\boldsymbol{L})\,, \tag{2.26}$$

and

$$L(\ell, \ell', \nu) = |\ell - \ell'| = \sqrt{\ell^2 + \ell'^2 - 2\ell\ell' \cos\nu}\,, \tag{2.27}$$

and finally

$$M = \begin{pmatrix} \cos 2\nu & -\sin 2\nu \\ \sin 2\nu & \cos 2\nu \end{pmatrix}. \tag{2.28}$$

In a realistic scenario, where the flat-sky pixels use a Cartesian coordinate system and have a finite size, coordinates $(\ell, \nu)$ cannot be easily used without losing significant accuracy. In practice, in NaMaster, these integrals are in two dimensions $(\ell_x, \ell_y)$ where the effect of binning into annuli of these Cartesian pixels is fully taken into account. From this we get the result,

$$\widetilde{\boldsymbol{C}}(\ell) = \int_0^\infty \mathrm{d}\ell' \ell' \mathcal{M}(\ell, \ell') \boldsymbol{C}(\ell')\,, \tag{2.29}$$

where

$$\boldsymbol{C} \equiv (C(\ell)^{\kappa_C\gamma_E}, C(\ell)^{\kappa_C\gamma_B})^T\,. \tag{2.30}$$

In reality we evaluate these integrals as discrete sums, so that the above equation is re-written as

$$\widetilde{C}(\ell_i) = \sum_j \Delta\ell_j \ell_j \mathcal{M}(\ell_i, \ell_j) C(\ell_j)\,, \tag{2.31}$$

where the value of $\ell_i$ is dependent on the size of the field in real-space and the choice of pixel size when binning the data. The approximation of integral to sum must also be applied when evaluating the mode coupling matrix and the masked power spectrum. A new mixing matrix can be defined as

$$M_{\ell_i \ell_j} = \Delta\ell_j \ell_j \mathcal{M}(\ell_i \ell_j)\,, \tag{2.32}$$

to give the following matrix relation

$$\widetilde{C}(\ell) = M_{\ell\ell'} C_{\ell'}\,, \tag{2.33}$$

where the $[i, j]$ sub-scripts have been dropped and replaced with $[\ell, \ell']$. By inverting the above equation we can recover the power spectrum,

$$C_\ell^{\mathrm{r}} = (M^{-1})_{\ell\ell'} \widetilde{C}_{\ell'}\,. \tag{2.34}$$

Since information is lost across the field due to masking, it is in general not possible to invert the mode coupling matrix, defined above, directly. A solution to this involves binning the coupled pseudo-power spectrum in a set of bandpowers,

$$C_b^{\mathrm{r}} = (M_b)^{-1} \widetilde{C}_b^{\mathrm{obs}} \tag{2.35}$$

where the subscript $b$ corresponds to a given bandpower. This assumes that the true power spectrum is a stepwise function which takes constant values over the multipoles contributing to each band power. In general, this is not the case and so the theoretical power spectrum, $C_\ell^t$, must have a bandpower binning correction applied to it, so that it can be compared to the measured spectrum in a consistent way. Mathematically, the process is described as

$$C_b^t = (M_b)^{-1} \widetilde{C}_b^t = (M_b)^{-1} B\{M C_\ell^t\}\,, \tag{2.36}$$

where $B$ is the binning matrix. This method is the most computationally efficient way to compare the pseudo-power spectra to a cosmological model.

An analogous description can be presented for the curved sky case. A Spherical Harmonic Transform can be applied to a given field $a(\boldsymbol{\theta})$ rather than a Fourier Transform, to measure the spherical harmonic coefficients, $a_{\ell m}$ from which the power spectrum can estimated. We refer to Alonso et al. (2019) in which this is fully derived.

### 2.2.3 Theoretical Power Spectrum

The predicted 2D power spectrum, introduced in equation 2.36, can be related to the 3D matter power spectrum, under the Limber approximation[3], which is given by:

$$C_\ell^{ij} = \int_0^{\chi_H} d\chi \frac{W_i(\chi)W_j(\chi)}{f_k(\chi)^2} P(k, \chi), \tag{2.37}$$

where $i$ and $j$ denote $\kappa_C$ and $\gamma_E$, $W_i(\chi)$ is a window function, $\chi$ is the comoving distance, $f_k(\chi)$ is the angular diameter distance and $P(k, \chi)$ is the 3D matter power spectrum at a given comoving distance. Although in cosmology we aim to measure the 3D matter power spectrum, this is complicated by our observational limitations. In practice, we observe a wedge of Universe and thus instead of being able to calculate $P(k, \chi)$, we calculate the average value over this region. The area of sky observed increases for increasing distances, which can be accounted for by including a factor of the inverse of the distance squared, $f_k(\chi)^2$. The general form for the window function for lensing is

$$W_i(\chi) = \frac{3\Omega_m H_0^2}{2c^2} \frac{f_k(\chi)}{a(\chi)} \int_\chi^{\chi_H} d\chi' p_i(\chi') \frac{f_k(\chi' - \chi)}{f_k(\chi')} , \tag{2.38}$$

where $p(\chi)$ is the probability distribution function. For CMB lensing, this is given by

$$p_{\mathrm{CMB}}(\chi) = \delta(\chi - \chi^*) , \tag{2.39}$$

[3]In the Limber approximation, effectively spherical bessel functions are replaced with a delta function. This approximation has been shown to hold at $\ell > 10$ and makes the power spectrum easier to compute.

since the CMB is on a single source plane and $\chi^*$ is the comoving distance to the surface of last scattering. For GWL, this is given by

$$p_{\mathrm{GAL}}(\chi) = n(z)\frac{dz}{d\chi}\,, \tag{2.40}$$

and $n(z)$ is the number of galaxies as a function of redshift. The window functions determine at which redshifts structure in the Universe contributes to the cross-correlation power spectrum. The overlap of the GWL and CMB lensing window functions, weighted by the matter power spectrum, determines the degree of cross-correlation between the two data sets. Thus the cross–correlation power spectrum, defined in equation 2.37, is sensitive to structure at intermediate redshifts. It is the fact that these two window functions overlap that means we can measure the cross–correlation.

### 2.2.4 Estimating Errors

We estimate the error associated with a cross-correlation measurement analytically using the Knox equation

$$\sigma^2(\hat{C}_l^{\kappa_C\gamma_E}) = \frac{1}{(2\ell+1)f_{\mathrm{sky}}\Delta\ell}[(C_\ell^{\kappa_C\kappa_C} + N_\ell^{\kappa_C\kappa_C})(C_\ell^{\gamma_E\gamma_E} + N_\ell^{\gamma_E\gamma_E}) + (C_\ell^{\kappa_C\gamma_E})^2]\,, \tag{2.41}$$

which uses theoretical models of the auto and cross-spectra of the CMB lensing convergence and GWL shear fields, given by equation 2.37. Only the noise spectra from the auto-correlations are required — accounting for the contributions from cosmic variance and the noise in the both lensing maps — since the noise in the two fields should not be correlated with each other. The factor of $(2\ell + 1)$ accounts for the number of modes and $f_{\mathrm{sky}}$ accounts for the partial sky coverage and any loss of modes due to apodisation. Equation 2.41 does not account for the mode coupling introduced by partial sky coverage which would produce larger errors in the case of complicated

GWL masks (García-García et al., 2019).

The CMB lensing noise is estimated from CMB lensing maps, which in turn can be derived from the noise properties of the CMB intensity and polarisation maps. In the case of this project we measure the CMB lensing auto-power spectrum from ACT CMB lensing maps and subtract a theoretical auto spectrum computed for a fiducial cosmology. The GWL noise is estimated as

$$N_\ell^{\gamma_E\gamma_E} = \frac{\sigma_e^2}{n_{\mathrm{eff}}}\,, \tag{2.42}$$

where $\sigma_e$ is the variance on the galaxy ellipticity and $n_{\mathrm{eff}}$ is the effective number of galaxies per square arcminute using the Chang et al. (2013) definition. The noise components and corresponding theoretical auto and cross spectra are shown in Fig. 2.1, for the example of ACT CMB lensing data, and KiDS GWL, described in the next section. We can use equation 2.42 to predict the expected signal-to-noise of a cross-correlation measurement as

$$\frac{S}{N} = \sqrt{\sum_\ell \left(\frac{C_l^{\kappa_C\gamma_E}}{\sigma(\hat{C}_l^{\kappa_C\gamma_E})}\right)^2}\,. \tag{2.43}$$

A more accurate way to capture the noise in the cross-correlation measurement is to use simulations, which contain the noise representative of the data.

## 2.3 Simulations and Data

The goal of this work is to develop the tools required to perform a measurement of the cross-correlation power spectrum between any future CMB lensing and GWL data. This pipeline can then be applied to current data sets including ACT CMB lensing correlated with KiDS, DES or HSC GWL, and will be appropriate for future data with SO CMB lensing and LSST GWL(Ade et al., 2019; Ivezić et al., 2019). In the

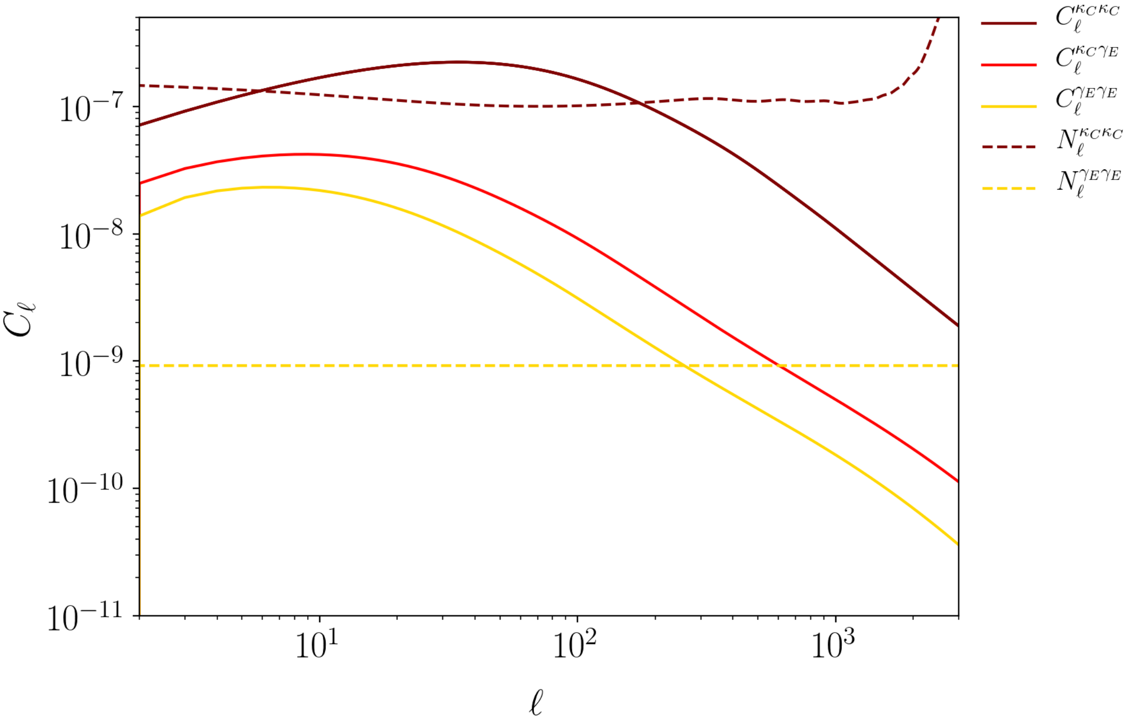


Figure 2.1: Theoretical values for the auto and cross-power spectra, and their corresponding noise spectra which all contribute to the cross-correlation noise as given by equation 2.41. Here the CMB lensing noise is the real noise spectrum for ACTPol S13-15 and GWL noise is estimated for the K-1000 data set from equation 2.42. It can be seen that the biggest contribution is from CMB lensing noise.

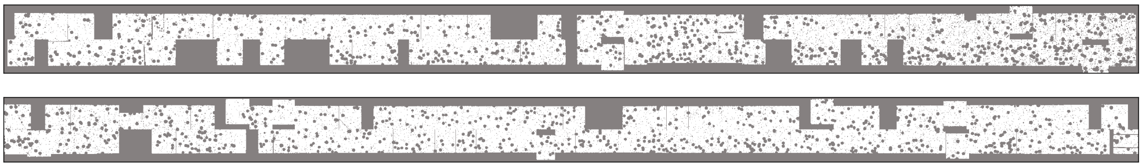

Figure 2.2: This is the area used in the ACT×CS82 analysis, with the CS82 mask shown in white. The two maps correspond to the map being split into two regions either side of zero in right ascension. The overlapping region of ACT and CS82 has an area of 129.2 deg$^2$ after the CS82 mask has been applied.

short-term, we will use it in chapter 3 to cross-correlate the latest KiDS GWL data set, K-1000, with ACT CMB lensing, and thus we create simulations which reflect the properties of these surveys. We also confirm that our new pipeline can reproduce existing results.

### 2.3.1 CS82×ACT data

We use the maps from the first CMB lensing/GWL cross-correlation (Hand et al., 2015) to test our pipeline. A detailed explanation of the data sets can be found in the original paper which we summarise here. The CMB lensing data comes from the ACT observations made of Stripe-82 from 2008-2010, using the 148 GHz frequency channel. The ACT data is centred on the celestial equator and extends 108 degrees in right ascension and 3 degrees in declination. The convergence was reconstructed using the minimum variance quadratic estimator described in Das et al. (2011) from CMB temperature maps. GWL data came from the Canada-France-Hawaii Telescope Stripe 82 Survey (CS82). This was an $i$-band survey designed for GWL measurements, covering an area of 160 deg$^2$ (129.2 deg$^2$ post-masking) on the celestial equator, shown in Fig. 2.2. The measured source galaxy number density is 15.8 galaxies arcmin$^{-2}$. Both CMB lensing and GWL maps have a resolution of 1 arcminute. The redshift distribution for CS82 galaxies was estimated from the 30-band COSMOS photometric redshift catalogue (Ilbert et al., 2009). The functional form of the weighted redshift distribution from (Fu et al., 2008) is well approximated by

$$\frac{dn}{dz} = A\frac{z^a + z^{ab}}{z^b + c} \,, \tag{2.44}$$

with $a = 0.531$, $b = 7.810$, $c = 0.517$, and $A = 0.688$. Uncertainties in this redshift distribution are due to the sample variance in the COSMOS data, the uncertainties in the photometric redshift for COSMOS and the assumed form of $dn/dz$. The Hand et al. (2015) analysis used a combined mask, i.e., only the exact overlapping area was used, so the patchy CS82 mask was applied to the ACT data. Due to limitations in the LensCross pipeline, the maps were split into two regions either side of zero in right ascension. A Gaussian apodisation was applied to the outer edge of the mask. The convergence was reconstructed from the two shear maps, using a standard Kaiser-Squires (Kaiser & Squires, 1993) approach as described and used in the (Hand et al., 2015) analysis. The cross-correlation measurement was then made starting from GWL lensing convergence in real-space. The cross-correlation was measured for the two sets of maps and then the average of the two cross-spectra was taken. No galaxy weights were applied during the measurement. Finally, the errors were estimated from uncorrelated simulations. In our analysis we take the same CMB lensing convergence, GWL shear and GWL mask as our input maps. We use these data sets to check the consistency of the Hand et al. (2015) result with our new cross-correlation pipeline based on the NaMaster pseudo-$C_\ell$ code.

### 2.3.2 Simulations

We create a simple set of simulations on which to test a variety of analysis choices. Theoretical CMB lensing and GWL auto and cross-power spectra are computed using the Core Cosmology Library from the LSST DESC project (Chisari et al., 2019)[4].

[4]https://github.com/LSSTDESC/CCL

This uses the code CLASS (Lesgourgues, 2011) to calculate the matter power spectrum at many redshifts which are then used to evaluate equation 2.37. Since the aim of the study is to eventually apply it to KiDS and ACT data, we use the real KiDS redshift distribution in equation 2.38. This is estimated using the methods described in Hildebrandt et al. (2018) for a single redshift bin from 0.1 to 1.2. We generate Gaussian random field realisations from these spectra for $[\kappa_c(\boldsymbol{\theta}), \gamma_1(\boldsymbol{\theta}), \gamma_2(\boldsymbol{\theta})]$. These simulations contain super-sample covariance, which is the sampling error caused by coupling to modes that are larger than the survey scale. To make these simulations as realistic as possible, we sample the shear maps at the location of the KiDS galaxies to produce a galaxy catalogue in the form of real KiDS data. Noise is then added by randomly sampling a Gaussian centred on zero with a width $\sigma_i = \frac{1}{\sqrt{w_i}}$, where $w_i$ is the weight associated with a KiDS galaxy which comes from the shape measurement process (Miller et al., 2013). Although this is not exactly what the galaxy weights correspond to, it should only lead to a slight over estimation of the noise[5]. The KiDS galaxy ellipticity distribution can be approximately described by a Gaussian centered on zero with $\sigma_e = 0.28$ – we check that this form is reproduced by the simulated galaxy ellipticities. Maps of the shear field are then made from this galaxy catalogue, such that the maps are masked in exactly the same way as the KiDS data. We use the real noise curves from ACTPol, appropriate for the data taken in 2013-15 and described in detail in Chapter 4, to add noise to the simulated CMB lensing convergence map and also apply the ACT sky window. We create these maps with half arcminute resolution to match the ACT flat-sky maps and the real number of galaxies per pixel.

We can also use these simulations to estimate the error bars. By measuring the cross-correlation for a suite of 100 simulations we can then take the sample variance of the resulting power spectrum. We check that these errors are comparable to the predicted variance from equation 2.42 using $\sigma_e = 0.28$, $n_{\text{eff}} = 7.2$ (Chang et al., 2013)

[5] Another valid option would be to add a randomly rotated version of a given galaxy to that galaxy's ellipticity

and common masked sky area of 275 deg$^2$. Estimating the errors by this method will more accurately capture the impact of choices in our method on the signal-to-noise.

## 2.4 Results

### 2.4.1 Reproducing Hand et al. (2015)

We check that our new pipeline can reproduce the CS82$\times$ACT result, using the same analysis choices as in Hand et al. (2015). This corresponds to reconstructing GWL convergence from smoothed shear maps, applying the same binary GWL mask – which has been apodised on the outer edge – to both convergence maps. The result is shown in Fig. 2.3, with the E-mode measurement on top and the B-mode component in the lower panel. The B-mode in this case is estimated by switching $\gamma_1 \to \gamma_2$ and $\gamma_2 \to -\gamma_1$, which is equivalent to a 45 degree rotation of the galaxies.

We then consider more optimal choices in our pipeline. In this case we do not use a combined mask and use the galaxy weights instead of a binary mask for the GWL shear fields and no mask for the CMB lensing field, since both data sets cover the same area of sky by design. We also measure the cross-correlation directly with the shear maps rather than converting to convergence first. Figure 2.4 shows the new result, with the B-mode null test being produced as a by-product of computing spectra for a $\{T, Q, U\} \to \{\kappa_C, \gamma_1, \gamma_2\}$ analysis.

It is clear that in both cases the published result is recovered with the NaMaster pipeline closely. The errorbars in both cases discussed above come from the Hand et al. (2015) result as we do not have access to the simulations used in the original analysis. Most of the changes we make in the second case either produce a quicker measurement pipeline or lead to a reduction in the errorbars which cannot be seen here, however none of these changes significantly alter the cross-spectra measured.

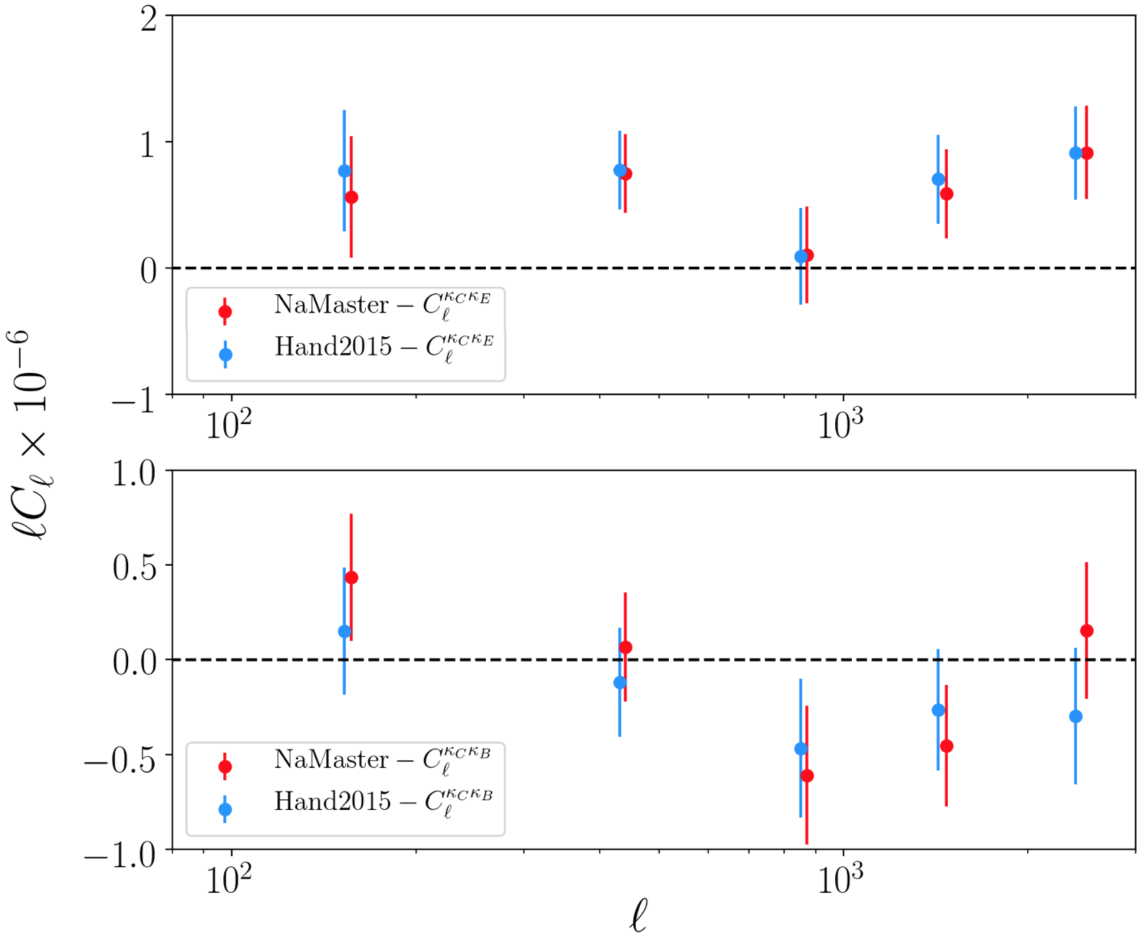


Figure 2.3: Comparison of the CS82×ACT cross-spectrum from the published Hand et al. (2015) analysis, and our new pipeline. Here we use NaMaster with settings equivalent to the Hand et al. (2015) analysis.

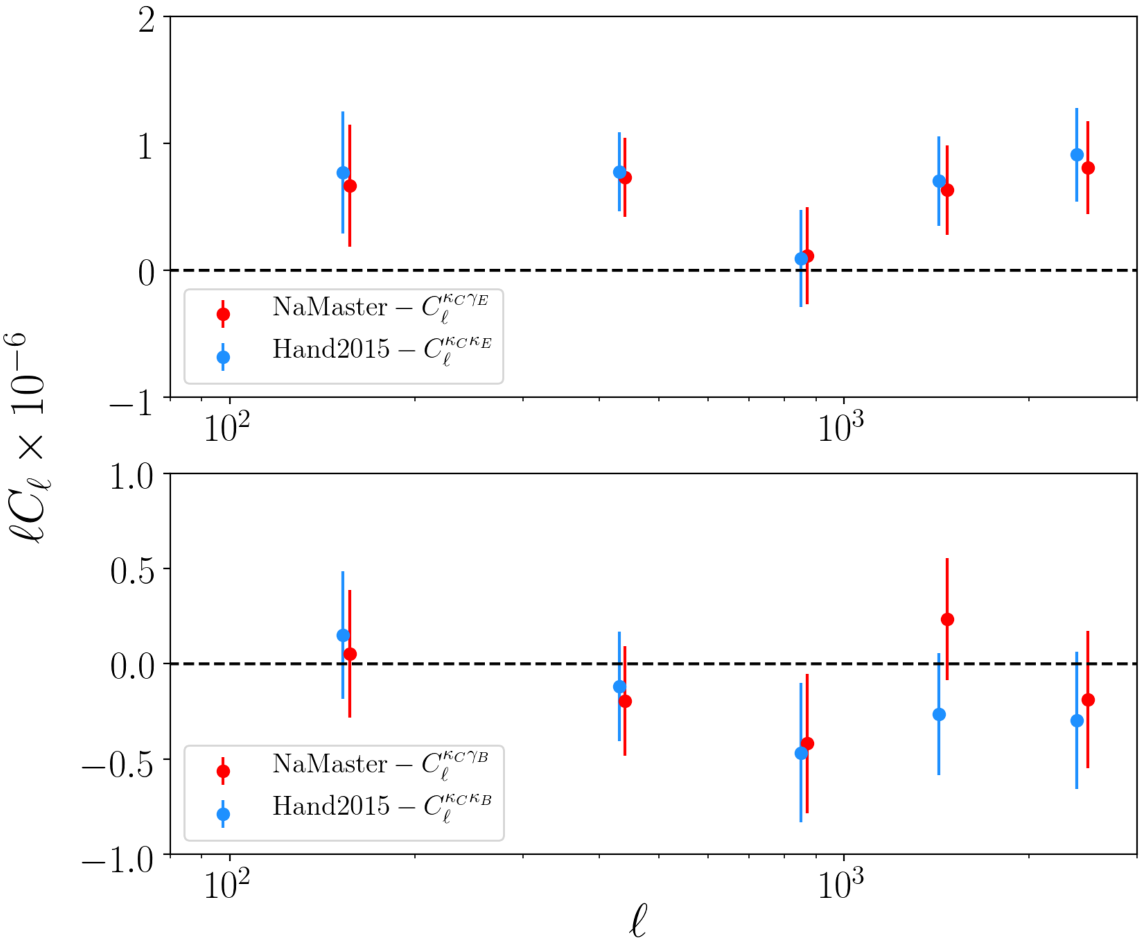


Figure 2.4: As in Fig 2.3, but modifying our new pipeline to use the two components of shear directly, and using galaxy weights and separate masks for the ACT and CS82 data.

### 2.4.2 Simulation Tests

Given this good agreement, we next apply our pipeline to the simulations appropriate for the correlation between KiDS×ACTPol. The baseline result is shown in Figure 2.5 for E and B-modes. The simulated $C_\ell^{\kappa_C \gamma_E}$ signal is recovered as expected, with a $8\sigma$ detection of the cross-correlation. The $C_\ell^{\kappa_C \gamma_B}$ is consistent with null, as expected.

In the following, we investigate the impact of various analysis choices on the recovered signal. In each case we plot the recovered pseudo-power spectrum from a single simulation. The corresponding error bars are then estimated as the variance of the power spectrum measured for all 100 simulations.

#### 2.4.2.1 Convergence vs. Shear

The first CMB lensing×GWL measurements were made with GWL convergence maps, which involves performing a reconstruction from the spin-2 shear field as described in section 2.2. The alternative is to measure the cross-correlation from the two components of shear directly. Using GWL convergence, rather than shear, was initially favoured, since the first pseudo-power spectrum codes were written for measuring the power spectrum of temperature maps (spin-0) and not polarisation (spin-2 fields). However, since there is both an E and B mode component of convergence and this method only includes the E mode, not all of the information is being used in the cross-correlation measurement. Also, performing a convergence reconstruction is somewhat cumbersome, as it requires transforming into Fourier space and then back into real-space only to apply the transformation once again for the purpose of power spectrum estimation. By estimating cross-spectra from the shear fields directly avoids systematic biases and minimises errors introduced during convergence reconstruction (Van Waerbeke et al., 2013). This motivates using the NaMaster code in our pipeline as it has the flexibility to use spin-2 fields as well as spin-0 fields. We use simulations to test this and find that both methods give consistent results, agreeing within $0.7\sigma$, for

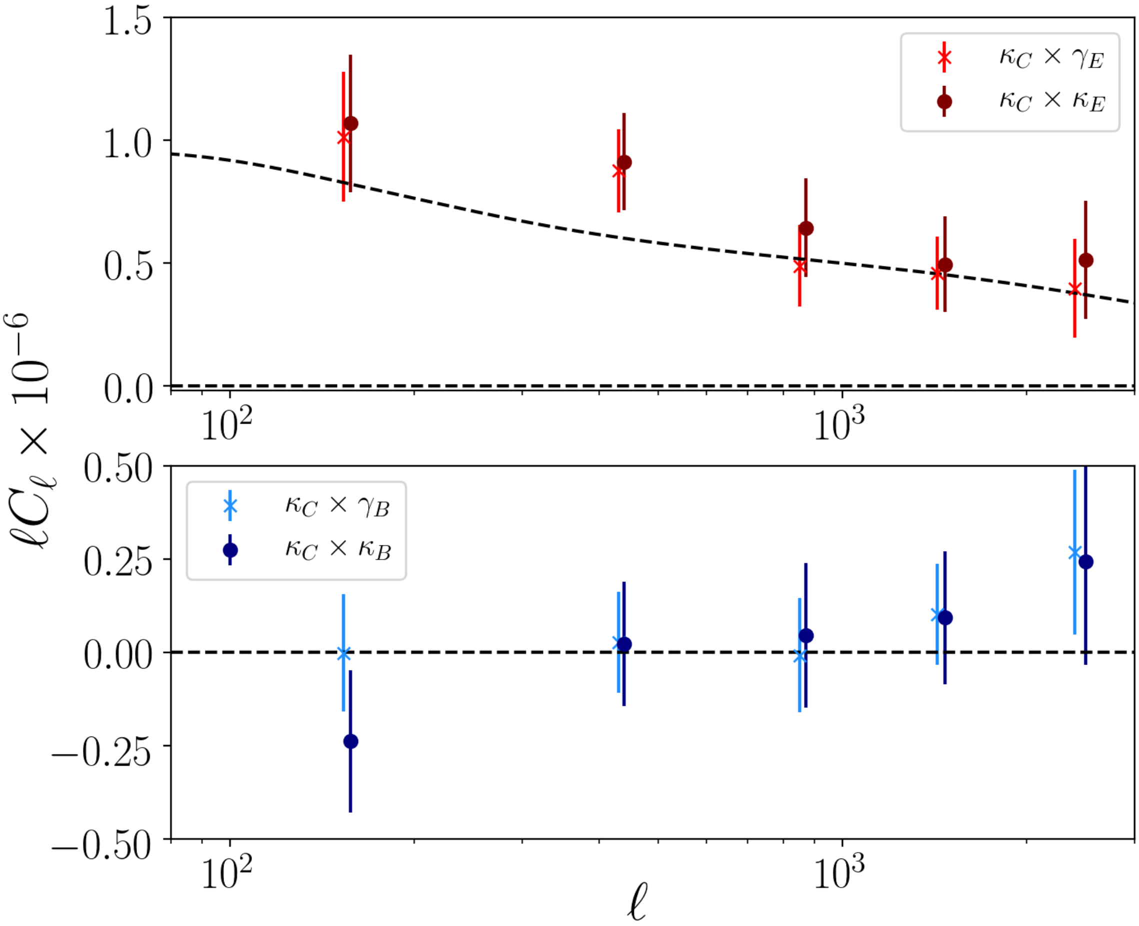


Figure 2.5: Comparison of cross-correlating with a GWL convergence map or with the GWL shear maps directly. These two measurements are consistent with each other.

a single simulation, as shown in Fig. 2.5.

#### 2.4.2.2 Flat Sky vs. Curved Sky

For current data sets flat-sky approximations have been appropriate. However as we move into the LSST and SO era of cosmological surveys, this will no longer be the case, as the coverage will approach half the sky. It is essential that these curved sky codes are quick enough to deal with these larger data sets.

NaMaster is unique in its flexibility to measure power spectra on both the flat and curved sky, and not requiring a HEALPix map for a curved sky analysis. Currently for ACTPol, maps are produced using a Plate Carree pixelisation – this is a special case of equirectangular projection, which means that the pixels are rectangular and will have a varying area – and reprojecting into HEALPix can introduce errors into the maps.

In the case of NaMaster, calculating the mode coupling matrix is faster using the curved sky code for an ACT×KiDS size analysis – the time taken to calculate the mode coupling matrix for flat sky goes like $\ell_{\max}^4$ compared to $\ell_{\max}^3$ for curved sky, since we cannot use the azimuthal symmetry due to the cartesian pixelisation. However the next stage of measuring the coupled power spectra is slower for calculating on the curved sky as Spherical Harmonic Transformations go like $N_{\rm pix}^{3/2}$ in contrast to $N_{\rm pix} \times \log N_{\rm pix}$ for Fast Fourier Transforms used in flat sky. Thus there is a trade off which depends on the size and number of pixels in a given data set and the number of simulations required to calculate the covariance matrix.

We compute the spectra using both the flat and curved-sky approach. For both cases we make pixelised shear maps directly from the simulated catalogues. Both approaches give binned power spectra that agree to within a standard deviation, for a single simulation, as shown in Fig. 2.6.

#### 2.4.2.3 Apodisation

As previously discussed, binary masks lead to complications in Fourier space. One method which has been used to mitigate this effect is apodisation. Apodisation is the smoothing of mask edges, such that the mask gradually transitions between zero and one between a masked and an unmasked region. When applying apodisation, the information present in the edges of the map is lost. This in turn suppresses the amplitude of the measured power spectrum and therefore must be corrected for. Apodisation is widely used in CMB experiments that have simple masks – this is mostly because the temperature auto-spectrum is quite steep. However, since GWL

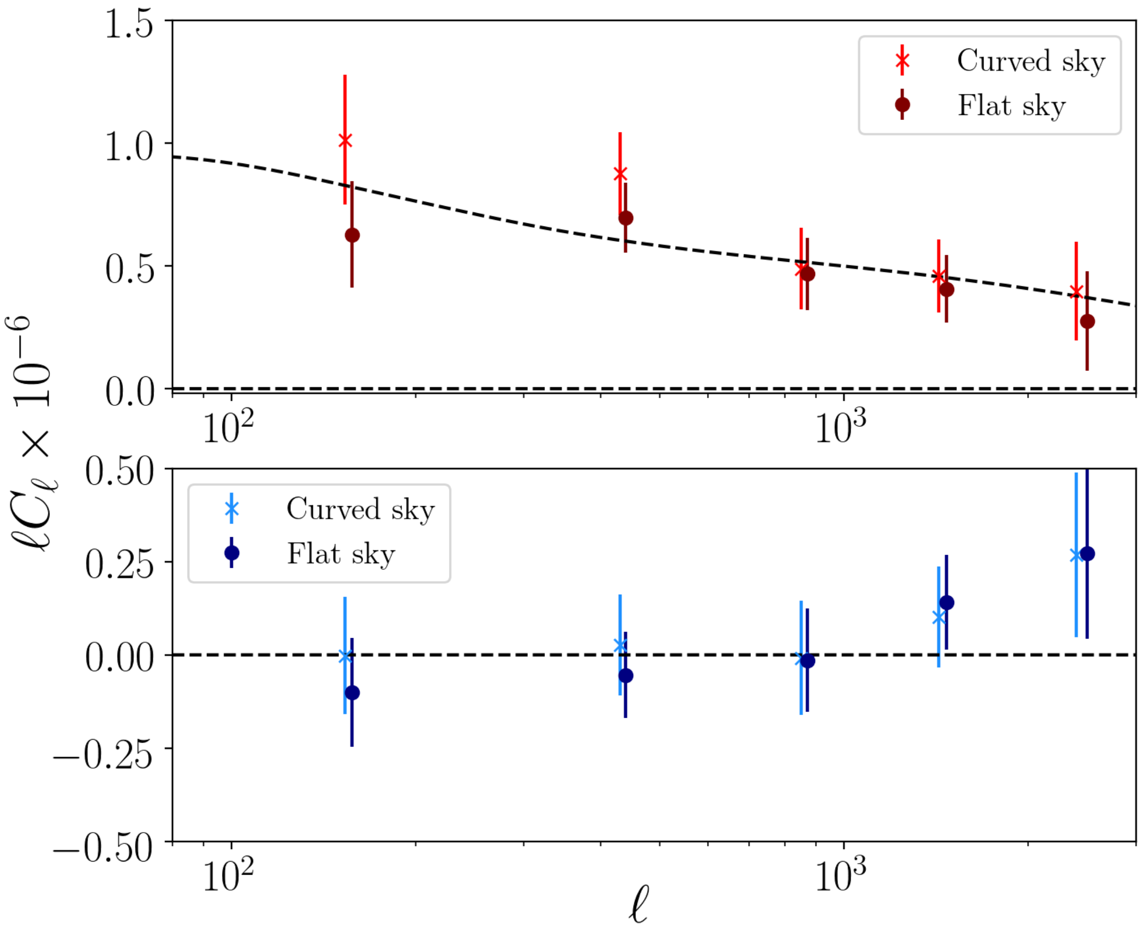


Figure 2.6: Flat sky and curved sky codes give consistent results for current data sets.

shear maps contain many small holes within a large cut-sky mask, even a small level of apodisation can lead to a large reduction in area and loss of information as shown in Fig. 2.7.

In this section we consider different levels of apodisation applied to a binary mask, using the following procedure of Alonso et al. (2019) — all pixels inside a radius of $2.5\theta_A$ of a masked pixel are set to zero, the mask is then smoothed with a Gaussian window function with $\sigma = \theta_A$, finally pixels which were zero in the original mask are set to zero to confirm that masked pixels are still masked. The different apodisation scales, $\theta_A$, are $[0, 0.25', 0.375', 0.5']$. The effect of these different levels of apodisation are shown in Fig. 2.7. This loss of area increases the noise in the measurement as expected from equation 2.41. Figure 2.8 shows that increasing levels of apodisation raises the noise in each measurement, particular in the second bin which is at the scale of the holes in the GWL mask. Therefore in this case, apodisation is not required or beneficial.

#### 2.4.2.4 Zero-padding

Considering the most recent data sets, CMB experiments observe larger patches of sky than the GWL surveys. One possibility is to cut the maps down to the area which they have in common, creating a combined mask. However, this does not optimally use all the information available in the maps. The convergence in one pixel will be correlated with pixels outside of the map because the correlation length is greater than zero and predicted to be at least 1 degree. Therefore, using a combined mask means information is being wasted, particular if the holes in the GWL mask are applied to the CMB lensing map. A better solution is to have two different masks and zero-pad the smaller map to match the size of the larger maps. This requires an estimator that can include the two different masks and account for them fully in the mode coupling matrix. The main effect is an improvement on the noise of the

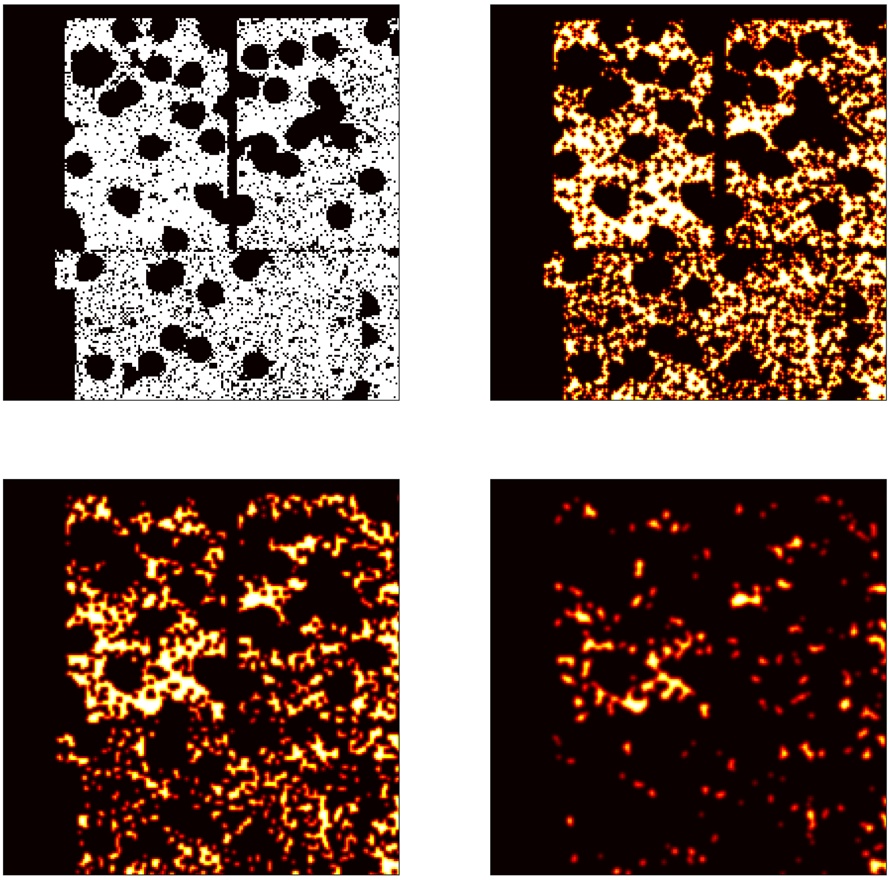

Figure 2.7: A small cut out of the GWL binary mask apodised with 3 different apodisation scales. The top-left panel has no apodisation applied and then the top-right, bottom-left and bottom-right panels have an apodisation scale of $\theta_A = 0.25', 0.375', 0.50'$ applied respectively. The largest apodisation scale corresponds to the size of one pixel in this map. In can be seen that for a GWL mask with many holes in the mask, the area of the mask is reduced significantly when apodised.

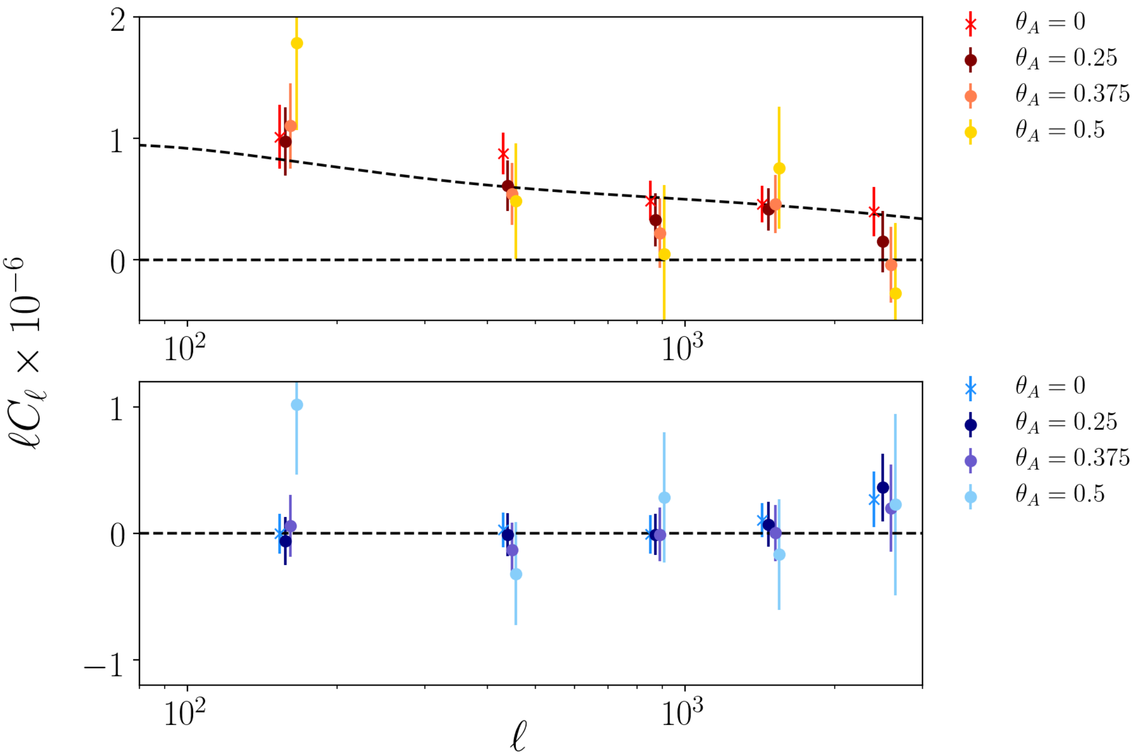


Figure 2.8: Comparing a binary mask with three different levels of apodisation applied. Increasing apodisation reduces the area used and therefore increases the noise. This is particularly notable in the second bin which is at the scale of the size of the holes in the GWL mask.

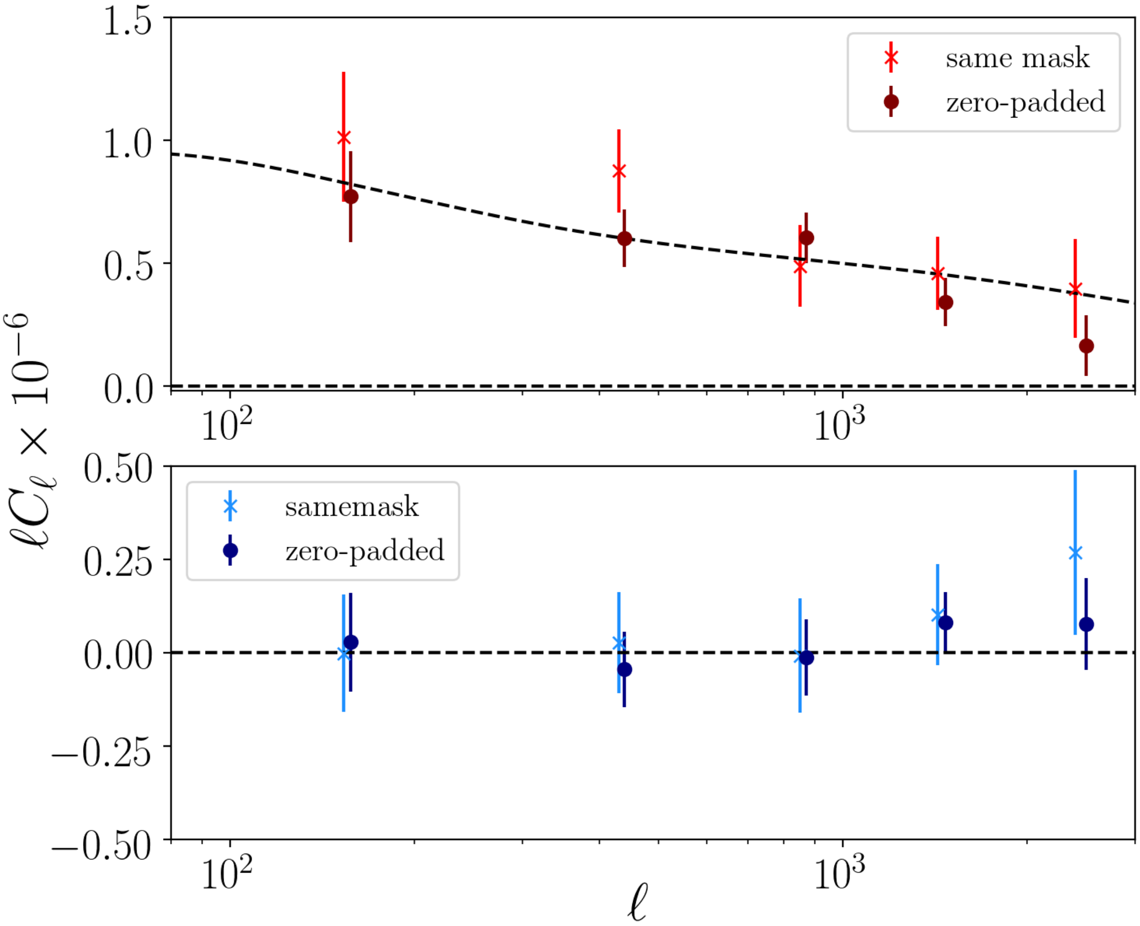


Figure 2.9: Comparison of the smaller GWL binary mask applied to both data sets and using two different maps zeropadding the GWL mask to match the CMB lensing mask.

measurement, which can be seen in Fig. 2.9. The error bars reduce in size by up to a factor of 1.6.

#### 2.4.2.5 Masking vs. Galaxy Weight Map

When measuring the pseudo-power spectrum, the data is analysed in a pixelated map form since Fast Fourier/Spherical Harmonic Transforms (for flat/curved-sky) can be used, and this significantly speeds up computation. However, making these maps depends on the distribution of source galaxies, which is not uniform. Maps of the shear field are created from galaxy catalogues by taking the weighted average shear of the galaxies within a pixel. These are inverse variance weights which come from estimating the ellipticity of the galaxies (Miller et al., 2013).

A binary mask can then be created which has a value zero if no galaxies are in a given pixel and a value of one if the pixel contains one or more galaxies that have a valid ellipticity value. Using a binary mask and no weight information means that each pixel contributes the same even if it contains only a single galaxy or the shape noise in a given region is larger due to variation in seeing conditions for different sky pointings.

To account for this, using a weight map instead of a binary mask is more appropriate. A weight map can be created by summing the weights of the galaxies in a given pixel. This way the quality of the shape estimates can be included, and regions with poor shape measurements do not contribute to the measurement as much, which leads to reduction in the noise. Also, by using a weight map rather than a binary mask, the mask is effectively smoother and contains less significant features. In the Hand et al. (2015) analysis they found that by including the weights, power at large $\ell$ values was suppressed, which is counter-intuitive to what is expected. We do not find this to be the case with our new pipeline and the input theory power spectrum is correctly recovered, as shown in Fig. 2.10. It can also be seen that the error bars are smaller in the case where the weight mask is applied. The error bars reduce in size by up to a factor of 1.7.

## 2.5 Discussion

In this chapter we have presented a new pipeline for measuring the CMB lensing GWL cross-correlation power spectra, and explored a set of different analysis options. We have shown that our pipeline, based on the psuedo-$C_\ell$ NaMaster code, is robust to variations in these choices.

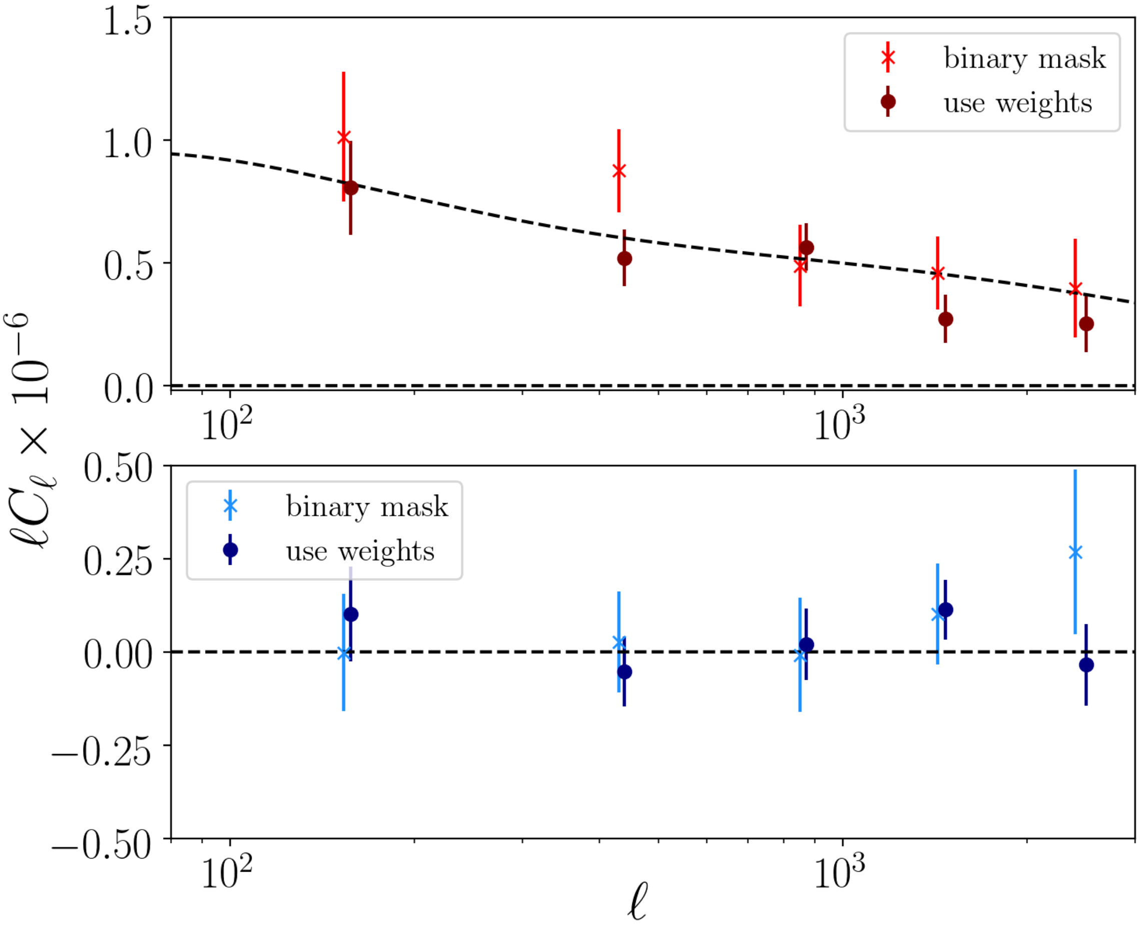


Figure 2.10: Instead of using a binary mask we use a 'weight map' which is the sum of the galaxy weights in each pixel. These two methods give consistent power spectra, with the weights producing a reduction in the noise as expected.

We have also highlighted that for analyses requiring such complicated masks, applying apodisation requires tuning and is not essential to making an unbiased estimate of the cross-correlation power spectra, for the signal under consideration here. Noise in the cross-correlation measurement can also be reduced by using the galaxy weights rather than a binary GWL mask and zero-padding the GWL mask to match a larger CMB mask. We have shown that using the galaxy shear information directly produces results which are consistent with measuring the cross-correlation from a GWL convergence map – with the former method benefiting from fewer additional processing steps and a better estimate of the B-mode null test.

We have also validated our approach by applying it to a previous analysis (Hand et al., 2015) and recovering the published result. This pipeline will be applied to new data from KiDS and ACTPol in chapter 3, and to future CMB lensing and GWL data.

# Chapter 3

# The Kilo Degree Survey Cross-correlation with Lensing from the Atacama Cosmology Telescope

## 3.1 Introduction

Observations of the CMB at high redshift and of galaxy weak lensing (GWL) at lower redshifts are capable of constraining the cosmological model describing our Universe to high precision (e.g Planck Collaboration, 2018; Hildebrandt et al., 2018; Abbott et al., 2018; Hikage et al., 2019). However, there is currently a mild tension between the cosmological parameters inferred from *Planck* measurements of the CMB and from low redshift probes of cosmology such as galaxy redshift surveys (e.g Alam et al., 2017), the galaxy cluster mass function (e.g Bocquet et al., 2019) and GWL (e.g Hildebrandt et al., 2018). It is therefore interesting to investigate how robust the results are and to understand whether this disagreement can be understood in terms of systematic effects or whether new physics is required. Looking ahead, the combination of high and low redshift probes will play an important role in determining the nature of dark energy and the mass of neutrino particles.

By combining data from independent cosmological probes, we can access information about our Universe at multiple epochs while also investigating systematic effects that plague our ability to measure cosmology accurately. In recent years there have been many studies combining a wide array of observations which not only give an alternative insight into cosmological models, but also the astrophysical and instrumental systematic effects. For example, cross-correlating the lensing of the CMB with populations of galaxies (Smith et al., 2007; Hirata et al., 2008; Bleem et al., 2012; Omori & Holder, 2015; Allison et al., 2015; Bianchini et al., 2015; Baxter et al., 2016; Giannantonio et al., 2016; Omori et al., 2019b), quasars (Sherwin et al., 2012; Geach et al., 2013) and clusters (Baxter et al., 2018) can be used to measure the bias of these objects and the growth factor, and cross-correlating lensing of the CMB with the Cosmic Infrared Background (Holder et al., 2013; van Engelen et al., 2015, CIB,) or the thermal Sunyaev-Zel'dovich effect (Van Waerbeke et al., 2014; Hill & Spergel, 2014; Hojjati et al., 2017) tells us about the poorly understood relationship between dark matter and baryons. Forecasts also show how correlating future data sets – for example SO, LSST or *Euclid* – will improve constraints on the evolution and nature of dark energy, the amplitude of matter fluctuations $\sigma_8$, the matter density $\Omega_m$ and the sum of neutrino masses, by better understanding the systematic effects, and by adding information as a function of redshift.

In this study we measure the cross-correlation between GWL and CMB lensing (CMB lensing$\times$GWL), which has been previously studied in Hand et al. (2015); Liu & Hill (2015); Kirk et al. (2016); Harnois-Déraps et al. (2016, 2017); Omori et al. (2019a). CMB lensing and GWL both probe the same underlying matter density field and therefore will be correlated. The GWL kernel peaks at around a redshift

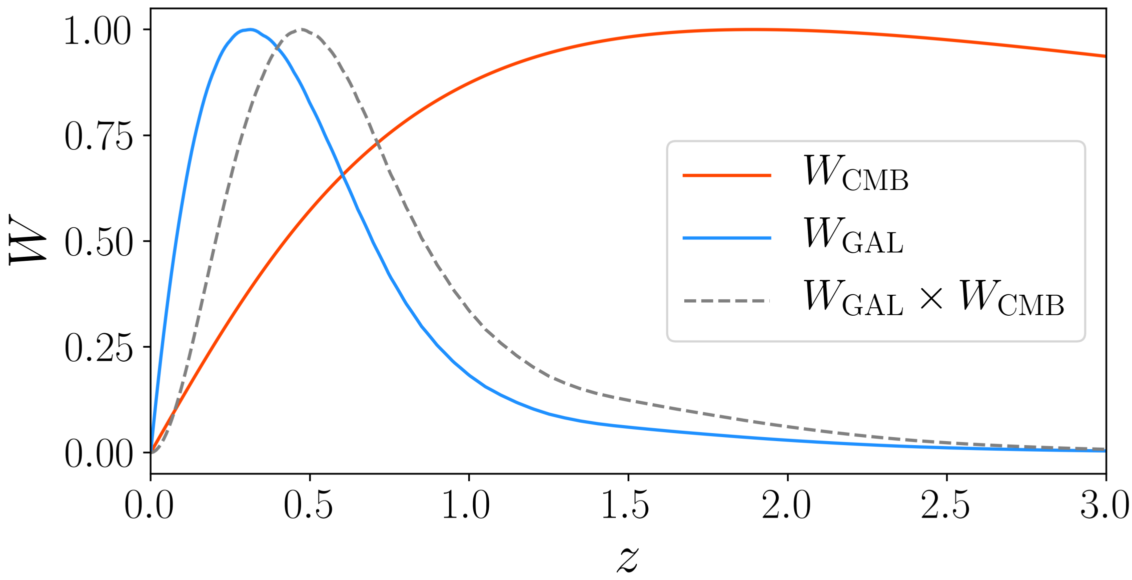


Figure 3.1: The GWL and CMB lensing kernals are shown in blue and orange respectively. The cross-correlation between these two probes selects an intermediate redshift range (shown in grey) over which the matter power spectrum is integrated.

of 0.5 for current data sets and the CMB lensing kernel peaks at a redshift of 2 (as shown in Fig. 3.1 – thus by measuring the CMB lensing×GWL power spectrum we can directly measure the mass distribution at an intermediate redshift, purely from gravitational lensing.

In parallel with constraining cosmology, the CMB lensing×GWL measurement helps constrain information about the biases present in GWL (Hu, 2002; Vallinotto, 2013). These include the shear multiplicative bias, $m$, which is a result of correcting for atmospheric and instrumental distortions which affect the galaxy shape measurement process. It is degenerate with the normalisation of the matter power spectrum and thus impacts the estimation of cosmological parameters. Photometric redshift bias can also be investigated: since the redshifts of galaxies used in GWL surveys are estimated through photometry. they have a large uncertainty associated with them. The CMB lensing kernel is well defined and therefore can be used as a cross-check on the photometric redshift calibration of GWL surveys (Schaan et al., 2017). This measurement can also potentially be used to study other effects which can impact the measurement including baryon feedback mechanisms and intrinsic alignment (Chisari et al., 2015).

In this chapter we measure the CMB lensing$\times$GWL power spectrum using the latest CMB lensing data from the Atacama Cosmology Telescope (ACT) and GWL data from the Kilo Degree Survey (KiDS). These data sets are detailed in section 3.3. Our method for measuring and modelling the cross-correlation is described in section 3.4. We present our results and cosmological parameter fits in 3.5. Here we compare our measured cross-spectrum to a *Planck* and KiDS best fit cosmology. We then perform an MCMC fitting for $\Omega_m$ and $\sigma_8$, marginalising over the GWL systematic biases using informative priors from previous KiDS analyses. Finally we forecast the expected signal-to-noise using the next data release from ACT and use simulated fields to investigate the impact on estimating cosmological parameters with that data set. Finally, a discussion of our conclusions is given in section 3.6.

## 3.2 Previous Results

The first measurement of CMB lensing$\times$GWL used CMB lensing data from ACT combined with GWL data from CS82 (as discussed in chapter 2). There have been five subsequent measurements using the CFHTLenS, RCSLenS, KiDS or DES GWL surveys combined with the *Planck*, ACT or SPT CMB lensing data (Liu & Hill, 2015; Kirk et al., 2016; Harnois-Déraps et al., 2016, 2017; Omori et al., 2019a). Little improvement in the signal-to-noise of this measurement has been made – this is because the overlapping area of the two surveys and noise in the CMB lensing maps are the main aspects driving the signal-to-noise of the measurement. Ground based CMB experiments that have lower noise and better resolution than *Planck*, such as ACT and SPT, have only very recently started to cover large areas, and therefore

| | Data Sets | Area (deg$^2$) | S/N | $A$ |
|---|---|---|---|---|
| Hand et al. (2015) | ACT×CS82 | 129 | 4.2 | $0.78 \pm 0.18$ |
| Liu & Hill (2015) | *Planck*×CFHT | 130 | 2.0 | $0.44 \pm 0.22$ |
| Kirk et al. (2016) | SPT×DES-SV | 139 | 2.9 | $0.88 \pm 0.30$ |
| | *Planck*×DES-SV | 139 | 2.2 | $0.86 \pm 0.39$ |
| Harnois-Déraps et al. (2016) | *Planck*×CFHT | 130 | 2.2 | $0.68 \pm 0.31$ |
| | *Planck*×RCSLenS | 395 | 4.0 | $1.31 \pm 0.33$ |
| Harnois-Déraps et al. (2017) | *Planck*×KiDS-450 | 449 | 3.9 | $0.68 \pm 0.15$ |
| Omori et al. (2019a) | SPT/*Planck* ×DES-Y1 | 1289 | 6.8 | $0.99 \pm 0.17$ |

Table 3.1: Previous measurements of the CMB lensing/GWL cross–correlation. The second column denotes which data sets were used, the third column states the overlapping area of the two surveys used, the fourth column indicates the significance of the detection and the final column displays the amplitude, $A$, which is unity if the results are consistent with a *Planck* ΛCDM cosmology.

cross-correlation measurements should rapidly improve in the near future.

Most CMB lensing×GWL measurements have measured the power spectrum, however the most recent studies (Harnois-Déraps et al., 2016, 2017; Omori et al., 2019a) have applied configurational space estimators. This choice is largely arbitrary and is often driven by the goal to combine cross-correlation analyses with a corresponding auto-analysis. In table 3.1 we summarise all of the CMB lensing×GWL measurements to date, including sky area, significance and estimate of $A$, which is a scaling of the amplitude of the cross-correlation that equals 1 if the measurement agrees with the *Planck* best fit cosmological model (Planck Collaboration, 2018).

Table 3.1 shows that for some of the measurements the amplitude $A$ is lower than expected. There has been some discussion about whether this could be accounted for by a phenomenon known as intrinsic alignment. The morphology of a galaxy is expected to be closely linked to its evolution and therefore environment, for example most elliptical galaxies are thought to be the consequence of major merging events and there have been claims that cluster galaxies are preferentially orientated towards the central galaxy (van Uitert & Joachimi, 2017). The coherent distortions of galaxy shapes resulting from gravitational lensing can be imitated or concealed by this intrinsic alignment of galaxy shapes caused by galaxy formation and evolution (see Kirk et al., 2015, and references therein). Intrinsic alignment has two forms, the first being II which is a correlation between the shapes of pairs of galaxies that have been tidally aligned since they inhabit the same dark matter halo – this results in a positive correlation. The second, GI, occurs since distant galaxies are aligned due to lensing by foregrounds structure, and the galaxies within this foreground structure are aligned in the opposite direction due to tidal forces. What is most troubling for cross-correlation measurements is that the intrinsic alignment of galaxies will be anti-correlated with CMB lensing convergence – analogous to the GI term – and result in a reduction in the cross-correlation amplitude (Hirata & Seljak, 2004). Hall & Taylor (2014) found that for a sample with a redshift distribution similar to that of CS82, intrinsic alignment leads to a 15-20% decrease in the amplitude of the cross-correlation signal. However it should be noted that this is dependent on the shape of the redshift distribution and the type of source galaxies sampled in the GWL survey. Furthermore, Chisari et al. (2015) showed this was dependent on type of galaxy with red galaxies leading to around a 10% shift in the amplitude and blue galaxies showing no alignment. Both of these investigations displayed that deeper surveys would have less contamination although intrinsic alignments are poorly understood at higher redshifts.

Previous studies have also shown that the cross-correlation signal is greatly impacted by the uncertainty in the redshift distribution of the source galaxies. Changes to the peak of the redshift distribution and its high-redshift tail could potentially lead to changes of order 10-20% (Hand et al., 2015). However this is dependent on the depth of the data set and whether there is a suitable spectroscopic survey overlapping which can be used for calibration.

Finally, Harnois-Déraps et al. (2017) show that baryonic feedback suppresses the cross-correlation power spectrum at large $\ell$-bins, and it is also a well-known effect that massive neutrinos reduce the amplitude of the power spectrum. To date, these

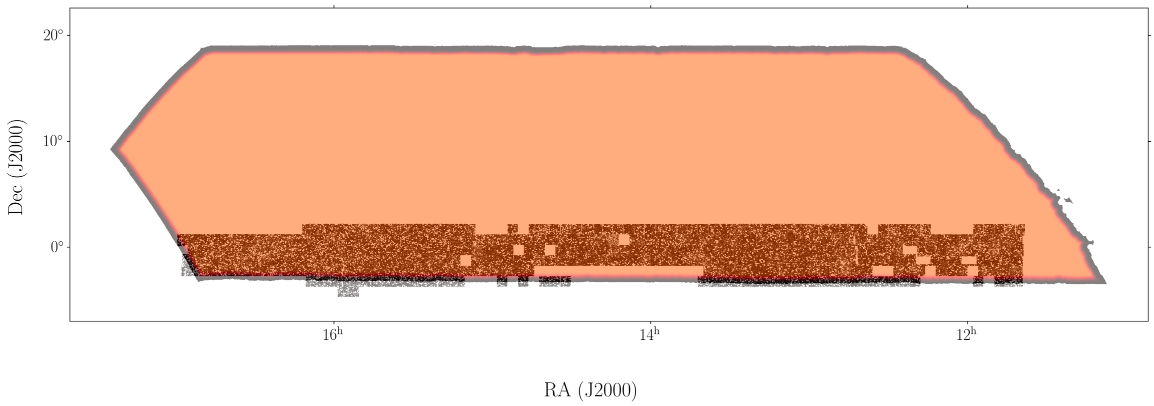


Figure 3.2: The KiDS K-1000 data shares a masked area of 275 deg$^2$ with the ACT BOSS-North lensing area, shown here as the larger area in light orange. The K-1000 mask is the smaller darker region.

two effects are sub-dominant given the signal-to-noise of the measurements.

# 3.3 Data

## 3.3.1 CMB Lensing

The CMB lensing convergence map used in this analysis is reconstructed from arcminute-resolution maps of the temperature and polarisation anisotropy observed by the Atacama Cosmology Telescope Polarimeter (ACTPol), described in Aiola et al. (in prep.). The data set used for the lensing reconstruction includes observations taking during 2014 and 2015 in the 90GHz and 150 GHz frequency bands, and consists of two patches of sky on the celestial equator of which we use the 'BOSS-N' region which overlaps with the area covered by KiDS. The entire BOSS-N region covers approximately 1500 deg$^2$ as shown in Fig. 3.2 as the larger area in light orange; the overlap region that we use is 275 deg$^2$. The effective white noise level of the ACT maps is $\Delta_T = 21\mu K$-arcmin for temperature and $\Delta_P = \sqrt{2}\Delta_T$ for polarisation; at large scales atmospheric noise dominates. The estimation of the convergence map and associated simulations used in this work is described in Darwish et al. (in prep.).

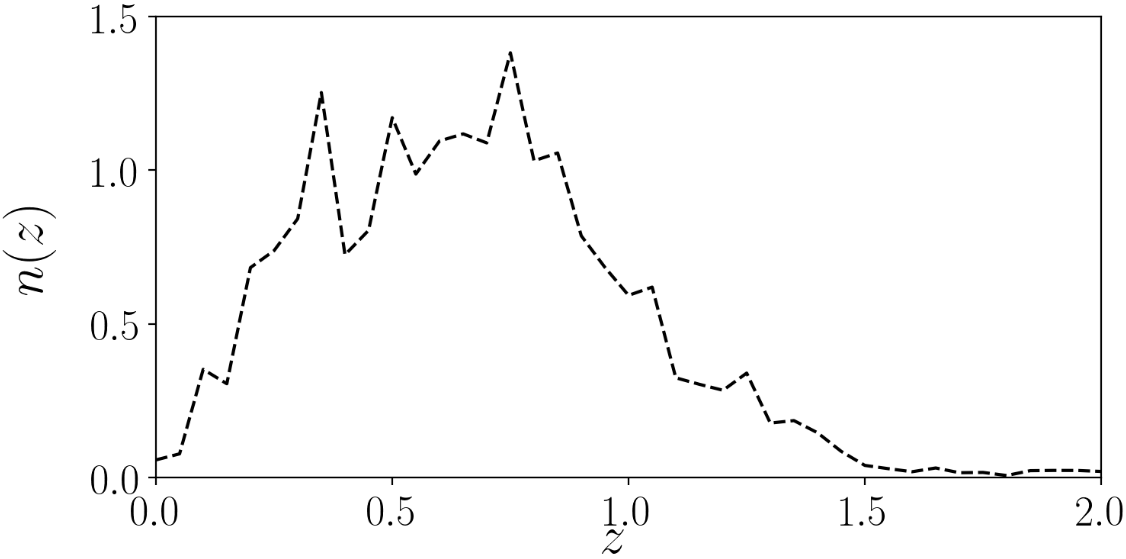


Figure 3.3: The redshift distribution of galaxies in the K-1000 catalogue. This is derived from the methods presented in Hildebrandt et al. (2018) which uses infra-red data from VIKING.

### 3.3.2 Galaxy Weak Lensing

KiDS is on ongoing optical wide-field imaging survey with the OmegaCAM camera on the VLT Survey Telescope. It measures the weak gravitational lensing of galaxies out to a redshift of around 1. In its complete state it will consist of 1350 square degrees split across two patches of sky – one along the equator and the other in the south – so that observations can be taken throughout the year. The KiDS North region benefits from overlapping with the GAMA spectroscopic survey as well as a single pointing in the COSMOS field which has 30-band photometry. KiDS observes the sky in four bands $\{u, g, r, i\}$. The $r$-band data is taken during dark time and has the best conditions for seeing, so these images are used for estimating the shapes of the galaxies. By design the same area of sky has also been observed by the VISTA Kilo-degree Infared Galaxy survey (VIKING) using the VISTA telescope in the $Z, Y, J, H$ and $K_s$ bands. Thus combining the KiDS and VIKING data sets produces a 9-band imaging survey.

The latest KiDS data release (DR4) (Kuijken et al., 2019) covers 1000 square degrees of sky (K-1000), of which we use the more northern patch that overlaps with the CMB lensing data from ACTPol, described in the previous section. The addition of VIKING photometry in this data release has led to the inclusion of source galaxies up to a redshift of 1.2, which improves the overlap of the GWL and CMB lensing window functions. The redshift distribution of the KiDS galaxies is shown in Fig. 3.3. The improved homogeneity in K-1000 makes it ideal for cross-correlation measurements as the mask contains fewer sharp features (discussed in chapter 2). There are $\sim 9$ million galaxies with shape measurements in this overlapping region. The lensing shape catalogues used in this analysis have been blinded such that estimated cosmological parameters should be displaced by of order $1\sigma$ from their true values. The blinding process, detailed in (Hildebrandt et al., 2017), involves perturbing the shear and weight values that are derived from the real measurements through parameterised smooth functions designed to prevent easy identification of the true data set. The amplitude of these changes to the catalogue is adjusted to guarantee that the best-fit $S_8$ values from the primary KiDS cosmic shear analysis differs by at least the $1\sigma$ error on the *Planck* measurement (Planck Collaboration, 2018).

## 3.4 Methods

In this section we describe the methods we use to measure the cross-correlation between the two lensing maps – plus its associated uncertainty – and to model the resulting signal.

### 3.4.1 Power Spectrum Estimation

Starting from the shape catalogue we construct shear maps by taking the weighted average of the galaxy ellipticities in pixels with 0.5 arcminute resolution, which map onto the ACT CMB lensing convergence maps. A galaxy weight map is also created by taking the sum of the galaxy weights in the corresponding pixel. The galaxy weights, defined in Miller et al. (2013), are derived from the shape measurement process, such that a galaxy with a larger weight has a more precisely known ellipticity. We apply the same source galaxy selection (photometric redshift and shape measurement flags) in our analysis as the corresponding KiDS cosmic shear study (Hildebrandt et al., 2018).

From these maps, we measure the CMB lensing/GWL cross-correlation power spectrum with the pipeline discussed in the previous chapter, which uses the NaMaster (Alonso et al., 2019) pseudo-$C_\ell$ estimator. Here we briefly review the pipeline, highlighting aspects which differ from some previous analyses. We zero-pad both maps to use all the data available in the ACT BOSS-North and K-1000 regions. Rather than applying the GWL binary mask we use the KiDS galaxy weights to maximise the signal-to-noise of the measurement and we do not apply any apodisation so that the available area is not reduced. Instead of reconstructing GWL convergence, we work directly with the two components of shear $(\gamma_1, \gamma_2)$, equivalent to using Stokes Q and U vectors for a CMB polarisation analysis.

From the three fields, $\kappa_C, \gamma_1, \gamma_2$, we estimate the correlation of the GWL E-mode with the CMB lensing convergence ($\kappa_C \gamma_E$). The NaMaster code first calculates the 2D pseudo-power spectrum which is then averaged in annuli to estimate the 1D spectrum. A mode coupling matrix is calculated from the masks applied to their respective fields. The inverse of the binned mode coupling matrix, is then applied to the 1D spectrum to recover an unbiased estimate of the cross-correlation. This method also produces an estimate of the correlation with the GWL B-mode as a by-product ($\kappa_C \gamma_B$). This is expected to be null. For faster computation of the mode coupling matrix, we perform a curved sky analysis.

### 3.4.2 Covariance

The covariance of the cross-correlation power spectrum is estimated using a suite of ACT CMB lensing simulations as described in Aiola et al. (in prep.) and Darwish et al. (in prep.). These each have a different signal and noise realisation, with noise realisations that approximate the noise in the CMB lensing maps. Simulations like this that do not correlate the CMB lensing and GWL signals are adequate for estimating the covariance matrix provided that

$$(C_\ell^{\kappa_C\kappa_C} + N_\ell^{\kappa_C\kappa_C})(C_\ell^{\gamma_E\gamma_E} + N_\ell^{\gamma_E\gamma_E}) \gg C_\ell^{\kappa_C\gamma_E}. \tag{3.1}$$

This is satisfied for this analysis where the CMB lensing auto-spectrum and noise spectrum are the dominant components.

To construct the covariance matrix we measure the cross-power spectrum between 500 simulated CMB lensing maps and the KiDS GWL data maps, $C_\ell^{\kappa_C\gamma_E}$, and then estimate the covariance matrix from these measurements, as

$$Q_{\ell,\ell'}^{\kappa_C\gamma_E} = \langle \Delta C_\ell^{\kappa_C\gamma_E} \Delta C_{\ell'}^{\kappa_C\gamma_E} \rangle \,. \tag{3.2}$$

With future experiments the noise will be lower such that correlated simulations will be required to estimate the covariance.

### 3.4.3 Modelling

#### 3.4.3.1 Theoretical Cross-correlation Power Spectrum

Our theoretical model for the unbinned cross-correlation power spectrum is given by

$$C_\ell^{ij} = \int_0^{\chi_H} d\chi \frac{W_i(\chi) W_j(\chi)}{f_k(\chi)^2} P(k, \chi) \,, \tag{3.3}$$

where $i$ and $j$ denote $\kappa_C$ and $\gamma_{E,B}$, $W_i(\chi)$ is the window function, $\chi$ is the comoving distance, $f_k(\chi)$ is the angular diameter distance and $P(k, \chi)$ is the 3D matter power spectrum at a given comoving distance. The general form for the window function for lensing is

$$W_i(\chi) = \frac{3\Omega_m H_0^2}{2c^2} \frac{f_k(\chi)}{a(\chi)} \int_\chi^{\chi_H} d\chi' p_i(\chi') \frac{f_k(\chi' - \chi)}{f_k(\chi')} \,, \tag{3.4}$$

where $p(\chi)$ is the probability distribution function. For CMB lensing, this is given by

$$p_{\rm CMB}(\chi) = \delta(\chi - \chi^*) \,, \tag{3.5}$$

since the CMB is on a single source plane and $\chi^*$ is the comoving distance to the surface of last scattering. For GWL, this is given by

$$p_{\rm GAL}(\chi) = n(z) \frac{dz}{d\chi} \,, \tag{3.6}$$

and $n(z)$ is the number of galaxies as a function of redshift.

The theoretical cross-correlation power spectrum is calculated using the Core Cosmology Library (CCL)[1] (Chisari et al., 2019). We extend this framework to include systematic effects present in the GWL data, for a more complete model, which we describe in the following subsections.

The model binned power spectrum, which accounts for the mode coupling matrix as described in the previous chapter, is given by

$$m = C_b = (M_b)^{-1} B\{M C_\ell\} \,, \tag{3.7}$$

where $M$ is the mode coupling matrix, with the subscript $b$ denoting the binned version and $B$ is the binning matrix.

[1]https://github.com/LSSTDESC/CCL

#### 3.4.3.2 Photometric Redshift Bias

Biases resulting from photometric redshifts has been shown to effect the cross-correlation by up to 10% in previous analyses (Hand et al., 2015). This is due to the fact that photometric redshift estimation becomes most uncertain in the high redshift tail because of a lack of spectroscopic data covering this redshift range. Errors in the photometric redshift distribution can be accounted for by modelling this bias as a shift in the redshift distribution, as

$$n(z)_{\rm biased} = n(z + \Delta z)\,, \tag{3.8}$$

where $n(z)_{\rm biased}$ is the observed redshift distribution. The photometric redshift bias, $\Delta z$ is expected to be dependent on redshift also, but given the expected signal-to-noise of our measurement this parameterisation is sufficient. Shifting the redshift distribution by $\Delta z$ changes the GWL window function which impacts the amplitude of the cross-correlation power spectrum. We assign a Gaussian prior to $\Delta z$ which comes from Hildebrandt et al. (2018) and is shown in table 3.2. This prior corresponds to the uncertainty in the redshift distribution, which is the 68% confidence interval estimated from a spatial bootstrap resampling of the spectroscopic redshift calibration sample.

#### 3.4.3.3 Multiplicative Bias

The multiplicative bias, $m$, accounts for the uncertainty in calibrating the shapes of galaxies, which is the remaining bias left in the shear estimation post calibration. This can account for selection bias, false object detection, star contamination and shape measurement failures. We therefore include the standard calibration bias as

$$C_{\ell,\rm obs}^{\kappa\gamma_E} = (1+m)C_\ell^{\kappa\gamma_E}\,. \tag{3.9}$$

We assign a Gaussian prior to this based on the analysis presented in Hildebrandt et al. (2018), detailed in table 3.2. A non-zero multiplicative bias will result in a shift in the amplitude of the cross-correlation power spectrum.

#### 3.4.3.4 Intrinsic Alignment

As discussed in section 3.1, galaxies do not only appear aligned due to the effect of lensing but can also be intrinsically aligned due to interactions with the local tidal field from the LSS which galaxies inhabit. This effect is captured in CCL, which employs a standard non-linear alignment model (Hirata & Seljak, 2004) which states that the intrinsic galaxy inertia tensor is proportional to the local tidal tensor. This enters our model as

$$C^{\kappa_C \gamma_E}_{\mathrm{obs}}(\ell) = C^{\kappa_C \gamma_E}(\ell) + C^{\kappa_C \gamma_{\mathrm{IA}}}(\ell) \tag{3.10}$$

where $C^{\kappa_C \gamma_{\mathrm{IA}}}(\ell)$ accounts for the cross-correlation between the intrinsic alignments of galaxies and the CMB lensing convergence. This essentially requires changing the window function in equation 3.4 to

$$W_{\mathrm{IA}}(\chi) = F(z) n(z) \frac{dz}{d\chi} \,. \tag{3.11}$$

Here, $F(z)$ is equivalent to the product of the so-called alignment bias, $b_{\mathrm{IA}}$, and the fraction of aligned galaxies in the sample, $f_{\mathrm{IA}}$, which we model as

$$F(z) = A(z) \frac{-C_1 \rho_c \Omega_m}{D(z)} \quad , \quad A(z) = A^{\mathrm{IA}} \left[ \frac{1+z}{1+z_0} \right]^{\eta^{\mathrm{IA}}} \left[ \frac{L}{L_0} \right]^{\beta^{\mathrm{IA}}} \quad , \tag{3.12}$$

where $A^{\mathrm{IA}}$ is a constant which describes the amplitude of the cross-correlation. Any redshift and luminosity dependence is captured by $\eta^{\mathrm{IA}}$ and $\beta^{\mathrm{IA}}$, but given the signal-to-noise of the measurement we fix these both to zero and simply fit for the amplitude $A^{\mathrm{IA}}$. We apply a Gaussian prior from Johnston et al. (2019); this intrinsic alignment study was performed on the same galaxy sample used in our analysis.

### 3.4.4 Estimating Parameters

#### 3.4.4.1 Likelihood and Sampling

We construct a simple Gaussian likelihood for the data vector of the measured cross-correlation power spectrum $\boldsymbol{d}$, given a model $\boldsymbol{m}$, produced from a set of parameters $\boldsymbol{p}$,

$$\ln \mathcal{L}(\boldsymbol{d}|\boldsymbol{m}(\boldsymbol{p})) = -\frac{1}{2}(\boldsymbol{d} - \boldsymbol{m}(\boldsymbol{p}))^T Q^{-1}_{b,b'}(\boldsymbol{d} - \boldsymbol{m}(\boldsymbol{p}))\,, \tag{3.13}$$

to within an overall additive normalisation factor.

The parameters of our cosmological model are shown in table 3.2. The model has two free cosmological parameters ($\Omega_m$ and $\sigma_8$) and three systematics parameters ($m$, $\Delta z$ and $A^{\rm IA}$). The other cosmological parameters are fixed to fiducial values for which we take the *Planck* values as nominal (Planck Collaboration, 2018). The priors are also shown in table 3.2. Here, square brackets refer to a uniform prior and curved brackets correspond to a Gaussian prior.

We also consider a simpler case where no cosmological parameters are varied, and instead the theoretical spectrum for the fiducial cosmological model is scaled by a free amplitude, $A$, as in Hand et al. (2015). Here we compare to both a *Planck* and KV-450 best fit cosmology.

To estimate the five free parameters, we use the affine-invariant MCMC sampling code emcee[2] (Foreman-Mackey et al., 2013). The posterior distribution of the model parameters is given by

$$P(\boldsymbol{m}(\boldsymbol{p})|\boldsymbol{d}) \propto \mathcal{L}(\boldsymbol{d}|\boldsymbol{m}(\boldsymbol{p}))P_{\rm prior}(\boldsymbol{p})\,, \tag{3.14}$$

where the model parameters have a prior given by $P_{\rm prior}(\boldsymbol{p})$.

[2]http://dfm.io/emcee/current/

| Parameter | *Planck* | KV-450 | Prior |
|---|---|---|---|
| $\Omega_m$ | 0.31 | 0.26 | [0.1,0.9] |
| $\sigma_8$ | 0.81 | 0.84 | [0.5,1.5] |
| $\Omega_b$ | 0.04 | 0.04 | fixed |
| $h$ | 0.67 | 0.75 | fixed |
| $n_s$ | 0.97 | 1.02 | fixed |
| $m$ | 0.0 | 0.0 | (0.0,0.02) |
| $\Delta z$ | 0.0 | 0.0 | (0.0,0.027) |
| $A^{\mathrm{IA}}$ | 0.0 | 0.0 | (1.06,0.47) |

Table 3.2: In this analysis we evaluate the amplitude of the cross-correlation in the context of both a *Planck* and KV-450 best-fit cosmology, the key parameters of which are specified in the respective columns. We use the *Planck* values as our fiducial model. The final column contains the prior – square brackets correspond to a uniform prior, curved brackets correspond to a Gaussian prior centred on the first number with the width given by the second value.

#### 3.4.4.2 Degeneracies

We show how the power spectrum changes when each of these parameters is individually varied in Fig. 3.4. It is clear that since the cross-correlation power spectrum is featureless across the range of scales we can measure, these parameters are all essentially variations on the amplitude and therefore highly degenerate with each other. For the multiplicative bias and photometric redshift bias ($m$ and $\Delta z$) we show a level of variation spanning twice the width of the prior. Since this appears as only a small variation in the power spectrum given the expected signal-to-noise of the measurement, we anticipate being prior dominated for these parameters. Nevertheless, we are using informative priors and investigate the impact of these choices on our cosmological modelling of the measured signal.

## 3.5 Results

In this section we present results based on the blinded KiDS data. When unblinded, we can expect cosmological parameter estimates to shift by order $1\sigma$. Our results and interpretation will be updated when the KiDS data are unblinded.

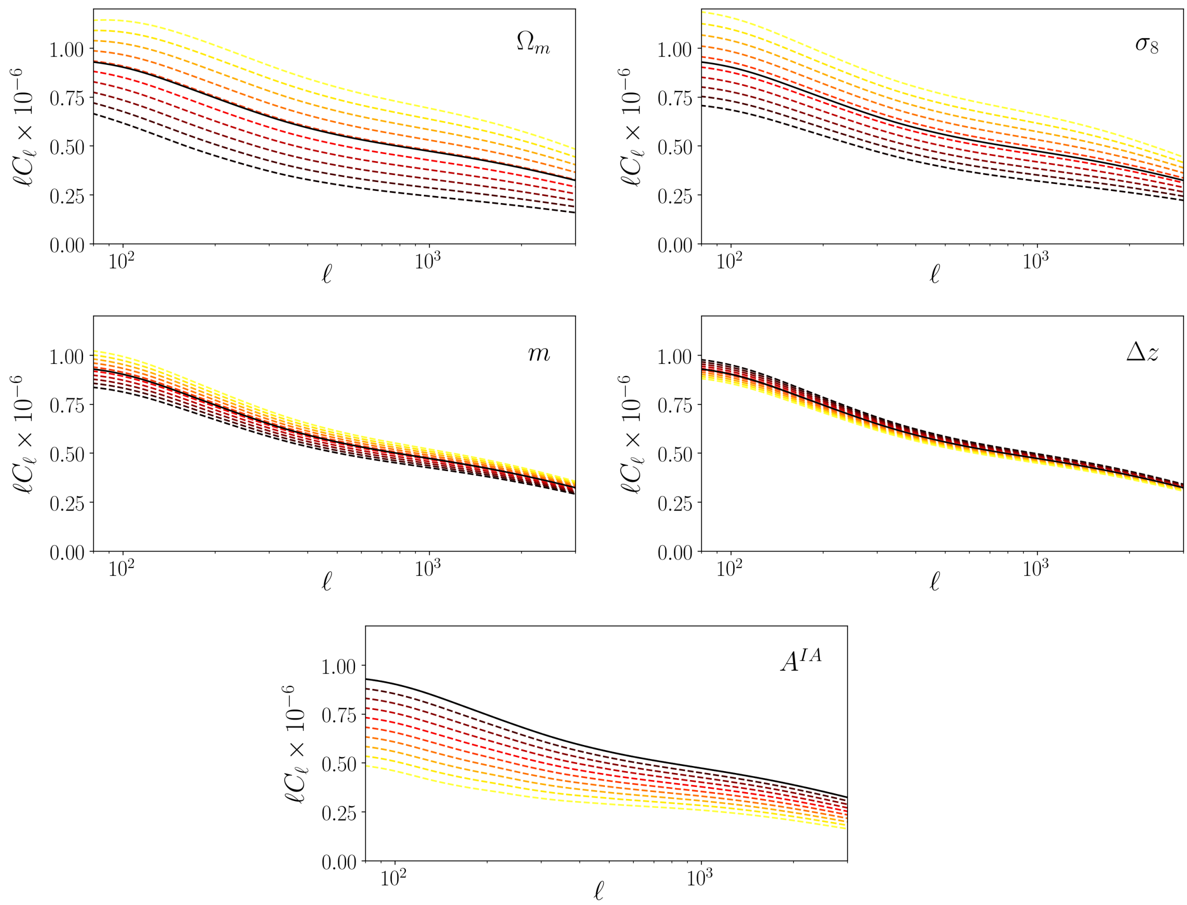


Figure 3.4: The effect on the cross-correlation power spectrum as a result of varying cosmological and systematic parameters individually while fixing the others to their fiducial *Planck* values, given in table 3.2. Light colours correspond to high values and dark colours correspond to low values of a given parameter.

### 3.5.1 KiDS×ACT Power Spectrum

We measure the cross-correlation power spectrum, $C_\ell^{\kappa_C \gamma_E}$ in 5 logarithmically spaced bins between $\ell = 50$ and $\ell = 3000$. This is shown in Fig. 3.5 where the dashed black line corresponds to our fiducial *Planck* cosmology model and its binned counterpart are the open circles. The cross-correlation is detected with a $4.7\sigma$ significance, compared to a model with zero signal. This indicates that, as expected, the cosmic shear and CMB lensing are tracing the same dark matter fluctuations. In comparison to previous measurements this has a similar signal-to-noise to Hand et al. (2015). The area considered here is larger (275 deg$^2$ compared to 129 deg$^2$), but the CMB lensing noise is higher across the wider field[3] and the number density of KiDS is lower than that of CS82 (7.2 arcmin$^{-2}$ compared to 15.8 arcmin$^{-2}$).

### 3.5.2 Testing the Measurement

We use the B-mode cross-correlation to assess whether there has been any E to B mode leakage due to masking, or any B-mode component produced from systematic effects in the shape measurement process.

The B-mode cross-correlation power spectrum is shown in Fig. 3.5. There is excess power in the bin at $\ell \sim 1000$, at the $2 - 3\sigma$ level. The $\chi^2$ for the five data points, compared to null, is 15.6, which has a probability of 0.8% to exceed. This is unlikely to be explained as a statistical fluctuation. The power spectrum estimator pipeline has been tested on simulations, particularly the impact of masking as shown in the previous chapter. Using the data we test the impact of not using galaxy weights, cutting out a smaller region away from the apodised ACT mask and splitting the area into smaller sections. In all cases we find a consistent $C_\ell^{\kappa_C \gamma_B}$ spectrum[4]. We therefore

[3]This analyses uses just the ACT 2014-15 night-time data; additional data has since been collected.

[4]This analysis uses lensing maps from ACT that are almost finalized for public release, but could contain some residual SZ contamination. Our analysis will be updated with the publication-quality lensing maps.

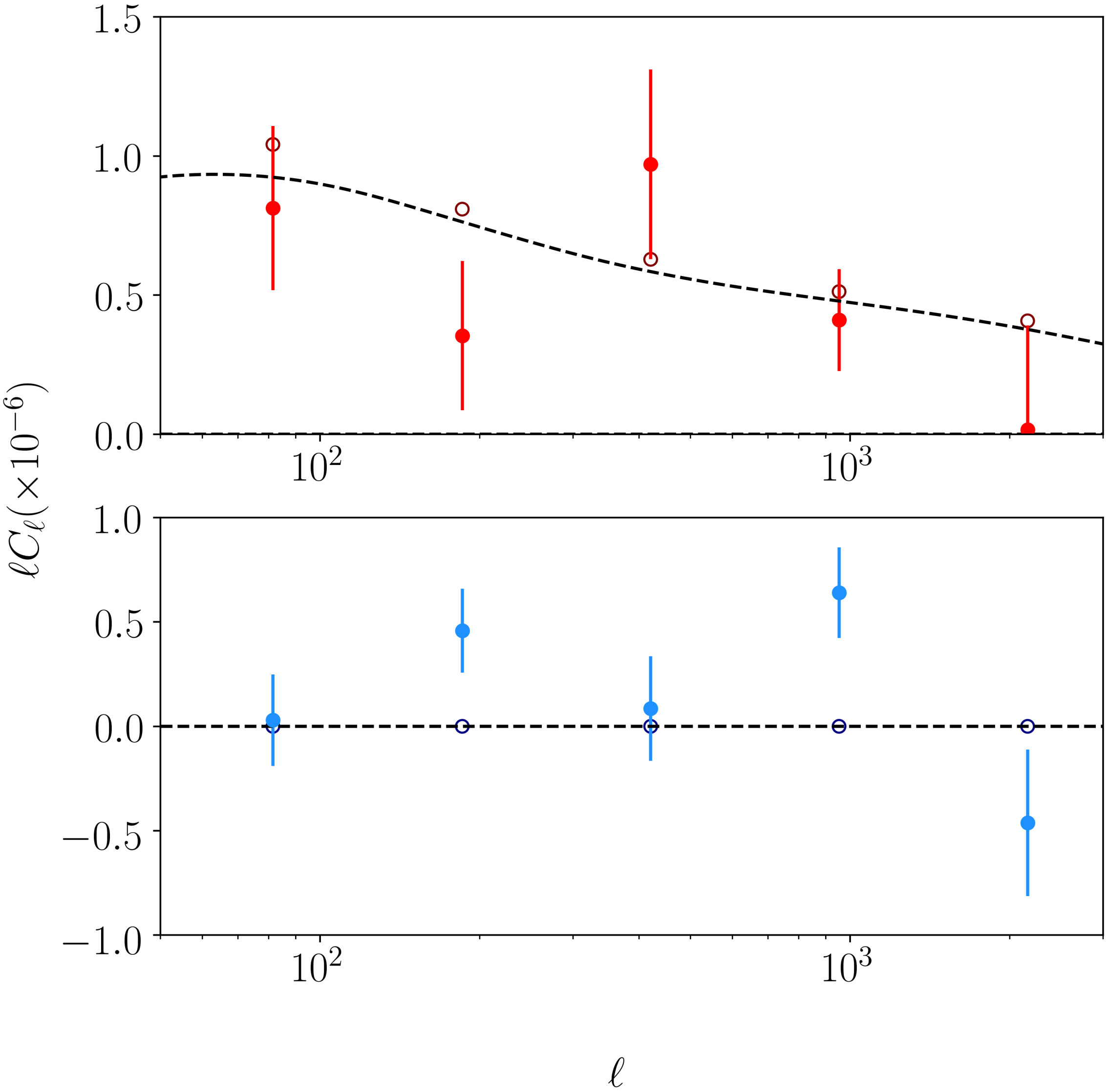


Figure 3.5: Top: the E-mode component of the ACT×K-1000 power spectrum, $C_\ell^{\gamma_E}$. The *Planck* best-fit model is plotted (dashed black line) and the open circles correspond to the binned spectrum. We detect non-zero correlation power at $4.7\sigma$ significance. Bottom: The B-mode null test, $C_\ell^{\gamma_B}$, which is consistent with zero with a PTE of 0.8%.

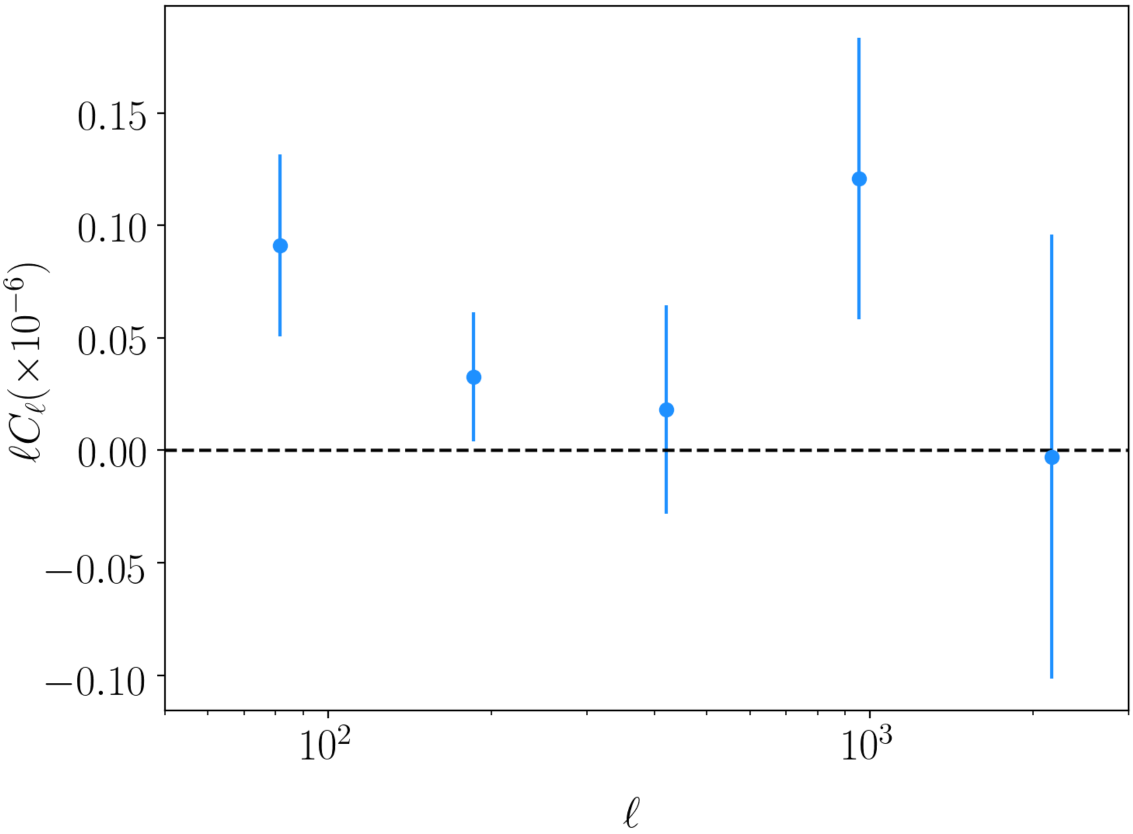


Figure 3.6: We test for systematic effects in the GWL data by measuring the cross-correlation with a set of 50 GWL shear maps where the galaxies have been randomly rotated. We find that this cross-spectrum is consistent with zero as expected.

leave additional exploration to further analysis when more data are available.

We also perform a randoms test, which involves randomly rotating the galaxies and remeasuring the cross-correlation on the random map. This checks for any residual linear bias c-term correction in the GWL data. Figure 3.6 shows the result of this randoms test, for $C_\ell^{\kappa_C \gamma_E}$. With $\chi^2 = 11.0$ compared to null, the test passes with a probability to exceed of 4%.

### 3.5.3 Amplitude Fit

We first perform the single-parameter fit, constraining the amplitude $A$ of the cross-correlation power spectrum, relative to the fiducial *Planck* (Planck Collaboration,

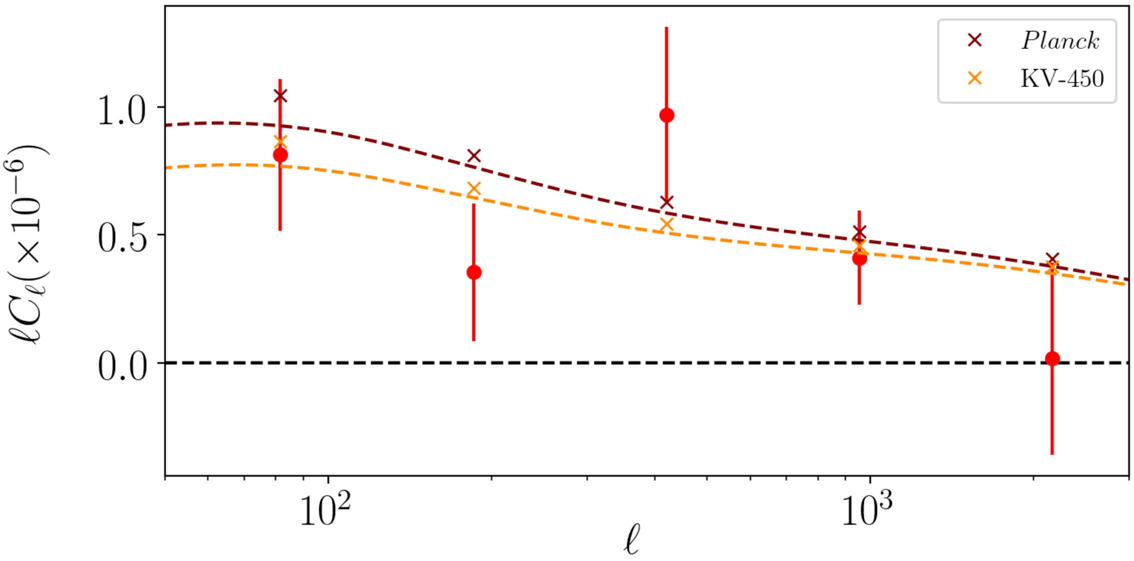


Figure 3.7: The theoretical cross correlation power spectrum assuming a *Planck* and KV-450 cosmology. The single points are the binned power spectrum.

2018) cosmology detailed in the second column of table 3.2. If the data is consistent with a *Planck* cosmology we would expect to find $A_{Planck} = 1$ to within the uncertainties. We find $A_{Planck} = 0.78 \pm 0.14$, consistent with unity at the 1-2$\sigma$ level and a $> 5\sigma$ detection significance. This amplitude is consistent with previous cross-correlation analyses.

Given the current mild state of tension between GWL and CMB experiments it is interesting to examine whether our measurement of the cross-correlation is more consistent with a *Planck* or a KV-450 cosmology (Hildebrandt et al., 2018). Figure 3.7 shows the cross-correlation for the two different cases when we assume a *Planck* cosmology (in red) or a KV-450 cosmology (in orange). It is clear that given our error budget we are unable to robustly distinguish between the two cases. Nevertheless, comparing to a KV-450 cosmology – specified in the third column of table 3.2 – we find $A_{\mathrm{KV-450}} = 0.87 \pm 0.16$. The cross-spectrum is consistent with both models.

It should be noted that in both cases here we have assumed zero intrinsic alignment contribution, so that we can compare our results to previous cross-correlation studies. Re-performing the fit, but assuming the intrinsic alignment amplitude is $A_{\rm IA} = 1.06$ (Johnston et al., 2019), we find $A_{Planck,{\rm IA}} = 0.90 \pm 0.15$ and $A_{\rm KV-450,IA} = 1.00 \pm 0.17$. As expected the inclusion of a non-zero intrinsic alignment amplitude improves the consistency between our measurement and both models.

### 3.5.4 Cosmological Parameter Fits

Here we perform the 5-parameter fit, with resulting parameter distributions for the cosmological and systematics parameters shown in Fig. 3.8. Our constraints on the GWL systematic parameters ($m$, $\Delta z$ and $A^{IA}$) are dominated by the imposed priors, and given the relatively low signal-to-noise of our measurement we would not expect to be able to constrain both cosmological and GWL systematics parameters simultaneously.

The cosmological parameters $\sigma_8$ and $\Omega_m$ are strongly correlated, as seen in previous similar analyses. They are also highlighted in Fig. 3.9, which shows the comparison to the same parameters estimated using the KV-450 shear auto-signal (Hildebrandt et al., 2018). The errors from the cross-spectrum (this result) are larger but the model is consistent.

Weak gravitational lensing is mainly sensitive to the parameter combination $S_8 = \sigma_8\sqrt{\Omega_m/0.3}$, which we also show in Fig. 3.9. We find $S_8 = 0.75 \pm 0.08$ at 68% confidence. This is consistent with the analysis of KV-450 which found $S_8 = 0.74^{+0.04}_{-0.03}$ (Hildebrandt et al., 2018).

### 3.5.5 AdvancedACT×K-1000 Forecast

Finally we consider prospects for improving this result from the next data release from ACT, which will have a reduced noise level across the area overlapping with KiDS. Using the expected noise level of 10 $\mu$K-arcmin, we forecast the signal-to-noise of that measurement to be $\sim 10\sigma$ using the current K-1000 GWL data.

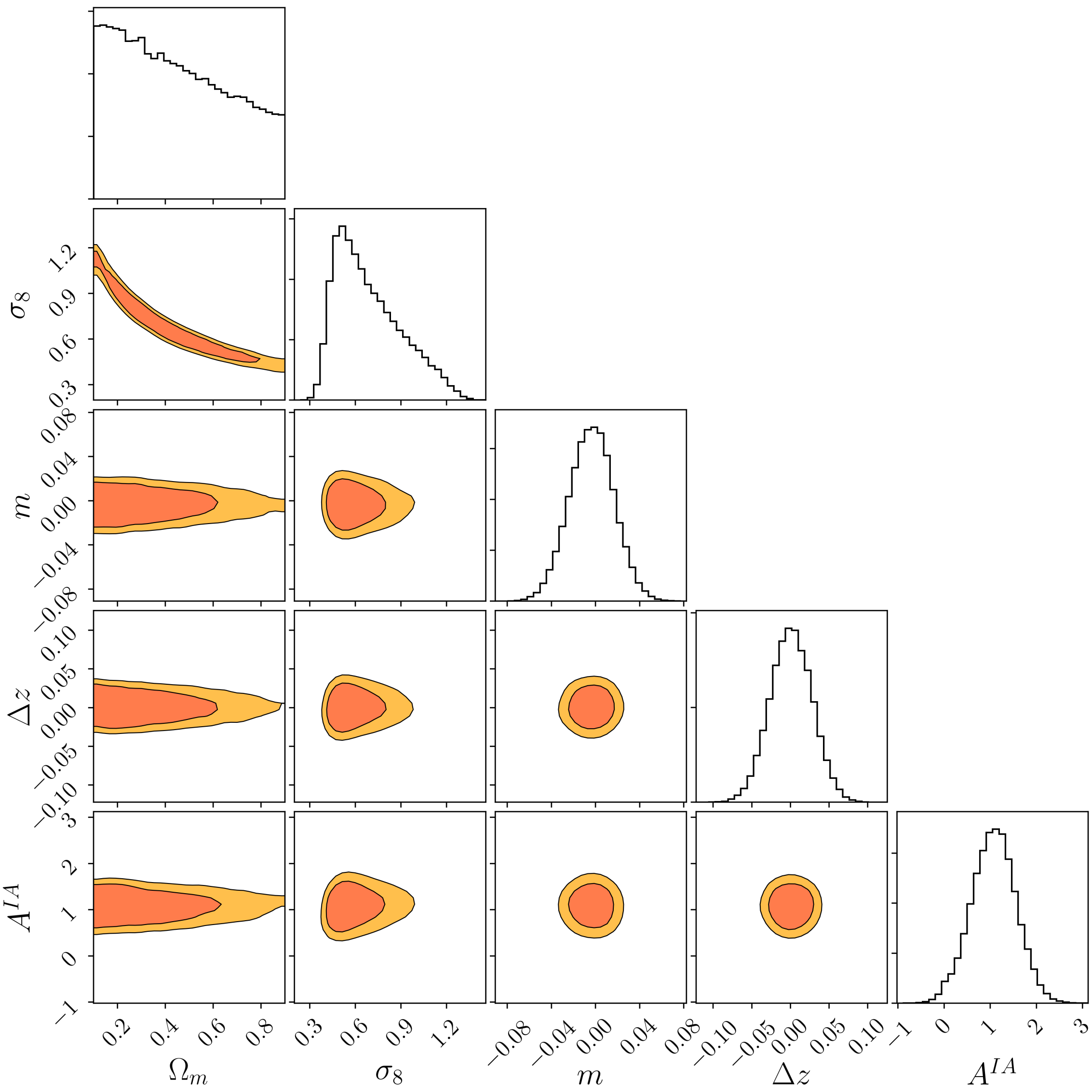


Figure 3.8: Posterior distributions for the five parameters estimated from the ACT-KiDS lensing cross-spectrum, using prior distributions detailed in table 3.2. The two cosmological parameters, $\sigma_8$ and $\Omega_m$, have a well-known degeneracy.

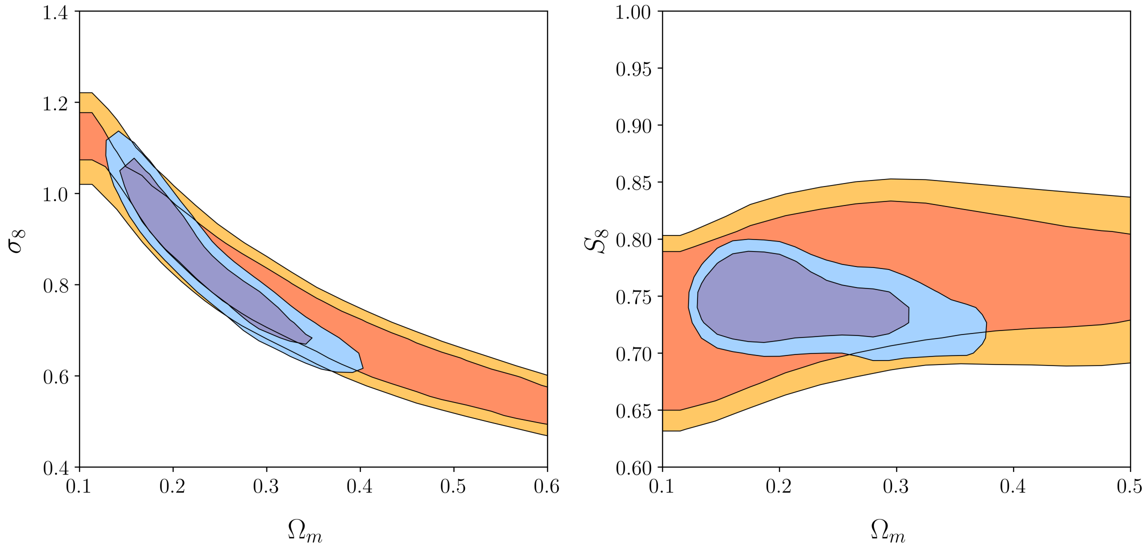


Figure 3.9: Left: the posterior distributions for the amplitude of matter fluctuations, $\sigma_8$, and the matter density, $\Omega_m$ shown in orange, compared to results from the KV-450 auto-spectrum, shown in blue. Right: Alternative parameterisation of these two parameters, with $S_8 = \sigma_8\sqrt{\Omega_m/0.3}$.

We investigate the impact of the improved data set on our ability to constrain cosmology, using a simulated cross-correlation power spectrum shown in Fig. 3.10. This simulation assumes a *Planck* cosmology and GWL systematics; $m = -0.003$, $\Delta z = 0.01$ and $A_{\mathrm{IA}} = 0.9$. The noise reflects our expectations for the next ACT data release. The error bars are estimated using the Knox equation using noise spectra measured from real ACT data maps. We fit this simulated data with our model described in section 3.4, using the priors described in table 3.2. We find our error on $S_8$ would reduce from 0.08 to 0.05, with the predicted parameter contours shown in Figure 3.11.

We examine the consequences of loosening the priors on the GWL systematics parameters, since we found in the previous section that our results are dominated by the priors we applied. In the first case we choose the priors to be Gaussian with the same mean but double the width, and in the second case we set the priors to be uniform – these are both detailed in table 3.3. In all three cases we recover the

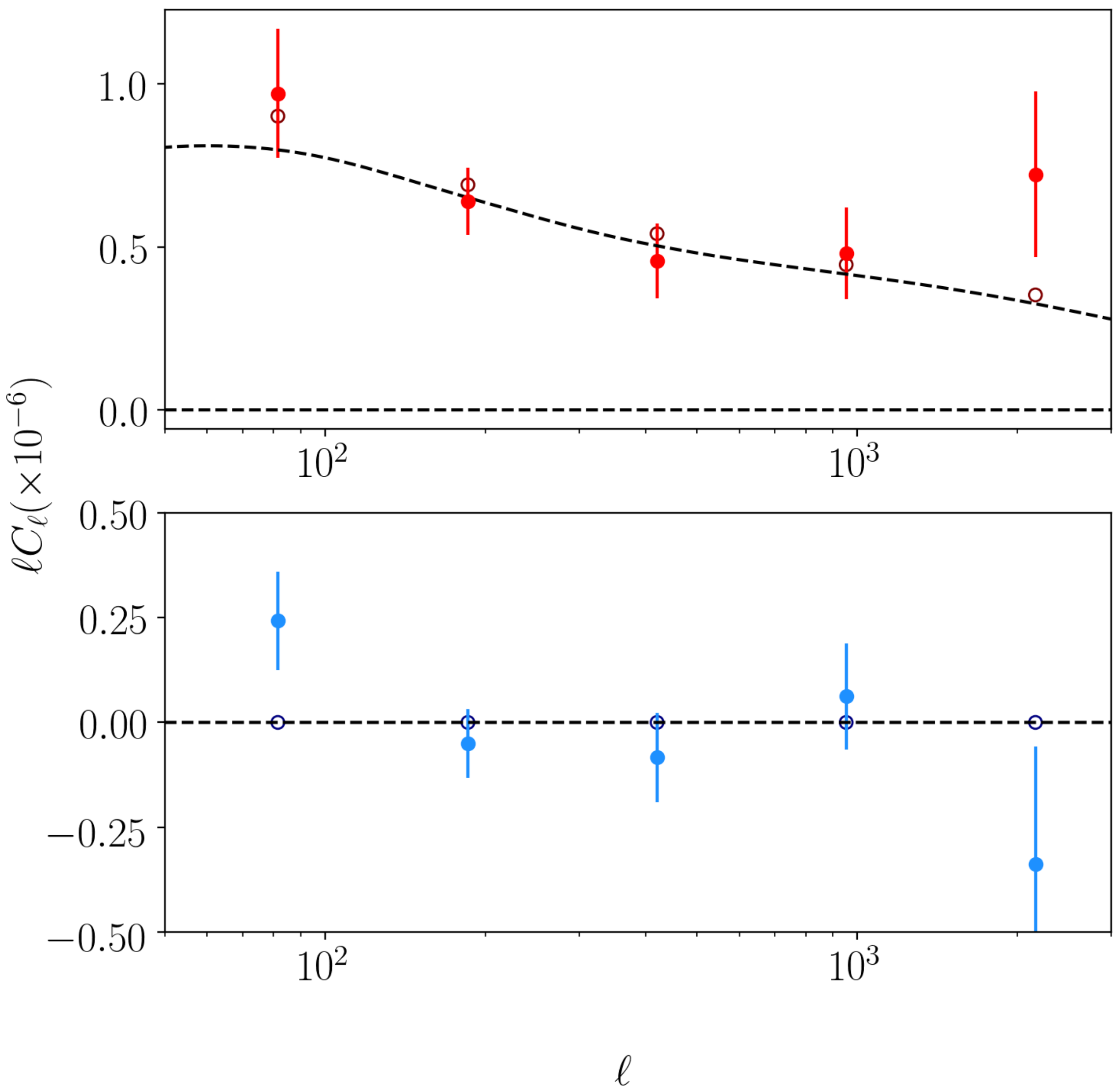


Figure 3.10: Simulated ACT-KiDS cross-spectrum using upcoming ACT data with error bars estimated using the Knox equation and realistic non-white noise spectra. The theoretical cross-correlation power spectrum assumes a *Planck* cosmology with realistic GWL systematics.

| Parameter | Prior 0 | Prior 1 | Prior 2 |
|---|---|---|---|
| m | (0.0,0.02) | (0.0,0.04) | [-0.08,0.08] |
| $\Delta z$ | (0.0,0.027) | (0.0,0.054) | [-0.108,0.108] |
| $A^{\rm IA}$ | (1.06,0.47) | (1.06,0.94) | [-1.18,2.94]] |
| $\Delta S_8$ | 0.05 | 0.07 | 0.1 |

Table 3.3: For simulated ACT data: we investigate the effect of varying systematic priors on the $S_8$ error budget. Here, curved brackets correspond to a Gaussian prior, $(\mu, \sigma)$, of mean $\mu$ and width $\sigma$ and square brackets correspond to a flat prior, $[a, b]$, between $a$ and $b$.

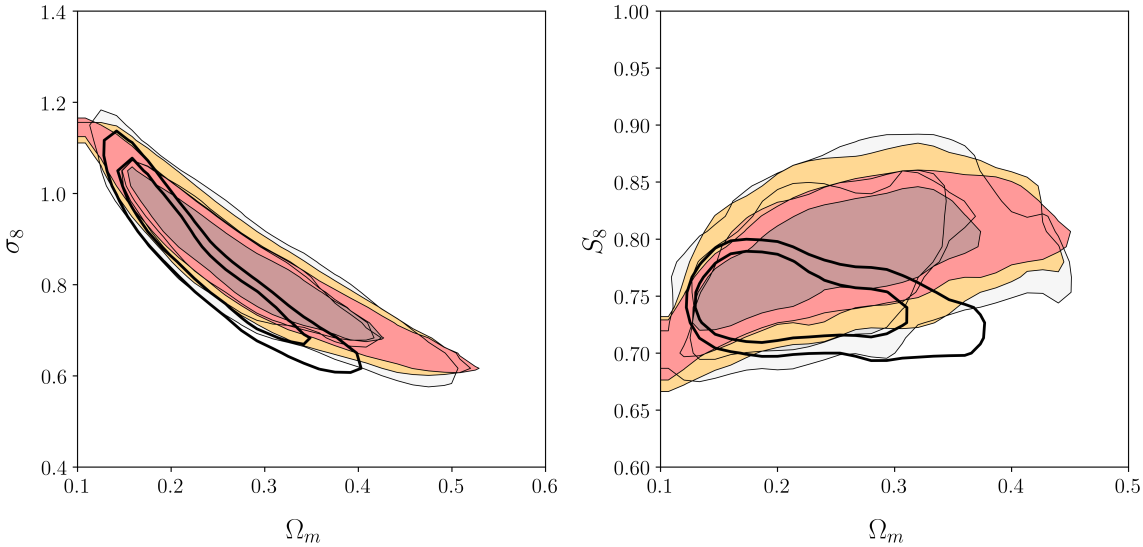


Figure 3.11: Effect of widening priors on GWL systematic parameters. Parameters using the wide flat priors (prior 2) are shown in the grey contours, with the double width Gaussian prior (prior 1) in orange, and the original narrow priors shown in red. For comparison the current measurement for the KV-450 shear signal (Hildebrandt et al., 2018) is over-plotted as the thick black line.

input model parameters. We find that widening our priors to flat priors doubles the uncertainty on the $S_8$ parameter, as shown in Fig. 3.11.

## 3.6 Discussion

In this chapter we have measured the cross-correlation power spectrum between the ACT CMB lensing and KiDS GWL data sets. The GWL shear maps are created from shape measurements of galaxies in the redshift range of 0.1 to 1.2. The cross-correlation is detected with a significance of $4.7\sigma$. We perform two null tests on the measurement, by measuring the B-mode component of the cross-correlation and by randomly rotating the KiDS galaxies and re-measuring the power spectrum.

From the measured power spectrum we perform amplitude fits to a *Planck* and a KiDS best fit cosmology and find $A_{Planck} = 0.78 \pm 0.14$ and $A_{\mathrm{KV-450}} = 0.87 \pm 0.16$ respectively. The amplitude inferred against a *Planck* cosmology is consistent with previous cross-correlation analyses using other data sets. From these fits we find the data favours a KiDS cosmology, although at low significance. We also show that including a non-zero intrinsic alignment amplitude makes the data agree more with both models. We extend this by performing a five parameter fit to the data, fitting for the cosmological parameters $\Omega_m$ and $\sigma_8$ and the GWL systematic bias parameters $m$, $\Delta z$ and $A_{\rm IA}$. We find that our constraints on the GWL systematic parameters are dominated by priors we impose, given the signal-to-noise of our measurement of the cross-correlation. We find $S_8 = 0.75 \pm 0.08$, which is consistent with the value reported in the KV-450 shear analysis (Hildebrandt et al., 2018). *Note: these results and conclusions will be updated when the KiDS data are unblinded: parameters can be expected to shift by order 1$\sigma$.*

Finally we show that with the next data set from ACT – which has improved CMB noise levels – we will be able to improve our constraints on the $S_8$ parameter, while investigating GWL systematics parameters.

Moving into the era of SO and LSST we will be able to use the cross-correlation to investigate the nature of dark energy and the mass of neutrino particles. These multi-probe analyses will also produce a robust test of systematic biases present in the data.

# Chapter 4

# Mass Calibration of Sunyaev-Zel'dovich Selected Clusters from the Atacama Cosmology Telescope with the Kilo Degree Survey

## 4.1 Introduction

The locations of galaxy clusters trace the position of peaks in the large scale matter distribution. As a result, their properties – including number density, masses, baryon content and evolution – contain information about the growth of structure in the Universe and can constrain quantities such as the amplitude of matter fluctuations, $\sigma_8$, the matter density, $\Omega_m$, the sum of neutrino masses and the dark energy equation of state (e.g., Kaiser, 1986; Peebles et al., 1989; Kaiser, 1991; Barbosa et al., 1996; Komatsu & Kitayama, 1999; Holder et al., 2001; Komatsu & Seljak, 2002; Battye

& Weller, 2003; Voit, 2005). The key statistic is their number density as a function of mass and redshift, $N(M, z)$. However, in practice we cannot measure the mass directly and instead infer it from some observable quantity that correlates with mass (see e.g., Allen et al., 2011, for a review).

Clusters can be observed in the X-ray, optical, infrared and millimetre regimes. They emit X-rays from the hot intra-cluster gas, with the luminosity scaling with mass. In the optical and infrared, the cluster richness and stellar luminosity of the galaxies within the cluster also correlate with mass. At millimeter wavelengths clusters produce the thermal Sunyaev-Zeldovich effect (SZ) (Zel'dovich et al., 1969; Sunyaev & Zel'dovich, 1972; Birkinshaw et al., 1984), where CMB photons are inverse Compton scattered off electrons in the hot cluster gas. In this case, the mass observable is the volume integrated intra-cluster medium (ICM) pressure, measured with the Compton–$y$ parameter. The low dependence of the SZ effect on redshift allows clusters to be detected at larger distances than with other observations.

For all of these detection methods, the ability to use clusters for cosmology is currently limited by the uncertainty in the mass-observable scaling relations, which need to be calibrated (see e.g Vikhlinin et al., 2009; Rozo et al., 2010; Vanderlinde et al., 2010; Sehgal et al., 2011; Benson et al., 2013; Hasselfield et al., 2013; Mantz et al., 2014, 2015; Hoekstra et al., 2015; Planck Collaboration, 2016; de Haan et al., 2016). Weak gravitational lensing provides a tool for this, as it is sensitive to the entire mass of the cluster, both dark and baryonic, and does not depend on its dynamical state. Previous estimates of weak-lensing masses have been made for SZ-selected clusters from the South Pole Telescope (SPT) (McInnes et al., 2009; High et al., 2012; Schrabback et al., 2018; Dietrich et al., 2019; Stern et al., 2019), the Atacama Cosmology Telescope (ACT) (Miyatake et al., 2013; Jee et al., 2014; Battaglia et al., 2016; Miyatake et al., 2019) and the *Planck* satellite (von der Linden et al., 2014; Hoekstra et al., 2015; Penna-Lima et al., 2017; Sereno et al., 2017; Medezinski et al., 2018).

Many of these studies have focused on measuring the hydrostatic mass bias, which quantifies the cluster mass fraction left unaccounted for in the $y-M$ scaling relation. This scaling relation uses models for the gas and density profiles calibrated on X-ray data, which assumes that clusters are in hydrostatic equilibrium. This bias is defined as

$$(1-b) = \frac{M_{\mathrm{SZ}}}{M_{\mathrm{WL}}}\,, \tag{4.1}$$

where $M_{\mathrm{SZ}}$ is the mass derived from the SZ Compton-$y$ observable, assuming the X-ray calibrated models, and $M_{\mathrm{WL}}$ is the mass measured using weak gravitational lensing which we take to be the 'true' mass. This bias can also capture other sources of systematics, bias and physical processes which are not yet fully understood within the framework used to model clusters (Pratt et al., 2019). There have been investigations into whether $(1-b)$ may depend on mass or redshift (Henson et al., 2017; Remazeilles et al., 2019); current data are not yet conclusive given the uncertainties.

Recent estimates of this bias from SZ clusters detected using *Planck* and ACT are reported in Medezinski et al. (2018) and Miyatake et al. (2019), with alternative parameterisations of the mass scaling reported from SPT in Bocquet et al. (2019). These latest estimates are consistent with the prediction from *Planck* CMB anisotropy measurements that $(1-b)$ should be of order 0.6 if the ΛCDM model is correct (Planck Collaboration, 2018), given the SZ clusters observed by *Planck*. In this chapter we estimate this bias parameter for a new cluster sample from ACT using weak lensing data from the Kilo Degree Survey (KiDS). The ACT experiment has been used to construct a sample of more than 1400 confirmed clusters over a 14,000 deg$^2$ region, measured during the 2013-16 observing seasons (Hilton & ACT Collaboration, in prep.). This catalogue will be extended using deeper observations over the same region until 2021. KiDS provides 1000 deg$^2$ of weak lensing data in the area covered by ACT; we find 57 SZ-confirmed clusters in this region. In this chapter we estimate the stacked masses of these clusters, and the bias parameter. This allows us to probe the lower end of the SZ cluster mass range with a larger sample size than was previously available. This study also provides a means to cross-check consistency of data from different weak lensing surveys which also have survey area in common with ACT.

The outline of this chapter is as follows. We summarise the data and observable quantities in section 4.2, then show the mass and bias estimates in sections 4.3 and 4.4 for the stacked clusters as well as the highest signal-to-noise individual clusters. We also describe tests of systematic effects and analysis choices. We conclude in section 4.5.

## 4.2 Data and Observables

### 4.2.1 The Atacama Cosmology Telescope SZ-selected Cluster Sample

We use the ACT cluster catalogue described in Hilton & ACT Collaboration (in prep.), based on the maps described in Aiola et al. (in prep.) and Naess & ACT Collaboration (in prep.), which we summarise briefly here. The Atacama Cosmology Telescope Polarimeter (ACTPol) observed four deep regions of the sky with a single detector array (PA1) at 150 GHz for its first season in 2013 (S13) (Naess et al., 2014), and two wider fields with an additional detector array (PA2) for its second season in 2014 (S14), and with a third array (PA3) with dichroic detectors measuring at 90 GHz and 150 GHz for its third season (S15). In 2016 (S16) a wider field was observed with PA1, PA2 and PA3. Observations have continued since then, but this cluster sample is based on the 2013-16 data.

The cluster catalogue is constructed from coadded S13-16 maps at 90 and 150 GHz formed by combining ACT and *Planck* data, described in Naess & ACT Collaboration

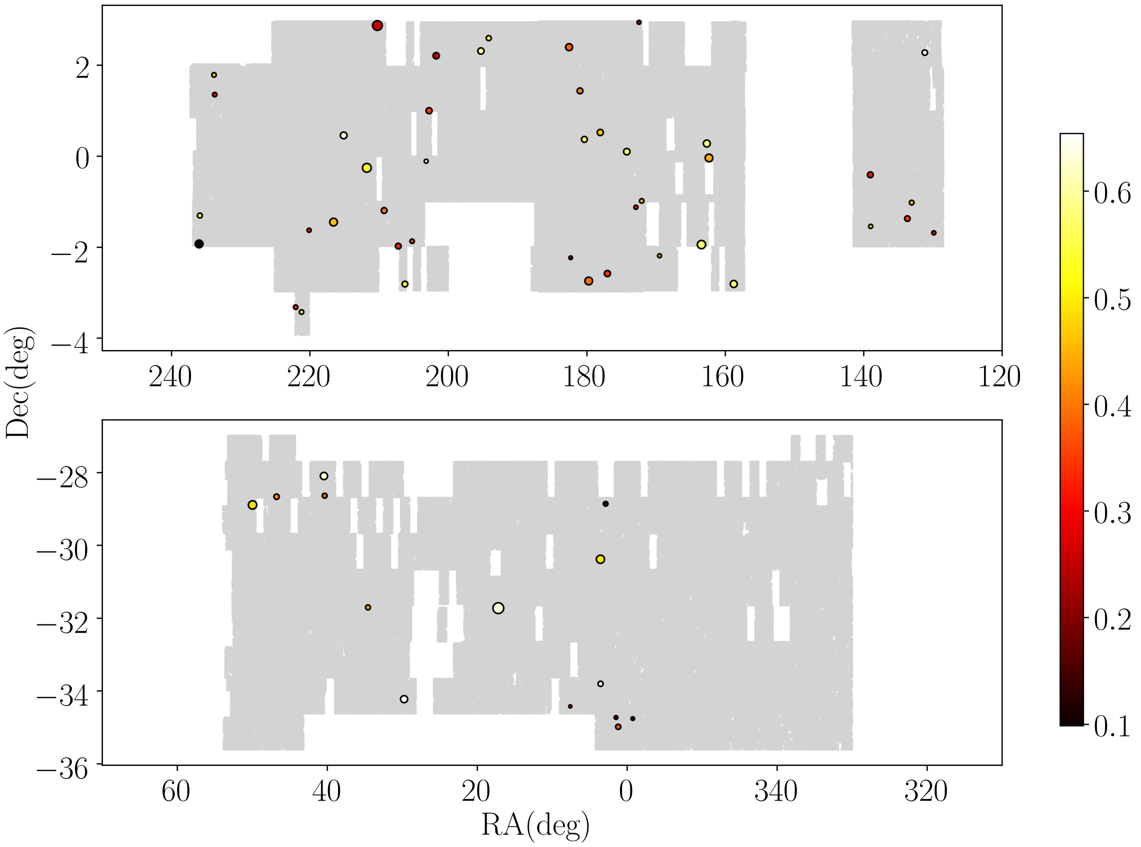


Figure 4.1: KiDS North and South patches, shown in light grey with the 57 ACT cluster positions indicated by each circle. The colour bar corresponds to redshift and the size of each circle scales with the cluster mass estimated from SZ observables.

(in prep.). Clusters are identified using a suite of multi-frequency matched filters (see Hilton & ACT Collaboration, in prep., for details), and confirmed using imaging from the large public surveys SDSS, DECaLS, PS1, PS1IR, KiDS, CS82, HSC, DES and 2dFLenS, from which the cluster redshifts are also determined. In our overlapping region with KiDS data, we find 57 clusters, of which 26 are detected with a signal-to-noise ratio greater than 5. The signal-to-noise of the cluster signal is determined from a single fixed filter scale which simplifies the survey selection function. Their locations are shown in Fig. 4.1, and their redshift distribution in the left panel of Fig. 4.2.

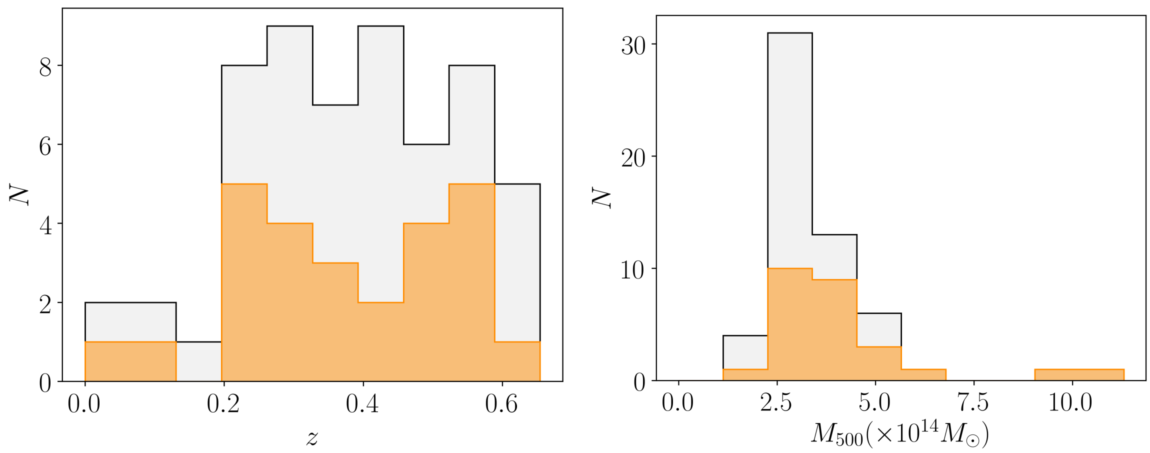


Figure 4.2: Left: The redshift distribution of 57 ACT clusters found in the K-1000 region – the 27 clusters with a signal-to-noise greater than 5 are shown in orange. Right: SZ-derived mass distribution of these clusters, estimated from the SZ observable Compton-$y$ values.

#### 4.2.1.1 SZ-estimated masses

Hilton & ACT Collaboration (in prep.) estimate the Compton-$y$ parameter and associated SZ mass, $M_{\rm SZ}$, for each cluster. We summarise that method here. The Compton-$y$ signal is modelled using the Universal Pressure Profile (Arnaud et al., 2010) which describes the intra-cluster gas pressure, $p$, as a function of radius, $x$, modelled with a generalised NFW profile from Nagai (2006)

$$p(x) = \frac{p_0}{(cx)^\gamma[1+(cx)^\alpha]^{(\beta-\gamma)/\alpha}} \tag{4.2}$$

where $c$ is the concentration parameter and $\{\gamma, \alpha, \beta\}$ describe the slope at different radii. This includes any mass dependence in the profile shape and has been calibrated to X-ray observations of nearby clusters. From these assumptions, following Arnaud et al. (2010), the cluster central Compton parameter, $y$, can be related to the SZ mass via

$$y = 10^{A_0} E(z)^2 \left(\frac{M_{\rm SZ,500}}{M_{\rm piv}}\right)^{1+B_0} Q(M_{\rm SZ,500}, z) f_{\rm rel}(M_{\rm SZ,500}, z)\,, \tag{4.3}$$

where $10^{A_0} = 4.95\times 10^{-5}$ is the normalisation, $E(z)$ is the ratio of the Hubble constant at a redshift $z$ to the present value, $B_0 = 0.08$ is a scaling parameter and $M_{\text{piv}} = 3 \times 10^{14}\text{M}_\odot$ is a mass normalisation parameter. The cluster-filter scale mismatch function $Q$ accounts for the discrepancy between the size of a cluster with a different mass and redshift to the reference model used to define the matched filter, which includes the effects of the beam.

The signal we observe due to the SZ effect is a change in radiation intensity which can be expressed in terms of CMB temperature by

$$\frac{\Delta T(\theta)}{T_{\text{CMB}}} = f_{\text{SZ}}\, y(\theta)\,. \tag{4.4}$$

In the non-relativistic limit, $f_{\text{SZ}}$ only depends on the observed radiation frequency, but here a correction factor $f_{\text{rel}}$ is applied to include relativistic effects for gas temperature, as determined in Itoh et al. (1998).

To obtain the cluster mass, the intrinsic scatter $\sigma_c$ in the $y - M$ scaling relation must be accounted for. Hilton & ACT Collaboration (in prep.) assume a log normal scatter of $\sigma_c = 0.2$, since this level of scatter is consistent with both numerical simulations (Bode et al., 2012) and dynamical mass measurements of clusters (Sifón et al., 2013). The distribution of SZ derived cluster masses ($M_{\text{SZ}}$) for our sample is shown in the right panel of Fig. 4.2.

### 4.2.2 Weak Gravitational Lensing from the Kilo Degree Survey

KiDS is an ongoing optical survey utilising the OmegaCAM CCD mosaic camera on the VLT Survey Telescope in Chile (de Jong et al., 2015, 2017). For this analysis we are using the K-1000 data set, first presented in Kuijken et al. (2019), which includes 30 million galaxies across 2 patches of sky based around the GAMA spectroscopic survey. K-1000 was observed in 4 bands, $\{u, g, r, i\}$, and has an effective number density of 7.2 arcminutes$^{-2}$. The seeing conditions are best in the $r$-band, which has a magnitude limit of 24.9, thus galaxy shape measurements were made from $r$-band images using lensfit (Miller et al., 2013) as described in Fenech Conti et al. (2017). The variance of the ellipticities is 0.28. The source redshift distribution is determined from direct calibration of the KiDS photometric redshifts using deep spectroscopic data and overlapping infrared data from VIKING which is detailed in section 3.2 of Hildebrandt et al. (2018). The weak lensing data from KiDS can be used up to a redshift of 1.2. For more technical details on the survey see Kuijken et al. (2019).

#### 4.2.2.1 The Excess Surface Density

We summarise the formalism for estimating the weak gravitational lensing signal around either a single cluster or a stack of clusters, following Bartelmann & Schneider (2001). Considering an isolated cluster, weak lensing introduces a systematic tangential alignment of the images of the source galaxies relative to the lens. We use the average tangential distortion, $\gamma_t$, to quantify the lensing signal. This is calculated from the two components of shear, $[\gamma_1, \gamma_2]$,

$$\begin{pmatrix} \gamma_t \\ \gamma_\times \end{pmatrix} = \begin{pmatrix} -\cos 2\phi & -\sin 2\phi \\ \sin 2\phi & -\cos 2\phi \end{pmatrix} \begin{pmatrix} \gamma_1 \\ \gamma_2 \end{pmatrix}, \tag{4.5}$$

where $\phi$ is the angle measured from the positive x–axis to a given source galaxy relative the centre of the lens. The 45°–rotational shear, $\gamma_\times$, is a useful control statistic that should be consistent with zero if the data has produced a signal solely caused by gravitational lensing.

Since the tangential distortion we observe is due to intervening matter along the line of sight, the average $\gamma_t$ of source galaxies at a projected separation $R$ from the cluster lens can be expressed in terms of the differential projected surface mass density,

$\Delta\Sigma_t$,

$$\langle\gamma_t\rangle(R) = \frac{\Delta\Sigma(R)}{\Sigma_c}\,, \tag{4.6}$$

where $\Sigma_c$ is the comoving critical surface density given by

$$\Sigma_c = \frac{c^2}{4\pi G}\frac{\chi_s}{(\chi_s - \chi_l)\chi_l(1+z_l)}\,. \tag{4.7}$$

Here $\chi$ is the comoving distance to the lens $l$ and the source $s$ and $z_l$ is the lens redshift. The differential projected surface mass density, (which from now on we will refer to as excess surface density or ESD) is defined as

$$\Delta\Sigma_t(R) \equiv \overline{\Sigma}(< R) - \Sigma(R)\,, \tag{4.8}$$

with the average mass density within a radius $R$ given by

$$\overline{\Sigma}(< R) \equiv \frac{2}{R^2}\int_0^R R'\Sigma(R')dR'\,. \tag{4.9}$$

Equation 4.6 can be generalised for broad lens and source redshift distributions, $p_l$ and $p_s$ to give

$$\langle\gamma_t\rangle(R) = \int_0^\infty dz\, p_l(z)\Delta\Sigma(R,z)\int_0^\infty dz'\, p_s(z')\frac{1}{\Sigma_c(z,z')}\,. \tag{4.10}$$

For a narrow lens and source redshift distribution, $p_l = \delta_D(z - z_l)$ and $p_s(z') = \delta_D(z' - z_s)$, so that the above equation reduces to equation 4.6. $\Delta\Sigma(R, z_l)$ cannot be solved for in closed form, but for a narrow lens redshift distribution, averaging over a background source redshift distribution, $p_s(z)$, we find

$$\Delta\Sigma(R, z_l) \approx \langle\gamma_t\rangle(R)\Big[\int_0^\infty dz' p_s(z')\frac{1}{\Sigma_c(z_l, z')}\Big]^{-1}\,. \tag{4.11}$$

This can be written as

$$\Delta\Sigma_t(R, z_l) = \frac{\gamma_t(\theta)}{\overline{\Sigma_c^{-1}}}\,, \tag{4.12}$$

where, for a given data set, the average inverse critical surface density, $\overline{\Sigma_c^{-1}}$, is defined as

$$\begin{aligned}\overline{\Sigma_c^{-1}} &\equiv \int_{z_l}^{\infty} dz_s p_s(z_s) \Sigma_c^{-1}(z_l, z_s) \\ &= \frac{4\pi G(1+z_l)\chi_l}{c^2} \int_0^{\infty} dz_s\, p_s(z_s) \Big[1 - \frac{\chi_l}{\chi_s}\Big].\end{aligned} \tag{4.13}$$

The above equation leads to the following estimator for a stack of clusters:

$$\Delta\Sigma_t(R) = \frac{1}{(1+\overline{m}(R))} \frac{\sum_i \sum_j w_i \overline{\Sigma_{c,j}^{-1}} \gamma_{t,ij}(R)}{\sum_i \sum_j w_i \left[\overline{\Sigma_{c,j}^{-1}}\right]^2}\,, \tag{4.14}$$

where the sum is over sources, $i$, in radial bin $R$ around cluster $j$. Each source is inverse variance weighted by, $w_i$, derived from the shape measurement. The excess surface density can be estimated for a single cluster by removing the sum over clusters in equation 4.14. An additional calibration prefactor is also included which corrects for the multiplicative bias, $m_i$, in the shape measurement,

$$\overline{m}(R) = \frac{\sum_i w_i' m_i}{\sum_i w_i'}\,, \tag{4.15}$$

where

$$w_i' = w_s \frac{(\chi_l - \chi_s)}{\chi_s}\,. \tag{4.16}$$

We estimate the ESD signal for individual clusters and for the stacked signal of all clusters. For the stacked ESD measurement we estimate the covariance matrix by bootstrapping over KiDS tiles used in the measurement. There are limitations with this method since we do not have a very large number of clusters and therefore a limited number of KiDS tiles – this could lead to an underestimate of the errors at larger scales. A more sophisticated approach for future analyses would be to use an analytic covariance which accounts for more than the Gaussian component (for example, Dvornik et al., 2018).

When considering measurements around individual clusters, we compute the variance analytically which includes shape noise only. To correctly estimate our error budget we should also include terms that account for intrinsic variations in the cluster mass profiles – such as halo triaxiality and the intrinsic scatter of the concentration-mass relation – as well as uncorrelated large scale structure along the line-of-sight. However, shape noise is expected to be the dominant component and since the individual cluster analysis is an exploratory study, we defer the development of a more complete estimate of the variance to a future study.

## 4.3 Results: Individual Clusters

### 4.3.1 Excess Surface Density

We initially measure the ESD, $\Delta\Sigma_t$, for each of the 26 clusters in our sample with S/N $> 5$, detailed in table 4.1. The highest signal-to-noise SZ detected clusters are shown in Figure 4.3 together with their corresponding optical images from KiDS.

We consider two different cluster centre definitions: the peak of the SZ emission and the Brightest Cluster Galaxy (BCG), which has been shown to be the best tracer of the cluster centre (George et al., 2012). The SZ centre is not expected to trace the centre particularly well since it is limited by the size of the beam which is 1.4 arcmin for ACT. We also anticipate that most clusters are not relaxed and therefore the gas is not predicted to trace the centre of the dark matter halo particularly well.

We find the BCG for each cluster by selecting KiDS galaxies found inside a cylinder, centred on the SZ centre, with a length $\Delta z = 2 \times 0.04(1 + z_l)$ and a diameter $D = 2 \times 1.4$ arcmin. The length of the cylinder is defined to be twice the length of the uncertainty on the photometric redshift of the KiDS galaxies, and the diameter

| Name | SZ RA | SZ Dec | BCG RA | BCG Dec | $z$ | SNR | $M_{500}^{\rm SZ}[\times10^{14}{\rm M}_\odot]$ | $M_{500}^{\rm WL}[\times10^{14}{\rm M}_\odot]$ |
|---|---|---|---|---|---|---|---|---|
| ACT-CL J0004.7-3459 | 00:04:47.90 | -34:59:09.19 | 00:04:48.68 | -34:59:34.21 | 0.23 | 5.73 | $2.59^{+0.64}_{-0.51}$ | $5.69^{+1.40}_{-1.38}$ |
| ACT-CL J0005.9-3443 | 00:05:58.73 | -34:43:42.11 | 00:05:59.76 | -34:43:17.53 | 0.11 | 5.83 | $2.13^{+0.67}_{-0.51}$ | $4.55^{+1.55}_{-1.51}$ |
| ACT-CL J0014.2-3022 | 00:14:17.12 | -30:22:54.26 | 00:14:20.76 | -30:23:57.61 | 0.31 | 10.99 | $9.56^{+1.96}_{-1.63}$ | $12.94^{+2.45}_{-2.40}$ |
| ACT-CL J0159.0-3413 | 01:59:00.29 | -34:13:27.70 | 01:59:03.99 | -34:13:04.25 | 0.41 | 7.38 | $6.71^{+1.42}_{-1.17}$ | $2.98^{+2.17}_{-1.64}$ |
| ACT-CL J0839.5-0141 | 08:39:30.01 | -01:41:02.06 | 08:39:31.58 | -01:40:23.94 | 0.27 | 5.44 | $2.76^{+0.77}_{-0.60}$ | $3.17^{+1.51}_{-1.41}$ |
| ACT-CL J0916.1-0024 | 09:16:10.30 | -00:24:27.86 | 09:16:08.94 | -00:24:22.64 | 0.32 | 5.79 | $3.64^{+0.85}_{-0.69}$ | $9.05^{+2.87}_{-2.90}$ |
| ACT-CL J1035.1-0248 | 10:35:06.54 | -02:48:25.10 | 10:35:07.00 | -02:48:36.68 | 0.58 | 6.12 | $3.46^{+0.72}_{-0.60}$ | $3.90^{+3.53}_{-2.62}$ |
| ACT-CL J1053.7-0156 | 10:53:45.40 | -01:56:29.14 | 10:53:45.85 | -01:56:30.40 | 0.57 | 5.54 | $3.06^{+0.68}_{-0.56}$ | $0.32^{+1.00}_{-0.32}$ |
| ACT-CL J1129.8+0256 | 11:29:50.57 | 02:56:37.45 | 11:29:50.93 | 02:56:26.87 | 0.23 | 5.22 | $2.37^{+0.69}_{-0.53}$ | $4.16^{+2.39}_{-1.87}$ |
| ACT-CL J1136.9+0006 | 11:36:54.63 | 00:06:03.20 | 11:36:57.80 | 00:05:00.04 | 0.58 | 9.90 | $5.26^{+0.96}_{-0.81}$ | $10.03^{+6.21}_{-5.28}$ |
| ACT-CL J1148.1-0234 | 11:48:06.79 | -02:34:38.93 | 11:48:06.93 | -02:34:20.22 | 0.34 | 5.98 | $3.50^{+0.80}_{-0.65}$ | $10.30^{+2.22}_{-2.03}$ |
| ACT-CL J1152.2+0031 | 11:52:13.74 | 00:31:21.24 | 11:52:14.09 | 00:31:27.53 | 0.46 | 5.74 | $3.49^{+0.76}_{-0.63}$ | $7.02^{+3.57}_{-3.32}$ |
| ACT-CL J1203.9+0126 | 12:03:57.48 | 01:26:11.67 | 12:03:57.89 | 01:25:30.84 | 0.41 | 6.38 | $3.75^{+0.80}_{-0.66}$ | $4.45^{+2.08}_{-2.00}$ |
| ACT-CL J1301.1+0218 | 13:01:11.58 | 02:18:44.86 | 13:01:13.51 | 02:18:51.47 | 0.59 | 5.72 | $3.57^{+0.76}_{-0.63}$ | $18.74^{+5.71}_{-5.12}$ |
| ACT-CL J1327.0+0212 | 13:27:02.31 | 02:12:33.34 | 13:27:01.02 | 02:12:19.61 | 0.26 | 8.54 | $5.07^{+1.11}_{-0.91}$ | $8.32^{+1.78}_{-1.68}$ |
| ACT-CL J1331.1+0100 | 13:31:10.94 | 01:00:04.38 | 13:31:11.44 | 01:00:03.20 | 0.35 | 8.33 | $4.68^{+0.96}_{-0.80}$ | $7.25^{+1.71}_{-1.57}$ |
| ACT-CL J1345.0-0248 | 13:45:05.83 | -02:48:33.88 | 13:45:06.02 | -02:48:42.75 | 0.52 | 7.12 | $4.23^{+0.85}_{-0.71}$ | $14.84^{+5.30}_{-5.15}$ |
| ACT-CL J1348.9-0158 | 13:48:57.43 | -01:58:29.76 | 13:48:56.62 | -01:57:59.33 | 0.33 | 5.22 | $2.98^{+0.72}_{-0.58}$ | $0.50^{+0.87}_{-0.41}$ |
| ACT-CL J1401.0+0252 | 14:01:01.81 | 02:52:24.91 | 14:01:02.07 | 02:52:42.66 | 0.25 | 21.72 | $11.30^{+2.32}_{-1.92}$ | $19.17^{+3.11}_{-2.90}$ |
| ACT-CL J1407.1-0015 | 14:07:07.29 | -00:15:16.48 | 14:07:07.04 | -0:15:04.91 | 0.54 | 5.81 | $3.47^{+0.75}_{-0.62}$ | $5.99^{+5.35}_{-3.99}$ |
| ACT-CL J1426.3-0126 | 14:26:22.23 | -01:26:50.41 | 14:26:24.25 | -01:26:57.11 | 0.46 | 5.73 | $3.47^{+0.77}_{-0.63}$ | $19.12^{+3.10}_{-2.86}$ |
| ACT-CL J1440.4-0137 | 14:40:29.93 | -01:37:31.10 | 14:40:31.40 | -01:37:32.25 | 0.32 | 5.42 | $2.92^{+0.74}_{-0.59}$ | $7.20^{+2.61}_{-2.68}$ |
| ACT-CL J1535.4+0147 | 15:35:26.42 | 01:47:17.72 | 15:35:25.27 | 01:46:25.90 | 0.47 | 6.19 | $3.24^{+0.71}_{-0.58}$ | $1.64^{+1.64}_{-1.16}$ |
| ACT-CL J1543.5-0118 | 15:43:35.57 | -01:18:10.94 | 15:43:34.49 | -01:18:27.78 | 0.55 | 5.19 | $3.25^{+0.72}_{-0.59}$ | $28.99^{+9.65}_{-9.81}$ |
| ACT-CL J2347.8-3535 | 23:47:50.32 | -35:35:16.02 | 23:47:48.78 | -35:35:8.40 | 0.26 | 5.72 | $2.35^{+0.56}_{-0.45}$ | $4.16^{+2.17}_{-1.94}$ |
| ACT-CL J2357.0-3445 | 23:57:01.57 | -34:45:31.93 | 23:57:02.32 | -34:45:20.19 | 0.05 | 5.36 | $2.50^{+0.90}_{-0.66}$ | $0.98^{+0.62}_{-0.55}$ |

Table 4.1: The 26 SZ-detected clusters in our sample with $S/N > 5$. The far right column gives the cluster masses estimated by fitting an NFW profile to the individual excess surface density (ESD).

is defined based on the size of the ACT beam. From these galaxies the brightest one is chosen. We then confirm the BCG locations by eye, using public imaging from KiDS, DECALS and HSC. The BCG and SZ centres are listed for a subset of clusters in table 4.1. We use the BCG definition of the centre to measure the ESD around individual clusters.

### 4.3.2 Estimated Masses

We estimate the mass of each cluster, $M_{\rm WL}$, by assuming an NFW density profile (Navarro et al., 1997) and calculating the expected ESD using Wright & Brainerd (2000), summarised here. The NFW profile is given by

$$\rho(r) = \frac{\delta_c \rho_c}{(r/r_s)(1+r/r_s)^2}\,, \tag{4.17}$$

where the characteristic overdensity, $\delta_c$, is related to the NFW concentration parameter, $c$ via

$$\delta_c = \frac{500}{c}\frac{c^3}{[\ln(1+c) - c/(1+c)]}\,. \tag{4.18}$$

In equation 4.17, the scale radius, $r_s = r_{500}/c$, is the cluster's characteristic radius and $r_{500}$ is the radius within which the density is 500 times the critical density, $\rho_c$. We use the $r_{500}$ radius to be consistent with the SZ measurements which also use this definition. The mass within a radius of $r_{500}$, is given by

$$M_{500} \equiv M(r_{500}) = \frac{800\pi}{3}\rho_c r_{500}^3\,. \tag{4.19}$$

The surface mass density, $\Sigma(R)$, as a function of radius for a spherically symmetric lens with mass density $\rho(R,z)$, such as an NFW halo, is given by

$$\Sigma(R) = 2\int_0^\infty \rho(R,z)\mathrm{d}z\,. \tag{4.20}$$

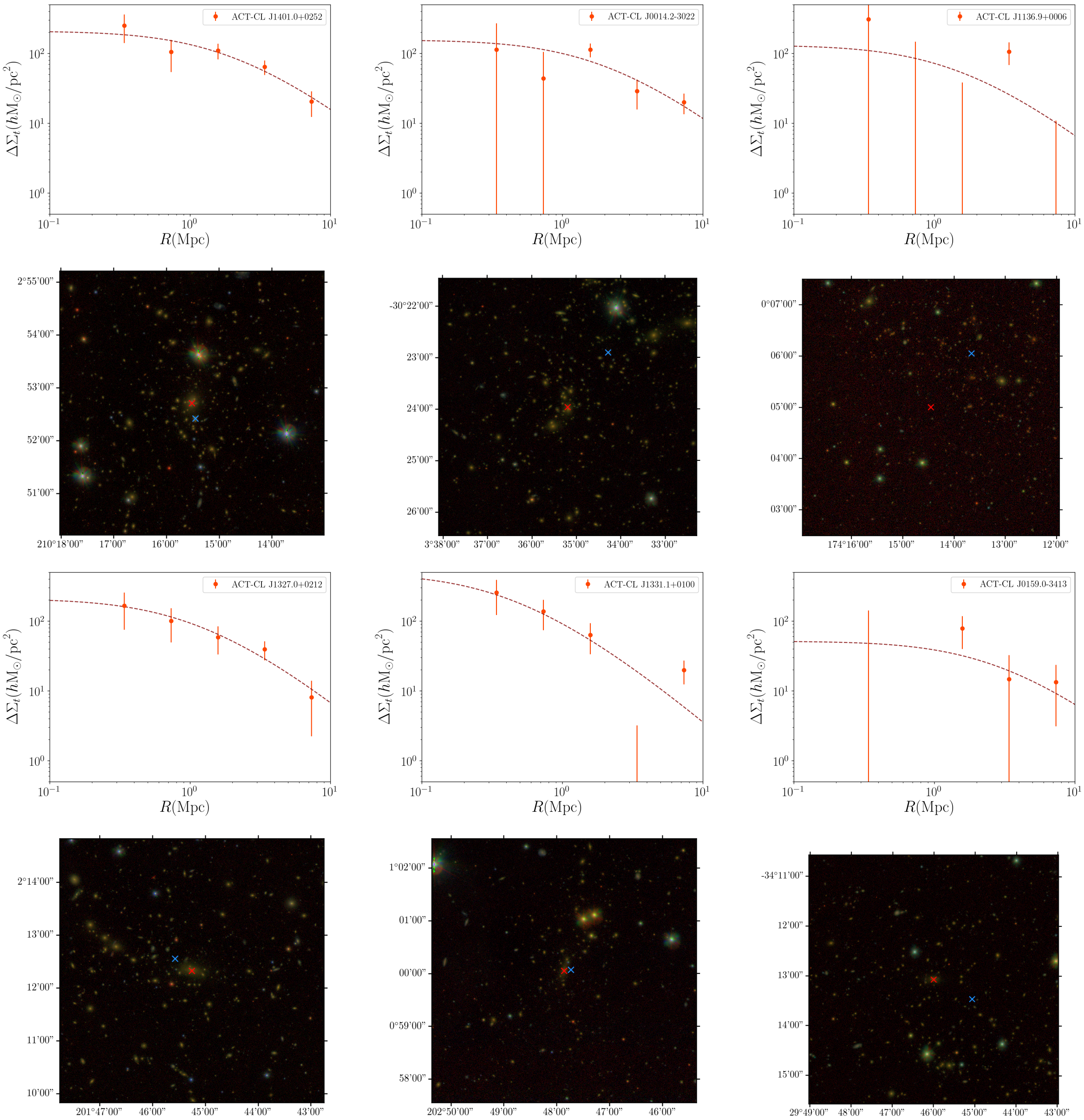


Figure 4.3: The 6 clusters detected with the highest $S/N$ in SZ from ACT: the measured ESDs from KiDS galaxy lensing are shown in the upper panels with fitted NFW profiles, with estimated masses given in table 4.1. The cluster images from KiDS are shown in the lower panels. The red and blue crosses correspond to the BCG and SZ centres respectively.

By integrating equation 4.17 along the line-of-sight, following equation 4.20, we can therefore obtain an equation for the surface density from an NFW halo,

$$\Sigma_{\rm NFW}(x) = \begin{cases} \frac{2r_s\delta_c\rho_c}{x^2-1}\left[1 - \frac{2}{\sqrt{1-x^2}}\,\text{arctanh}(\sqrt{\frac{1-x}{1+x}})\right], & (x < 1) \\ \frac{2r_s\delta_c\rho_c}{3}, & (x = 1) \\ \frac{2r_s\delta_c\rho_c}{x^2-1}\left[1 - \frac{2}{\sqrt{x^2-1}}\arctan\sqrt{\frac{x-1}{1+x}}\right], & (x > 1) \end{cases} \tag{4.21}$$

which has been defined in terms of $x = \frac{R}{r_s}$ for convenience. Therefore the average mass density, defined in equation 4.9 is then given by

$$\overline{\Sigma}_{\rm NFW}(x) = \begin{cases} \frac{4}{x^2}r_s\delta_c\rho_c\left[\frac{2}{\sqrt{1-x^2}}\,\text{arctanh}\sqrt{\frac{1-x}{1+x}} + \ln(\frac{x}{2})\right], & (x < 1) \\ 4r_s\delta_x\rho_c\left[1 + \ln(\frac{1}{2})\right], & (x = 1) \\ \frac{4}{x^2}r_s\delta_c\rho_c\left[\frac{2}{\sqrt{x^2-1}}\arctan\sqrt{\frac{x-1}{1+x}} + \ln(\frac{x}{2})\right], & (x > 1) \end{cases} \tag{4.22}$$

such that the above two equations can be combined to produce an expression for $\Delta\Sigma_{\rm NFW}$ using equation 4.8.

Within this model we fit the mass, $M_{500}^{\rm WL}$, and the concentration, $c$, using the MCMC sampling code emcee (Foreman-Mackey et al., 2013), using wide flat priors. Due to noise and LSS projection the signal can become negative. We address this by allowing for negative masses so that we do not bias the mass high. The resulting NFW models for the clusters detected with the highest SZ signal-to-noise are shown in Fig. 4.3 and detailed in table 4.1. In Fig. 4.4 we show these weak lensing mass estimates together with their SZ inferred masses. We fit a straight line to this relation fixing the y-intercept to zero so that the gradient is equivalent to $(1-b)^{-1}$. We find $(1-b) = 0.60 \pm 0.15$ at 68% confidence level.

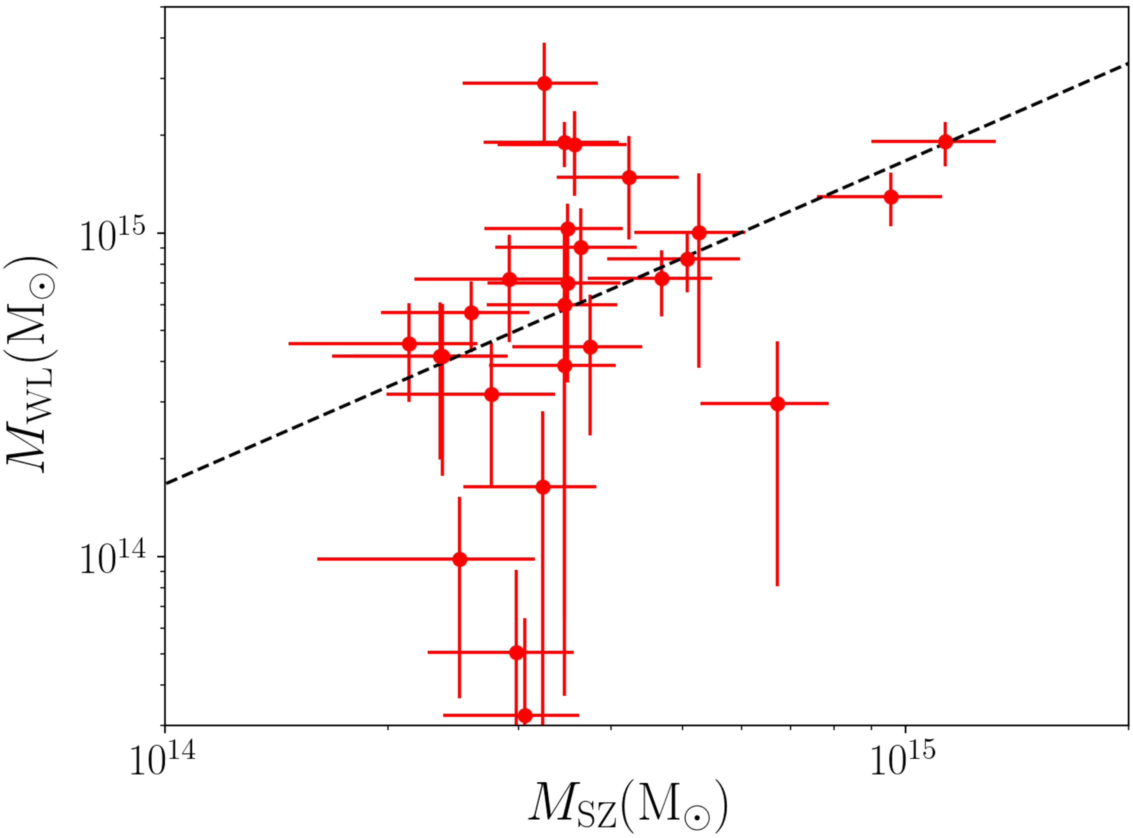


Figure 4.4: Individual cluster masses estimated from the ACT SZ Compton-$y$ parameter ($M_{\rm SZ}$) and from KiDS weak lensing ($M_{\rm WL}$). The black dashed line is the best fitting slope, with y-intercept fixed to zero. The gradient of this line corresponds to the $(1-b)^{-1}$ bias parameter.

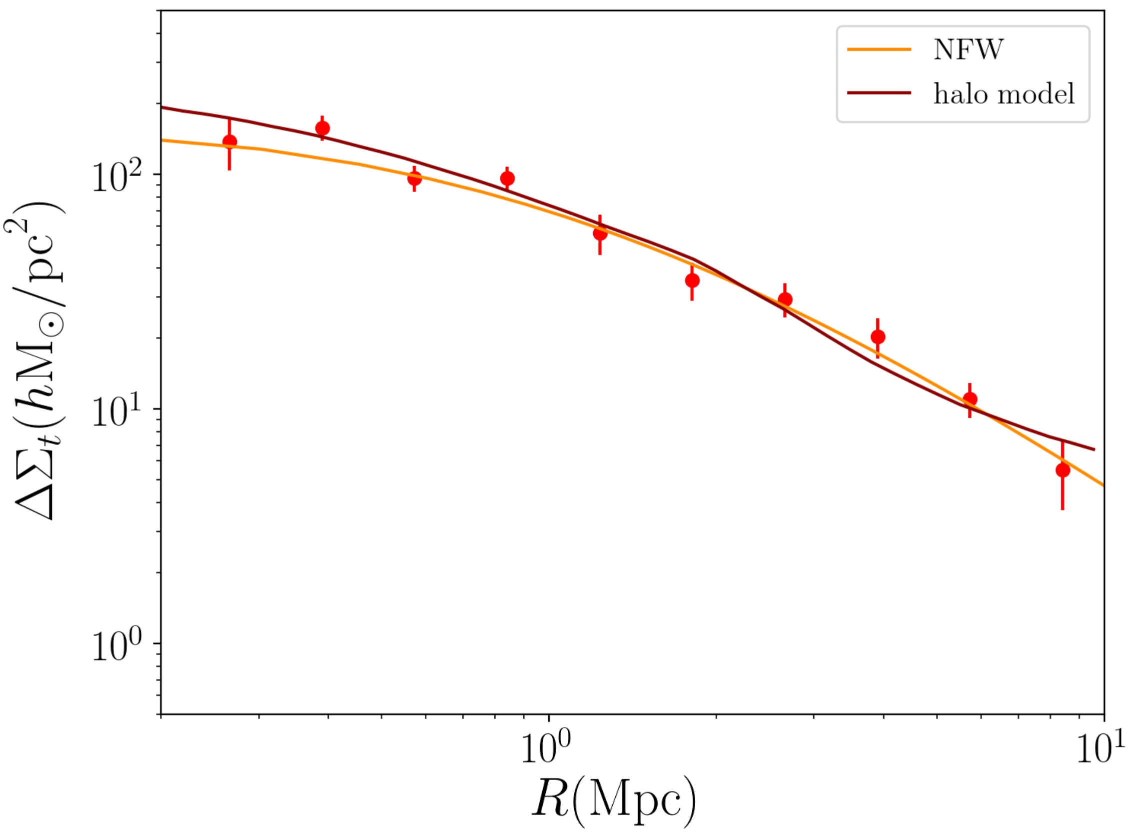


Figure 4.5: The excess surface density profile (ESD, $\Delta\Sigma_t$) as a function of radius $R$ for the complete stack of SZ-detected clusters. The signal is detected at $20\sigma$ significance. The best-fitting model is shown.

## 4.4 Results: Stacked Clusters

We combine all 57 ACT-detected clusters in a single stack, and detect the excess surface density from the KiDS lensing data at $20\sigma$ significance. The stacking process involves averaging over all source galaxies in all clusters in a series of annuli around the clusters, oppose to averaging over source galaxies around each cluster and then taking the average of all clusters. The density profile is shown in Fig. 4.5. The lensing signal is measured at high significance in the range 0.3 Mpc to 10 Mpc from the cluster centres. To test the robustness of this result we investigate the impact of a set of systematic effects, detailed below. These tests are also applicable to the individual cluster ESD measurements.

### 4.4.1 Testing the Measurement

#### 4.4.1.1 Mis-centering of Clusters

The mis-centering of clusters has been reported as one of the largest biases when estimating the cluster mass from weak gravitational lensing (George et al., 2012). If the true cluster centre has not been identified then the amplitude of ESD will be reduced at small radii, corresponding to a lower mass estimate for the cluster.

In our nominal analysis we consider the cluster centre to be defined by the Brightest Cluster Galaxy (BCG), but we also consider the peak of the SZ emission. Measuring the ESD around both these centre candidates, we find at small radii the ESD measured around the BCG has a higher amplitude compared to when measured around the SZ centre, which agrees with our expectation – this is shown in Fig. 4.6.

For this analysis we only use scales greater than 0.3Mpc to infer cluster mass. Both measurements are consistent with each other at the scales larger than this and so we conclude that at the current signal-to-noise of the measurement there is no requirement for further investigation into the effect of miscentering. From here on, we use the BCG as the cluster centre in this study.

#### 4.4.1.2 Source Photometric Redshift Cuts

When measuring the lensing from clusters, it is important not to include any shape measurement values from the cluster members themselves as they will not be lensed by the cluster they inhabit. Due to the uncertainty associated with the photometric redshifts of the source galaxies, there will be some source galaxies that are a cluster member or a foreground galaxy. This leads to a dilution of the lensing signal and therefore a mass estimate which is biased low. To ensure that only sources behind the clusters are being used in the lensing analysis, we test a range of strict cuts on the photometric redshifts of the source galaxies, $z_B$.

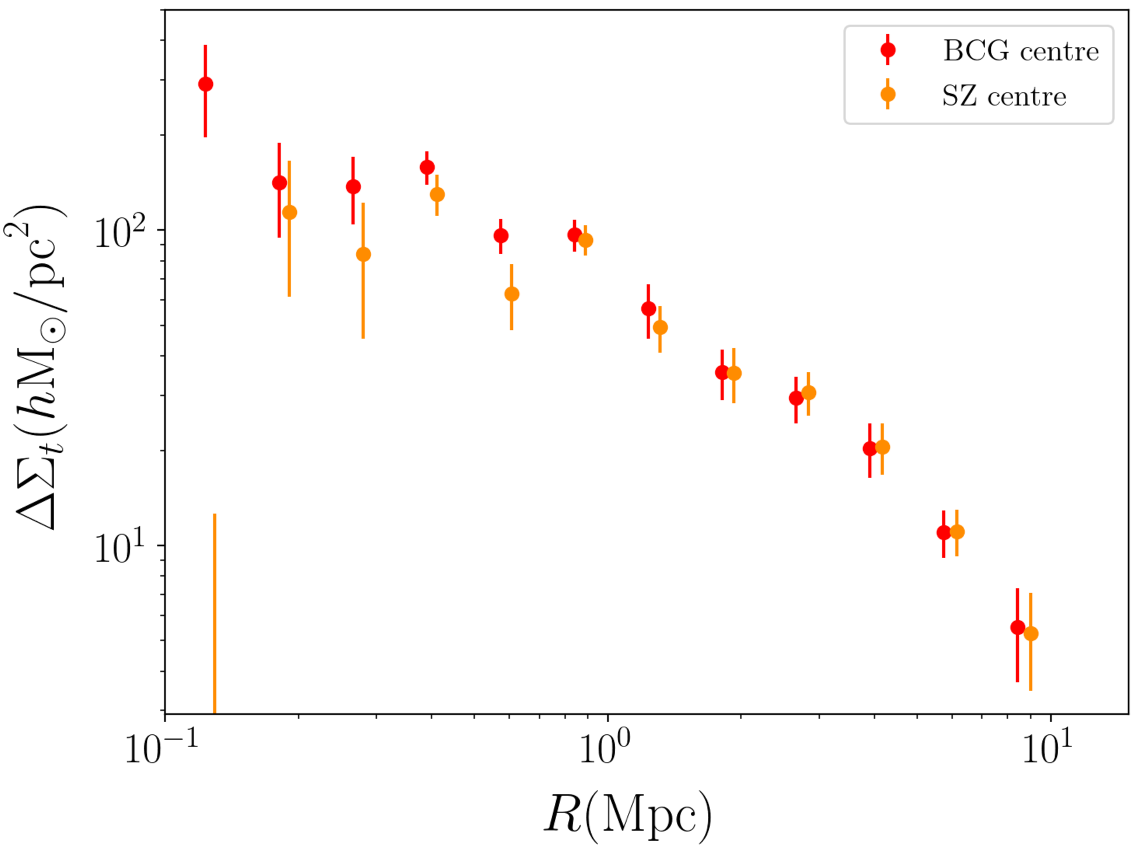


Figure 4.6: Tests of mis-centering: comparison of the ESD measured around the peak in the SZ emission and the BCG. Both measurements are consistent across the scales we use in this analysis, so we conclude that miscentering does not significantly effect our mass estimates.

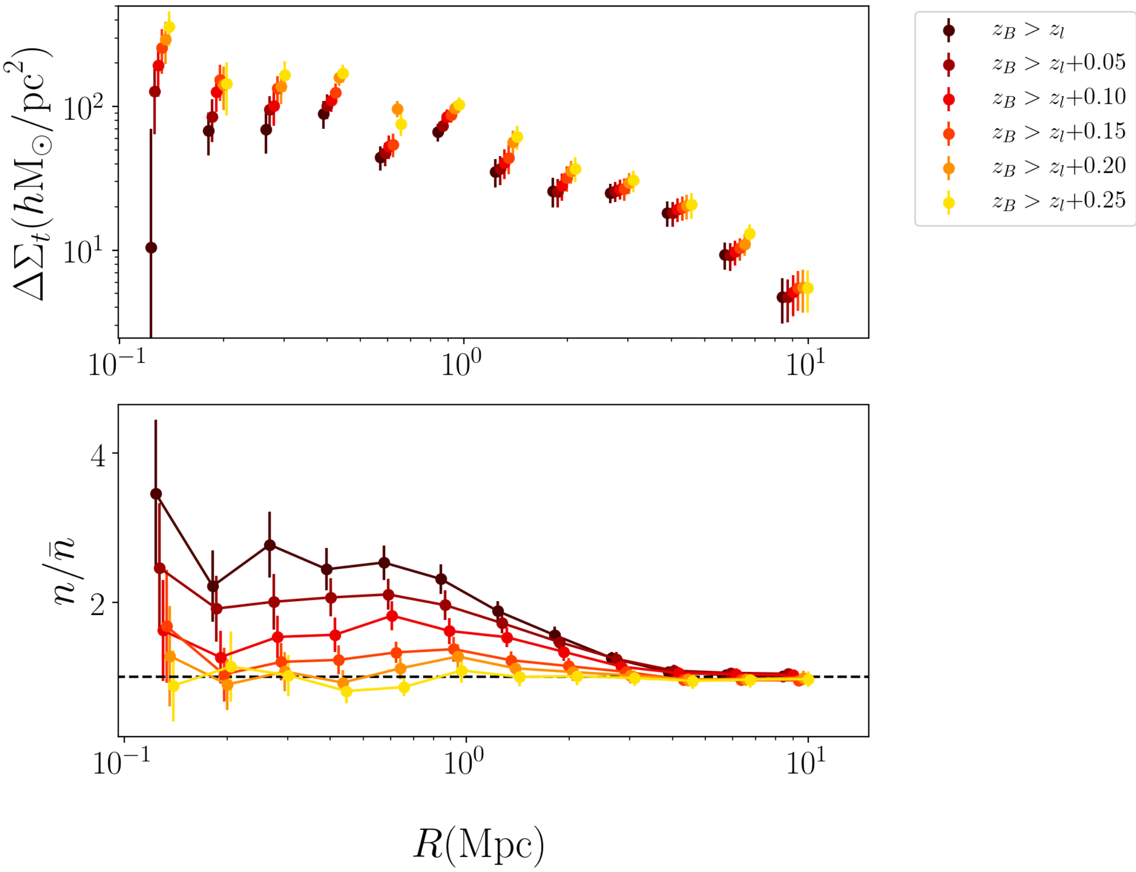


Figure 4.7: Top: The ESD density measured applying different cuts on which source galaxies are included in the lensing measurement based on their photometric redshift. The amplitude of ESD profile is greater for larger cuts on the photometric redshift particularly impacting small radii. Bottom: The average number density of source galaxies around the clusters divided by the the average number density around randomly chosen positions in the KiDS fields. It is clear that when smaller cuts to the photometric redshifts are made more cluster members are included. We conclude a cut of $z_B > z_l + 0.2$ reduces contamination due to cluster members without strongly decreasing the number of source galaxies which are lensed by foreground clusters.

The lensing signal is measured on the stack with each of these cuts applied, as shown in the top panel of Fig. 4.7. This effect is very evident when measuring the number density of source galaxies around clusters compared to random positions, which is shown in the lower panel of Fig. 4.7. We randomly choose 570 positions within the KiDS field and assign redshifts selected from the cluster redshift distribution shown in Fig. 4.2. The average number density in annuli around these random points, $\bar{n}$, is on average the same at all radii for a given photometric redshift cut. It is clear that for a cut of $z_B > z_l + 0.15$ or less, some cluster members are still being included. However, for a cut of $z_B > z_l + 0.2$ and above, the number density of source galaxies is consistent with the number density measured around random points. We therefore select a source galaxy cut of $z_B > z_l + 0.2$ since most cluster galaxies are removed without considerably reducing the number of source galaxies.

#### 4.4.1.3 Null Tests: B-modes and Random Points

To test for systematics in the weak lensing data, we perform two null tests. The cross-component of the ESD, $\Delta\Sigma_\times$, is calculated using equation 4.14 where the cross–component of shear is defined in equation 4.10. This is equivalent to rotating the galaxies by 45 degrees which we expect to remove any tangential alignment. Fig. 4.8 shows that $\Delta\Sigma_\times$ is consistent with zero. We are therefore confident that no significant systematic effects are present in the GWL data at the scales used in this analysis.

We also expect no signal if we measure the ESD at random points across the K-1000 field, unless there is some residual linear bias in the weak lensing data. This null test is also shown in Fig. 4.8. Both these measurements are consistent with zero and thus we infer that the signal measured around the ACT cluster positions is due to the over-density of mass.

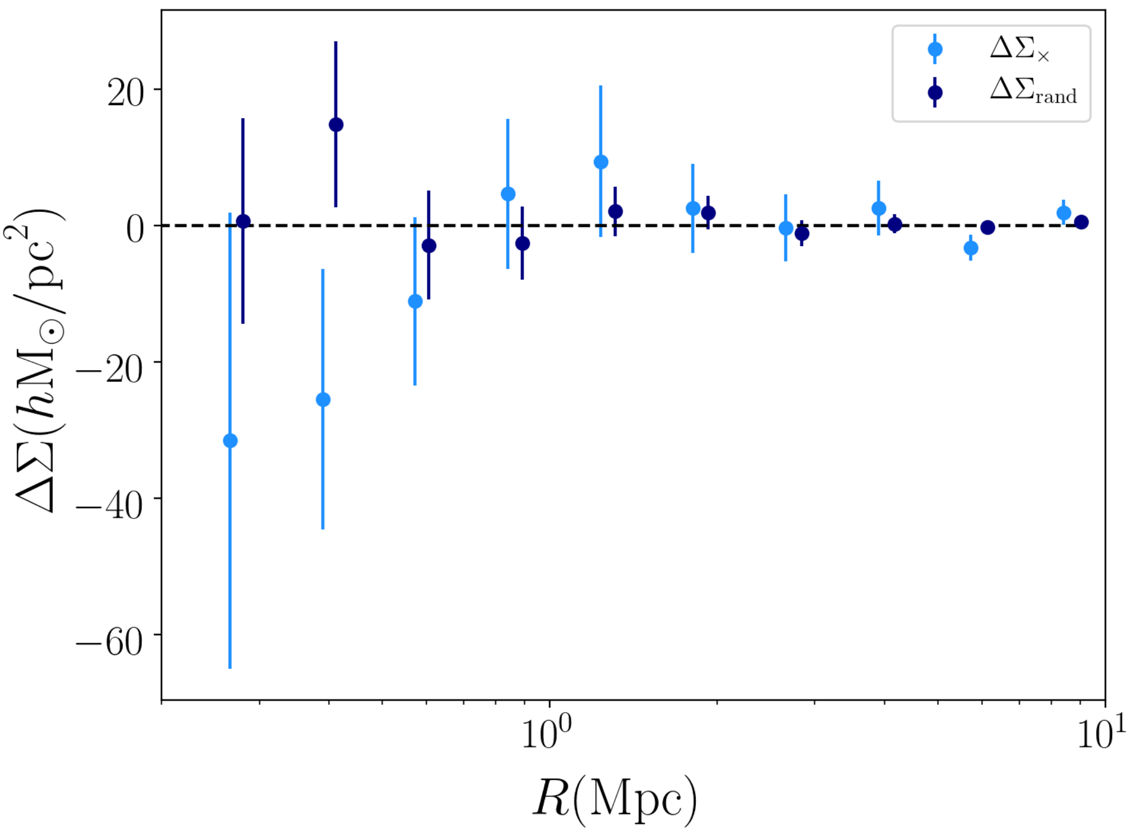


Figure 4.8: Null tests: the cross-component of the ESD, and the ESD measured around random positions in the K-1000 field. Both tests are consistent with zero as expected.

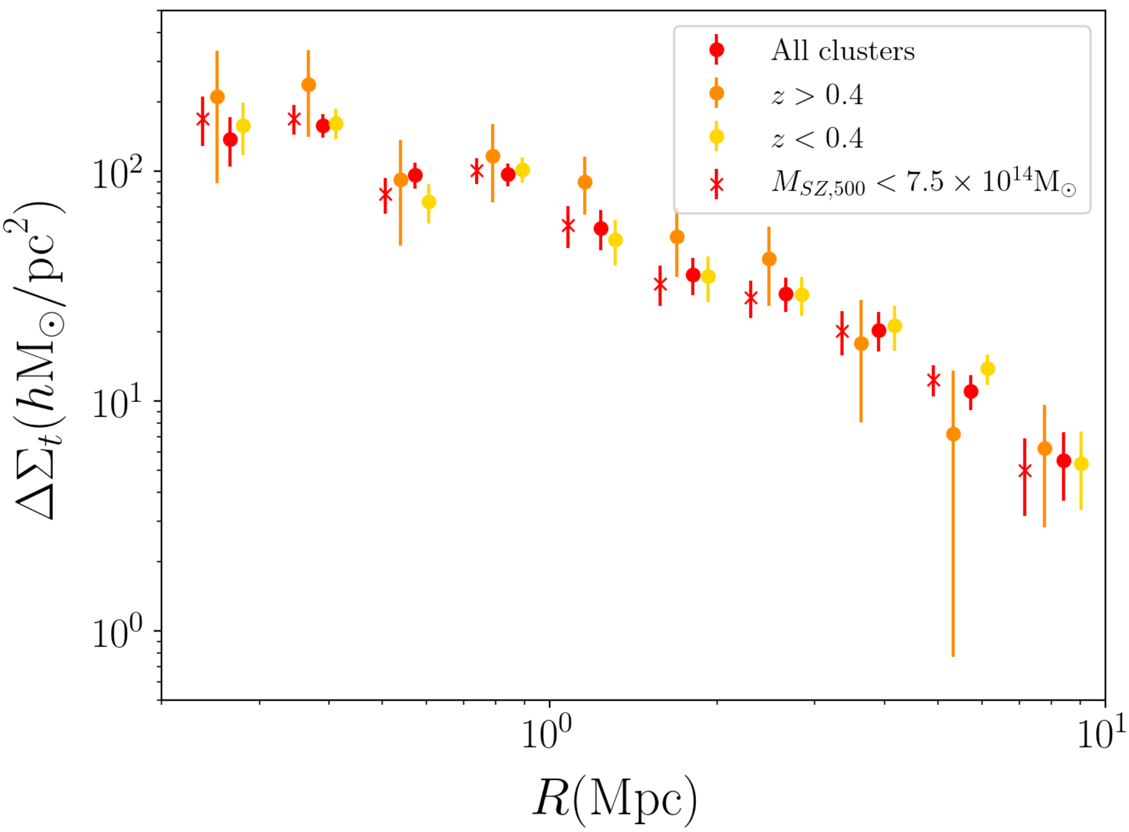


Figure 4.9: Splitting the data: we find consistent ESD measurements when splitting by redshift or mass, indicating that the conclusions are not driven by a subset of the clusters.

#### 4.4.1.4 Consistency Checks

Our cluster sample contains a range of cluster masses which can make modelling the stacked ESD signal more difficult. We therefore test how the ESD changes for different splits in the data. Considering the distribution of SZ estimated masses shown in Fig. 4.2, the majority of clusters are found within the range $1.26 - 6.9 \times 10^{14}\mathrm{M}_\odot$. However, there are two much more massive clusters present in our data set. We remove these two clusters to test if the stacked ESD profile is being dominated by them, shown in Fig. 4.9, and find that ESD profile is not significantly affected. We do not split the remaining 55 clusters into different mass bins since the uncertainty in the SZ mass estimate is relatively large.

We also split the clusters in terms of redshift into two bins about a redshift of 0.4, and find that both splits are consistent. From these checks we conclude that our ESD measurement is not being dominated by a subset of clusters. This is important in the case of a small sample of lenses when only a limited number of bootstrap patches are available.

### 4.4.2 Modelling the Stacked Excess Surface Density

We estimate the weak lensing mass, $M_{\rm WL}$, of the stacked clusters using two methods: a single NFW model and a halo model. The halo model method is superior for modelling the ESD signal, since the single bin NFW model is restricted by the fact that the amplitude of the ESD does not vary linearly with cluster mass. We include the NFW fit to compare our results with previous analyses which have utilised a similar modelling approach.

#### 4.4.2.1 Single NFW

We use the NFW fitting method described in Section 4.3.2, evaluated at the average cluster redshift of $z = 0.273$, which is calculated by weighting the clusters in the same way as the shear is weighted when estimating the ESD using equation 4.14. We estimate the weak lensing mass to be $M_{500}^{\rm NFW} = (5.2 \pm 0.4) \times 10^{14} {\rm M}_{\odot}$ and concentration of $c = 1.7 \pm 0.2$. The best fitting NFW model is shown in Fig. 4.5. We only use the range $(0.4 < R < 4)$ Mpc to avoid any miscentering biases at small scales, and to avoid including the '2-halo' term at large scales.

#### 4.4.2.2 Halo Model Method

Cluster lensing can be understood within the framework of the halo model (Seljak, 2000; Cooray & Sheth, 2002). The projected surface density is completely specified by the cluster–dark matter cross correlation, $\xi_{c,dm}$, which can be computed from a given halo occupation model,

$$\Sigma(R) = 2\bar{\rho} \int_R^\infty \left[1 + \xi_{c,dm}(r)\right] \frac{r\mathrm{d}r}{\sqrt{r^2 - R^2}}\,, \tag{4.23}$$

where $r$ is the 3D comoving distance $r^2 = R^2 + (\chi - \chi_l)^2$. The cluster–dark matter cross correlation power spectrum is given in terms of $\xi_{c,dm}$ as

$$P_{c,dm}(k) = 4\pi \int_0^\infty \xi_{c,dm}(r) \frac{\sin(kr)}{kr} r^2 \mathrm{d}r\,. \tag{4.24}$$

The power spectrum of the cluster–dark matter cross correlation can be split into two parts:

$$P_{c,dm}(k) = P^{1h}_{c,dm}(k) + P^{2h}_{c,dm}(k)\,, \tag{4.25}$$

with the '1–halo term', which describes the non–linear regime at small scales, and the '2–halo term' which describes the linear clustering regime, where galaxy clustering is dominant on large scales.

The '1–halo' term, $P^{1h}_{c,dm}(k)$, describes the dark matter distribution inside halos hosting clusters. For a single cluster, this is

$$P^{1h}_{c,dm}(k) = \frac{M}{\bar{\rho}} u_c(k|M)\,, \tag{4.26}$$

were $u_c(k|M)$ is the normalised Fourier transform of the cluster density profile $\rho(r|M)$ squared, which we assume to be described by an NFW profile. Within the NFW description we also assume the mass concentration relation from Duffy et al. (2008), with normalisation specified by $f_c$.

Since we are measuring a stack of clusters, with masses in the range ($M_{\mathrm{SZ},1} \leq M_{\mathrm{SZ}} \leq M_{\mathrm{SZ},2}$), where $M_{\mathrm{SZ}}$ is the mass determined from SZ observations, the '1–halo' term becomes

$$P^{1h}_{c,dm}(k) = \frac{1}{\bar{\rho}}\int_0^\infty \mathcal{P}(M|M_{\mathrm{SZ},1}, M_{\mathrm{SZ},2}) M u_c(k|M)\mathrm{d}M\,, \tag{4.27}$$

where $\mathcal{P}(M|M_{\mathrm{SZ},1}, M_{\mathrm{SZ},2})$ is the probability that a cluster in the given $M_{\mathrm{SZ}}$ range resides in a halo of mass $M$. From Bayes' theorem,

$$\mathcal{P}(M|M_{\mathrm{SZ},1}, M_{\mathrm{SZ},2})\mathrm{d}M = \frac{\langle N_c|M\rangle \frac{\mathrm{d}n(M)}{\mathrm{d}M}}{\bar{n}_c}\mathrm{d}M\,, \tag{4.28}$$

where $\langle N_c|M\rangle$ is the average number of clusters in the SZ derived mass range $[M_{\mathrm{SZ},1}, M_{\mathrm{SZ},2}]$ in a halo of mass $M$, $\frac{\mathrm{d}n(M)}{\mathrm{d}M}$ is the halo mass function and $\bar{n}_c = \int \langle N_c|M\rangle \frac{\mathrm{d}n(M)}{\mathrm{d}\ln M}\frac{\mathrm{d}M}{M}$ is the comoving number density of clusters in the $M_{\mathrm{SZ}}$ range. Therefore equation 4.27 can be re–written as:

$$P^{1h}_{c,dm}(k) = \frac{1}{\bar{\rho}\bar{n}_c}\int_0^\infty \mathrm{d}M\frac{\mathrm{d}n(M)}{\mathrm{d}\ln M}u_c(k|M)\langle N_c|M\rangle\,. \tag{4.29}$$

This '1–halo' term is constructed so that mis-centering of clusters can be accounted for in the cluster density profile, via the $u_c(k|M)$ term, defined as

$$u_c(k|M) = u_{dm}(k|M)(1 - p_{\mathrm{off}} + p_{\mathrm{off}}e^{-0.5k^2(r_s R_{\mathrm{off}})^2})\,, \tag{4.30}$$

where, $p_{\mathrm{off}}$ and $R_{\mathrm{off}}$ is the probability of mis-centering and the size of the offset respectively.

The '2–halo' term, denoted by $P^{2h}_{c,dm}(k)$, describes the correlation between clusters and dark matter particles belonging to separate haloes, and is given by

$$\begin{aligned} P^{2h}_{c,dm}(k) = &\frac{P_{dm}(k)}{\bar{\rho}}\int_0^\infty \mathcal{P}(M|M_{\mathrm{SZ},1}, M_{\mathrm{SZ},2}) b_h(M)\mathrm{d}M \\ &\int_0^\infty u_{dm}(k|M')b_h(M')\frac{\mathrm{d}n(M')}{\mathrm{d}\ln M'}\mathrm{d}M'\,, \end{aligned} \tag{4.31}$$

where $P_{dm}$ is the linear matter power spectrum and $b_h(M)$ is the halo bias function. The halo bias function describes how halos of mass $M$ are biased with respect to the overall dark matter distribution. Using equation 4.28, we can re–write equation 4.31 as

$$\begin{aligned} P^{2h}_{c,dm}(k) =& \frac{P_{dm}(k)}{\bar{\rho}\bar{n}_c} \int_0^\infty \langle N_c|M\rangle b(M) \frac{\mathrm{d}n(M)}{\mathrm{d}\ln M}\frac{\mathrm{d}M}{M} \\ & \int_0^\infty u_{dm}(k|M')b(M')\frac{\mathrm{d}n(M')}{\mathrm{d}\ln M'}\mathrm{d}M' \,. \end{aligned} \tag{4.32}$$

For the halo occupation statistics that are required to calculate the galaxy–matter power spectrum, we assume a simple power law dependence between halo mass $M$ and $M_{\rm SZ}$

$$\log(M_{\rm SZ}) = \alpha + \beta \log(M)\,, \tag{4.33}$$

to calculate the the average number of clusters. Given the signal-to-noise of the data we fix the mass dependent exponent, $\beta$, equal to 1, so that we can focus on $\alpha$, which quantifies the constant mass bias between SZ mass and the true mass. For our sample of clusters in the range $[M_{\rm SZ,1}, M_{\rm SZ,2}]$, the average number of clusters is then given by,

$$\langle N_c|M\rangle = \frac{1}{\sqrt{2\pi}\sigma_c}\int_{M_{\rm SZ,1}}^{M_{\rm SZ,2}} S\exp\left[\frac{-(\log M - \log M_{\rm SZ})^2}{2\sigma_c^2}\right]\mathrm{d}M\,, \tag{4.34}$$

where we have assumed a lognormal scatter, $\sigma_c$, and $S = S(M_{\rm SZ}, z)$ is the SZ-experiment selection function. We fix the SZ mass scatter to $\sigma_c = 0.2$, firstly because lensing does not constrain this well and secondly because this is the same scatter assumed to correct the Eddington bias for the SZ masses derived for the ACT clusters (Hilton & ACT Collaboration, in prep.). Finally the average number density of the clusters in our sample is given by

$$\bar{n}_c = \int \langle N_c|M\rangle)\frac{\mathrm{d}n(M)}{\mathrm{d}\ln M}\frac{\mathrm{d}M}{M}\,. \tag{4.35}$$

In this model we fit for the following set of parameters: $\{f_c, \alpha, b_h\}$. Since we are not using large scales we do not expect to be able to constrain the halo bias term particularly well, but we include it for completeness. The average halo mass, which is the main parameter we are interested in, is a derived parameter, given by

$$M_{500}^{\mathrm{WL}} \equiv M_h = \frac{1}{\bar{n}_c} \int \langle N_c | M \rangle \frac{\mathrm{d}n(M)}{\mathrm{d}\ln M} \mathrm{d}M \,. \tag{4.36}$$

We use Bayesian inference to recover the posterior probability distribution of these three parameters using emcee, the MCMC Python package (Foreman-Mackey et al., 2013). We use wide flat priors for all parameters ($f_c = [0, 10], \alpha = [-5, 5], b_h = [0, 10]$) and assume a Gaussian likelihood. The halo model is evaluated at a median redshift of $z = 0.273$ – calculated using the same weighting as equation 4.14. Fig. 4.11 shows the estimated distributions of the halo model parameters. From our MCMC sampling analysis, we infer the weak lensing mass estimate to be $M_{500}^{\mathrm{WL}} = (4.7 \pm 0.9) \times 10^{14}\mathrm{M}_{\odot}$. Our best fitting halo model is shown in Fig. 4.5; it is a good fit to the data. The estimated mass is consistent with the NFW model but has larger uncertainty due to marginalising over more model parameters.

### 4.4.3 Calibration Bias: $(1 - b)$

To estimate the hydrostatic mass bias $(1-b)$ we combine estimates of the SZ inferred cluster masses by taking the weighted average. Here clusters are weighted in the same way as in the stacked ESD measurement described in equation 4.14. We estimate the average SZ inferred mass to be $M_{500}^{\mathrm{SZ}} = 3.6^{+1.0}_{-0.8} \times 10^{14}\mathrm{M}_{\odot}$.

From our halo model estimate of the weak lensing mass, we estimate $(1 - b) = 0.76^{+0.25}_{-0.21}$. This is consistent with our estimate using a single NFW profile of $(1-b) = 0.68^{+0.20}_{-0.16}$. In Figure 4.11 we show our new estimate together with a compilation of measurements from other data combinations. Our results are consistent with analyses

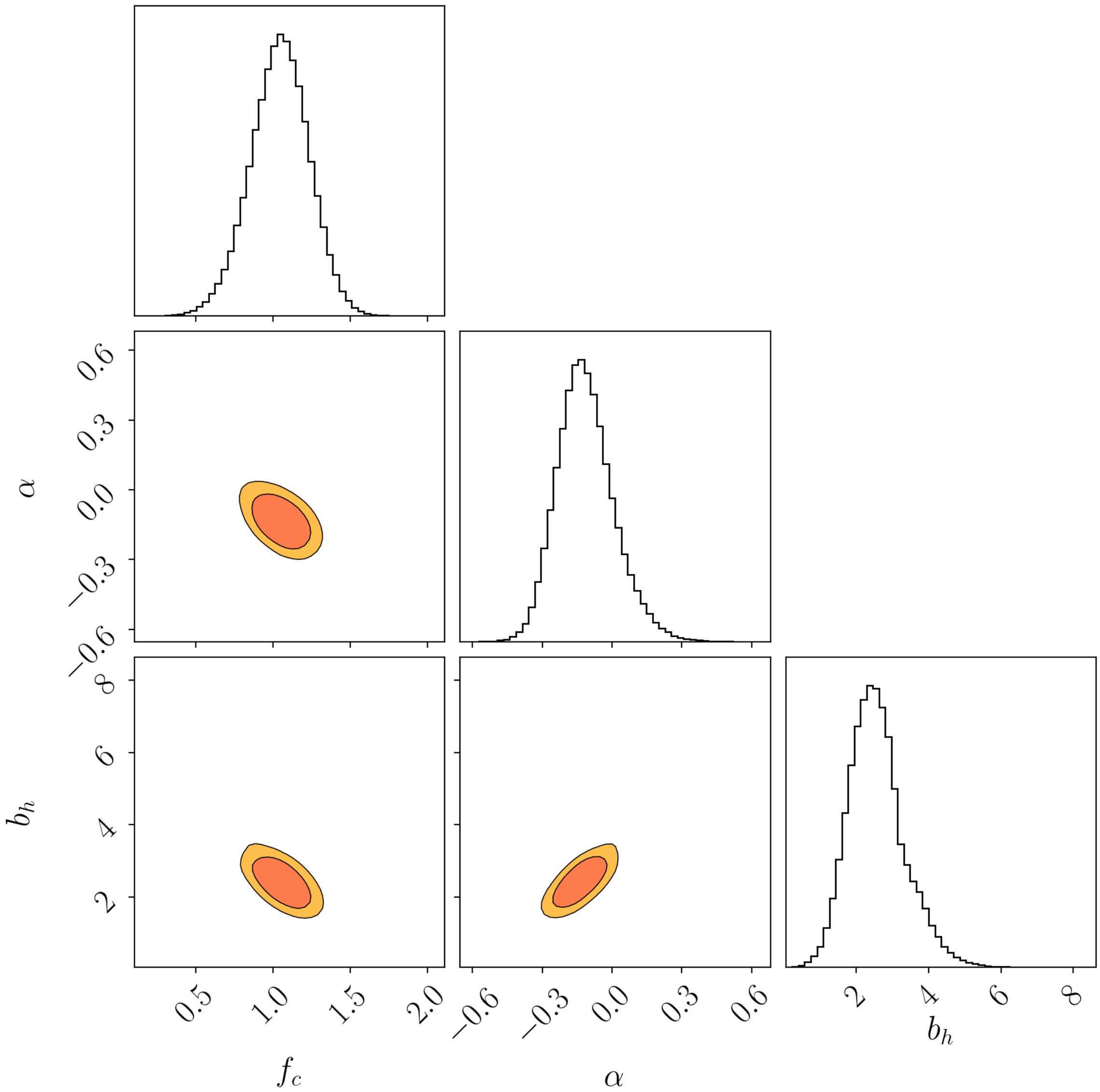


Figure 4.10: Marginalized posterior distributions (68 and 95% CL) for the three halo model parameters.

of ACT and *Planck* clusters in a similar mass range using HSC (Miyatake et al., 2019; Medezinski et al., 2018) and CS82 (Battaglia et al., 2016). A similar bias is estimated from the CLASH (Penna-Lima et al., 2017), WtG (von der Linden et al., 2014) and CCCP (Hoekstra et al., 2015) analyses, for higher mass clusters. ACT and *Planck* cluster mass estimates can be directly compared since they are derived from the same SZ-mass scaling relations and pressure profiles.

## 4.5 Conclusions

We have estimated the masses of a new sample of galaxy clusters detected using the Atacama Cosmology Telescope. Stacking the signal from 57 high signal-to-noise clusters, we detect the weak lensing signal at $20\sigma$ significance. We estimate the stacked mass to be $M_{500}^{\mathrm{WL}} = (4.7 \pm 0.9) \times 10^{14}\mathrm{M}_{\odot}$, using an analytical halo model formalism which accounts for the ACT SZ cluster selection. By comparing this gravitational lensing estimate of mass to the mass inferred from the SZ signal itself, we provide a new estimate of the calibration of the SZ Compton-$y$ parameter mass scaling relation.

We find our estimate of the mass calibration bias to be consistent with estimates made using other contemporary weak lensing surveys including HSC. This measurement does not indicate a significant departure from the predicted value of the mass bias from *Planck* primary CMB measurements if the $\Lambda$CDM model is correct (Planck Collaboration, 2018), given the SZ clusters observed by *Planck*. The aim is to eventually constrain cosmology with these clusters, but we defer that analysis to future work with a larger sample. Nevertheless applied as a prior, this will be useful for extracting cosmological information from the ACT cluster sample, to estimate the amplitude of structure formation and possible extensions to $\Lambda$CDM including non-zero neutrino mass and deviations from a cosmological constant.

In comparing $(1 - b)$ estimates, shown in Fig. 4.11, the clusters that are in

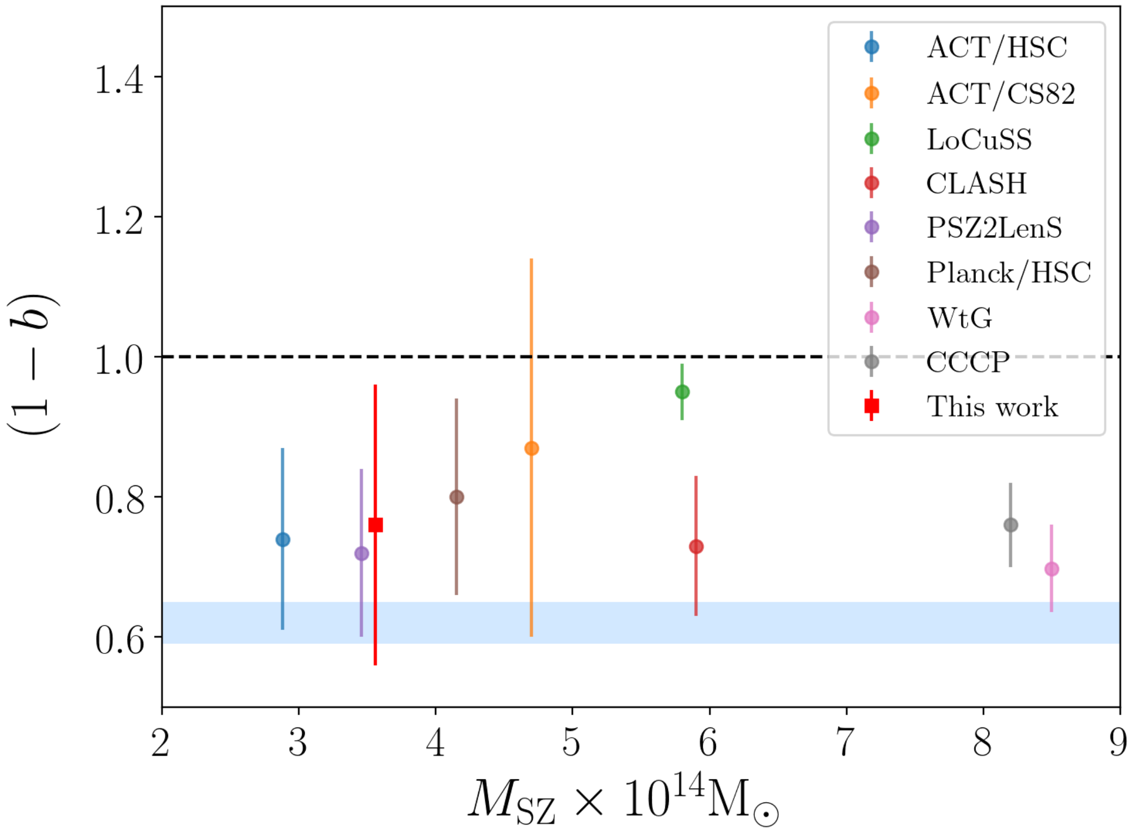


Figure 4.11: The estimated $(1-b)$ bias parameter from this analysis (ACT SZ-detected clsuters calibrated with KiDS weak lensing), compared to other recent results. At the lower mass range, our results are consistent with analyses of ACT and *Planck* clusters using HSC (Miyatake et al., 2019; Medezinski et al., 2018) and CS82 (Battaglia et al., 2016). A similar bias is estimated from the CLASH (Penna-Lima et al., 2017), WtG (von der Linden et al., 2014) and CCCP (Hoekstra et al., 2015) analyses, for higher mass clusters. The blue band indicates the prediction from *Planck* primary CMB measurements if the $\Lambda$CDM model is correct (Planck Collaboration, 2018), given the SZ clusters observed by *Planck*.

ACT/HSC and ACT/CS82 analyses will be different to ours. However, the high mass clusters present in our sample will be detected by *Planck* too. *Planck* and ACT use the same mass scaling relations so they can be compared – this is not the case for example SPT clusters. To be able to combine all the measurements shown in Fig. 4.11, we would need to account for covariances between different data sets since some clusters appear in more than one sample and the fact that the ACT and *Planck* selection functions are different.

The measurement is currently limited by the number of clusters in the sample. With the next data release from ACT we would expect to double the number in the KiDS footprint. Using a weak lensing survey like HSC, the increased depth would also improve the significance of the measurement since clusters can be detected at higher redshifts in CMB data. Looking to the future of these mass calibration bias studies, the next development that needs to be made is moving away from assuming the X-ray calibrated scaling relation and instead considering the relation between the measured Compton-$y$ parameter and the weak lensing mass directly. This is not the data set to do that with, but by SO and LSST the step-up in the number of clusters is huge. Also with a larger sample, as the error bars shrinks, when modelling the lensing signal we would be dependent on cosmological parameters – currently assuming a KiDS or Planck best fit cosmology has no implication on the masses we infer. We will need to estimate the relationship, and scatter, between the SZ signal and the underlying mass, and include these in a joint likelihood.

The comparison and combination of these calibrations using KiDS, HSC and DES data will be valuable in laying the ground work for these future efforts with LSST and SO.

# Chapter 5

# Conclusions and Future Work

Evidence for the presence of dark matter and dark energy has been well established, yet understanding them physically poses a huge challenge to modern cosmology. These two components form part of the ΛCDM model that has been very successful observationally. The *Planck* satellite, as well as ground based CMB, LSS and GWL experiments has brought us into an era of precision cosmology, with present data sets testing the current paradigm to high accuracy. Next generation surveys including *Euclid*, LSST and SO, will build on these successes, moving towards complete sky coverage and increased sensitivity, with the ability to probe cosmology in a variety of ways. Collaborations have only just begun to explore the benefits that can be achieved by bringing together data from different surveys. There are many synergies between CMB and GWL data sets, of which in this thesis we have focused on the CMB lensing/GWL cross correlation and the use of GWL to calibrate the masses of galaxy clusters selected using the SZ effect seen in CMB maps.

In this thesis we investigated optimal ways to estimate the GWL-CMB lensing cross-correlation power spectrum with pseudo-$C_\ell$ estimators. We considered the effects of convergence reconstruction, masking, zero-padding, weight maps, apodisation and curved-sky projection with the public code NaMaster using realistic simulations.

We found that in each case the input theoretical power spectrum was recovered within our error budget and the B-mode null test was always consistent with zero. We established the impact of these analysis choices on the signal-to-noise of the measurement and concluded that for a GWL mask apodisation reduces the area of the mask significantly and therefore increases the noise in the measurement. We showed that the optimal procedure was to use a weight mask constructed from the inverse variance weights of the galaxy sample derived from the shape measurement process. We also noted that in the common case of different survey areas, zero-padding each survey to utilise all the data available reduces the size of the error bars.

In chapter 3, we created GWL shear maps from shape measurements of galaxies in the redshift range of 0.1 to 1.2. Using the pipeline described above we measured the GWL-CMB lensing cross-correlation power spectrum with the latest data from ACT and KiDS. The cross-correlation was detected with a significance of $4.7\sigma$. We tested the data by performing a B-mode null test and re-measuring the cross-correlation power spectrum with galaxy shear maps where the KiDS galaxies have been randomly rotated. From our measurement of the power spectrum we presented amplitude fits to a *Planck* and a KiDS best fit cosmology. Using blinded KiDS data we found that the amplitude inferred against a *Planck* cosmology is consistent with previous cross-correlation analyses using other data sets. From this analysis we also found the data favours a KiDS cosmology, although at low significance. We also showed that when accounting for a realistic estimate of the intrinsic alignment amplitude the consistency between the data and both a *Planck* and KiDS best fit cosmology improved. We presented fits for $\Omega_m$ and $\sigma_8$ with informed priors and found constraints on the $S_8$ parameter which were consistent with the KV-450 results. These conclusions will soon be refined with unblinded shear catalogues. When considering the next data set from ACT, we showed that constraints on the $S_8$ parameter will improve, whilst loosening the priors we applied to GWL systematic parameters.

From the latest ACT SZ selected cluster sample we found 57 high signal-to-noise clusters in the KiDS survey area. We measured the lensing signal in the form of the excess surface density around 27 individual clusters which had a $S/N > 5$ and estimated their individual masses by fitting a simple NFW profile to each lensing measurement. We then performed the same lensing measurement on the stack of 57 clusters and fitted a single NFW profile to the stacked excess surface density in accordance with previously published studies. We modelled the stacked lensing signal with a second method that used an analytical halo model formalism. This approach accounted for the '2-halo' term and included selection effects from the ACT SZ cluster detection process. From these estimates of the 'true' cluster mass, we presented a new measurement of the SZ-mass calibration bias, which we found to be consistent with previous estimates and the value of the bias needed for cosmology from *Planck* clusters to be consistent with cosmology from *Planck* primary CMB. We checked our measurement against the effects of cluster mis-centering, dilution due to large photometric redshift uncertainty and B-modes in the KiDS data.

A natural extension to the work presented in this thesis would be to apply these tools to data from SO and LSST, which will be available in the early 2020s. For these measurements the additional area, shown in Fig. 5.1 is the main factor in increasing the signal-to-noise. With this improvement, we will be able to use the cross-correlation power spectrum to constrain $\sigma_8$ and $\Omega_m$, as well as investigating the total neutrino mass and baryon feedback parameters on small scales. These future studies will have to include improved modelling of intrinsic alignments and a wider variety of baryon feedback models. With the increase in signal-to-noise and greater depth, a tomographic analysis will be possible so that the growth of structure can be measured free of galaxy bias. This measurement will be complimentary to the LSS surveys, including the upcoming wide field survey DESI, which will probe the growth factor too.

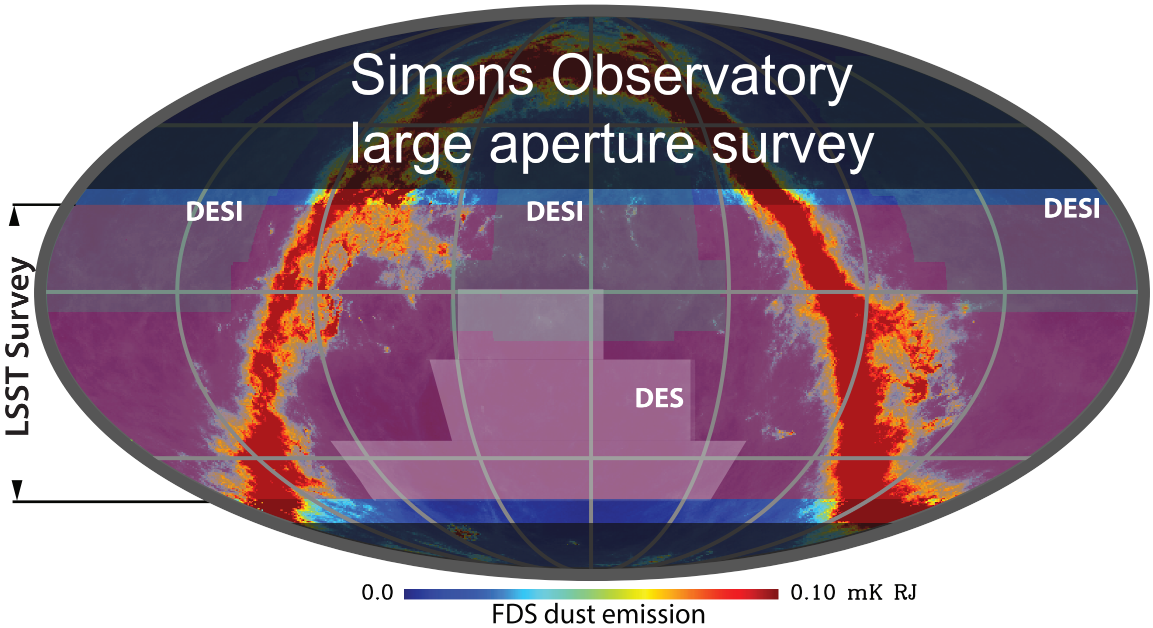


Figure 5.1: Coverage of upcoming ground based cosmology experiments. This huge overlapping area makes combined probe analyses a natural progression. *Image credit: (Ade et al., 2019)*

ACT is in the unique and exciting position of overlapping with all three of the current GWL surveys (DES, HSC and KiDS). Using the cross-correlation measurement between each of these GWL surveys with CMB lensing from ACT, we can test and compare multiplicative bias and photometric redshift bias. These analyses are already planned independently for cosmological parameter estimation, therefore a logical development would be to consider them together as a test of consistency between lensing data sets.

We are already seeing a huge increase in number of clusters found when including the wider field seasons of Advanced ACT. This will require the community to build on the current mass calibration studies and develop more complex modelling of cluster samples. This mass calibration is essential for cosmology from clusters. With SO and LSST on the horizon we would like to take the opportunity to combine cluster mass information from GWL, CMB lensing and Compton-$y$ information.

To fully exploit these future data sets, we need to move towards a complete combined probe analysis that includes cluster measurements on the same footing as CMB and clustering data. So far, most core cosmological analyses have not included clusters or fully accounted for the covariances between clusters and other probes. To maximise the data from LSST and SO, the necessary next step will be to include weak lensing, galaxy clustering and cluster counts together with the primary CMB. This will require implementing new statistical techniques which include systematic uncertainties in the initial part of the modelling. These measurements can be used to unravel any tensions – should they remain – between low and high redshift probes and investigate models beyond the ΛCDM paradigm.

# References


Abbott, T.M.C. et al. Dark Energy Survey year 1 results: Cosmological constraints from galaxy clustering and weak lensing. *Physical Review D*, 98(4):043526, August 2018.

Ade, P.A.R. et al. Constraints on Primordial Gravitational Waves Using *Planck*, WMAP, and New BICEP2/*Keck* Observations through the 2015 Season. *Phys. Rev. Lett.*, 121:221301, November 2018.

Ade, P. et al. The Simons Observatory: science goals and forecasts. *Journal of Cosmology and Astroparticle Physics*, 2019(2):056, February 2019.

Aihara, H. et al. The Hyper Suprime-Cam SSP Survey: Overview and survey design. *Publications of the Astronomical Society of Japan*, 70:S4, January 2018.

Aiola, S. et al. The Atacama Cosmology Telescope: Data Release 2 ACTPol Data and Cosmological Results. in prep.

Alam, S. et al. The clustering of galaxies in the completed SDSS-III Baryon Oscillation Spectroscopic Survey: cosmological analysis of the DR12 galaxy sample. *Monthly Notices of the Royal Astronomical Society*, 470(3):2617–2652, September 2017.

Alcock, C. et al. The MACHO Project Large Magellanic Cloud Microlensing Results from the First Two Years and the Nature of the Galactic Dark Halo. *Astrophysical Journal*, 486(2):697–726, September 1997.

Allen, S.W., Evrard, A.E. and Mantz, A.B. Cosmological Parameters from Observations of Galaxy Clusters. *Annual Review of Astronomy and Astrophysics*, 49: 409–470, 2011.

Allison, R. et al. The Atacama Cosmology Telescope: measuring radio galaxy bias through cross-correlation with lensing. *Monthly Notices of the Royal Astronomical Society*, 451(1):849–858, July 2015.

Alonso, D., Sanchez, J. and Slosar, A. A unified pseudo-$C_\ell$ framework. *Monthly Notices of the Royal Astronomical Society*, 484(3):4127–4151, April 2019.

Alsing, J. et al. Hierarchical cosmic shear power spectrum inference. *Monthly Notices of the Royal Astronomical Society*, 455(4):4452–4466, February 2016.

Amendola, L. et al. Cosmology and Fundamental Physics with the Euclid Satellite. *Living Reviews in Relativity*, 16(1):6, September 2013.

Amon, A. et al. KiDS-i-800: comparing weak gravitational lensing measurements from same-sky surveys. *Monthly Notices of the Royal Astronomical Society*, 477 (4):4285–4307, July 2018.

Anderson, L. et al. The clustering of galaxies in the SDSS-III Baryon Oscillation Spectroscopic Survey: measuring $D_A$ and H at z = 0.57 from the baryon acoustic peak in the Data Release 9 spectroscopic Galaxy sample. *Monthly Notices of the Royal Astronomical Society*, 439(1):83–101, March 2014.

Arnaud, M. et al. The universal galaxy cluster pressure profile from a representative sample of nearby systems (REXCESS) and the $Y_{SZ}$ - $M_{500}$ relation. *Astronomy and Astrophysics*, 517:A92, July 2010.

Asgari, M. et al. Flat-SkyPseudo-Cls analysis for weak gravitational lensing. *Monthly Notices of the Royal Astronomical Society*, 479(1):454–477, September 2018.

Asorey, J. et al. Recovering 3D clustering information with angular correlations. *Monthly Notices of the Royal Astronomical Society*, 427(3):1891–1902, December 2012.

Bacon, D.J., Refregier, A.R. and Ellis, R.S. Detection of weak gravitational lensing by large-scale structure. *Monthly Notices of the Royal Astronomical Society*, 318 (2):625–640, Octoberober 2000.

Bahcall, J.N. et al. M Dwarfs, Microlensing, and the Mass Budget of the Galaxy. *Astrophysical Journal, Letters*, 435:L51, November 1994.

Barbosa, D. et al. The Sunyaev-Zel'dovich effect and the value of {OMEGA}_0_. *Astronomy and Astrophysics*, 314:13–17, October 1996.

Bardeen, J.M. et al. The Statistics of Peaks of Gaussian Random Fields. *Astrophysical Journal*, 304:15, May 1986.

Bartelmann, M. and Schneider, P. Weak gravitational lensing. *Physics Reports*, 340 (4-5):291–472, January 2001.

Battaglia, N. et al. Simulations of the Sunyaev-Zel'dovich Power Spectrum with Active Galactic Nucleus Feedback. *Astrophysical Journal*, 725(1):91–99, December 2010.

Battaglia, N. et al. Weak-lensing mass calibration of the Atacama Cosmology Telescope equatorial Sunyaev-Zel'dovich cluster sample with the Canada- France-Hawaii telescope stripe 82 survey. *Journal of Cosmology and Astro-Particle Physics*, 2016:013, 2016.

Battye, R.A. and Weller, J. Constraining cosmological parameters using Sunyaev-Zel'dovich cluster surveys. *Physical Review D*, 68(8):083506, October 2003.

Baxter, E. et al. Joint measurement of lensing-galaxy correlations using SPT and DES SV data. *Monthly Notices of the Royal Astronomical Society*, 461(4):4099–4114, October 2016.

Baxter, E.J. et al. A measurement of CMB cluster lensing with SPT and DES year 1 data. *Monthly Notices of the Royal Astronomical Society*, 476(2):2674–2688, May 2018.

Benedict, G.F. et al. Hubble Space Telescope Fine Guidance Sensor Parallaxes of Galactic Cepheid Variable Stars: Period-Luminosity Relations. *The Astronomical Journal*, 133(4):1810–1827, April 2007.

Benítez, N. Bayesian Photometric Redshift Estimation. *Astrophysical Journal*, 536 (2):571–583, June 2000.

Benson, B.A. et al. Cosmological Constraints from Sunyaev-Zel'dovich-selected Clusters with X-Ray Observations in the First 178 $\deg^2$ of the South Pole Telescope Survey. *Astrophysical Journal*, 763:147, 2013.

Bertone, G., Hooper, D. and Silk, J. Particle dark matter: evidence, candidates and constraints. *Physics Reports*, 405(5-6):279–390, January 2005.

Beutler, F. et al. The 6dF Galaxy Survey: baryon acoustic oscillations and the local Hubble constant. *Monthly Notices of the Royal Astronomical Society*, 416(4): 3017–3032, October 2011.

Bianchini, F. et al. Cross-correlation between the CMB Lensing Potential Measured by Planck and High-z Submillimeter Galaxies Detected by the Herschel-Atlas Survey. *Astrophysical Journal*, 802(1):64, March 2015.

Birkinshaw, M., Gull, S.F. and Hardebeck, H. The Sunyaev-Zel'dovich effect towards three clusters of galaxies. *Nature*, 309:34–35, May 1984.

Blake, C. et al. The WiggleZ Dark Energy Survey: joint measurements of the expansion and growth history at z < 1. *Monthly Notices of the Royal Astronomical Society*, 425(1):405–414, September 2012.

Blanchard, A. and Schneider, J. Gravitational lensing effect on the fluctuations of the cosmic background radiation. *Astronomy and Astrophysics*, 184(1-2):1–6, October 1987.

Bleem, L.E. et al. A Measurement of the Correlation of Galaxy Surveys with CMB Lensing Convergence Maps from the South Pole Telescope. *Astrophysical Journal, Letters*, 753(1):L9, July 2012.

Blumenthal, G.R. et al. Formation of galaxies and large-scale structure with cold dark matter. *Nature*, 311:517–525, Octoberober 1984.

Bocquet, S. et al. Cluster Cosmology Constraints from the 2500 deg$^2$ SPT-SZ Survey: Inclusion of Weak Gravitational Lensing Data from Magellan and the Hubble Space Telescope. *Astrophysical Journal*, 878(1):55, June 2019.

Bode, P. et al. Calibration of Nonthermal Pressure in Global Dark Matter Simulations of Clusters of Galaxies. *arXiv e-prints*, art. arXiv:1204.1762, April 2012.

Böhringer, H. et al. The Extended Northern ROSAT Galaxy Cluster Survey (NORAS II). I. Survey Construction and First Results. *The Astronomical Journal*, 153(5): 220, May 2017.

Bolzonella, M., Miralles, J.M. and Pelló, R. Photometric redshifts based on standard SED fitting procedures. *Astronomy and Astrophysics*, 363:476–492, November 2000.

Bond, J.R., Jaffe, A.H. and Knox, L. Estimating the power spectrum of the cosmic microwave background. *Physical Review D*, 57(4):2117–2137, February 1998.

Bond, J.R. Signal-to-Noise Eigenmode Analysis of the Two-Year COBE Maps. *Physical Review Letters*, 74(22):4369–4372, May 1995.

Bonvin, C. and Durrer, R. What galaxy surveys really measure. *Physical Review D*, 84(6):063505, September 2011.

Bonvin, V. et al. H0LiCOW - V. New COSMOGRAIL time delays of HE 0435-1223: $H_0$ to 3.8 per cent precision from strong lensing in a flat ΛCDM model. *Monthly Notices of the Royal Astronomical Society*, 465(4):4914–4930, March 2017.

Boughn, S. and Crittenden, R. A correlation between the cosmic microwave background and large-scale structure in the Universe. *Nature*, 427(6969):45–47, January 2004.

Brammer, G.B., van Dokkum, P.G. and Coppi, P. EAZY: A Fast, Public Photometric Redshift Code. *Astrophysical Journal*, 686(2):1503–1513, October 2008.

Cacciato, M., van Uitert, E. and Hoekstra, H. Describing galaxy weak lensing measurements from tenths to tens of Mpc and up to z 0.6 with a single model. *Monthly Notices of the Royal Astronomical Society*, 437(1):377–390, January 2014.

Caldwell, R.R., Dave, R. and Steinhardt, P.J. Cosmological Imprint of an Energy Component with General Equation of State. *Physical Review Letters*, 80(8):1582–1585, February 1998.

Challinor, A. et al. PolSpice: Spatially Inhomogeneous Correlation Estimator for Temperature and Polarisation. Astrophysics Source Code Library, September 2011.

Chang, C. et al. The effective number density of galaxies for weak lensing measurements in the LSST project. *Monthly Notices of the Royal Astronomical Society*, 434(3):2121–2135, September 2013.

Chisari, N. et al. Intrinsic alignments of galaxies in the Horizon-AGN cosmological hydrodynamical simulation. *Monthly Notices of the Royal Astronomical Society*, 454(3):2736–2753, December 2015.

Chisari, N.E. et al. CCL: Core Cosmology Library, January 2019.

Choi, A. et al. CFHTLenS and RCSLenS: testing photometric redshift distributions using angular cross-correlations with spectroscopic galaxy surveys. *Monthly Notices of the Royal Astronomical Society*, 463(4):3737–3754, December 2016.

Chon, G. et al. Fast estimation of polarization power spectra using correlation functions. *Monthly Notices of the Royal Astronomical Society*, 350(3):914–926, May 2004.

Cole, S. et al. The 2dF Galaxy Redshift Survey: power-spectrum analysis of the final data set and cosmological implications. *Monthly Notices of the Royal Astronomical Society*, 362(2):505–534, September 2005.

Colless, M. et al. The 2dF Galaxy Redshift Survey: spectra and redshifts. *Monthly Notices of the Royal Astronomical Society*, 328(4):1039–1063, December 2001.

Contaldi, C.R., Hoekstra, H. and Lewis, A. Joint Cosmic Microwave Background and Weak Lensing Analysis: Constraints on Cosmological Parameters. *Physical Review Letters*, 90(22):221303, June 2003.

Cooray, A. and Sheth, R. Halo models of large scale structure. *Physics Reports*, 372 (1):1–129, December 2002.

Copeland, E.J., Sami, M. and Tsujikawa, S. Dynamics of Dark Energy. *International Journal of Modern Physics D*, 15(11):1753–1935, January 2006.

Crill, B.P. et al. In *Proceedings of the Society of Photo-Optical Instrumentation Engineers*, volume 7010 of *Society of Photo-Optical Instrumentation Engineers (SPIE) Conference Series*, page 70102P, July 2008. doi: 10.1117/12.787446.

Darwish, O. et al. The Atacama Cosmology Telescope:A CMB lensing mass map and its cross-correlation with BOSS-CMASS galaxies. in prep.

Das, S. et al. Detection of the Power Spectrum of Cosmic Microwave Background Lensing by the Atacama Cosmology Telescope. *Physical Review Letters*, 107(2): 021301, July 2011.

de Haan, T. et al. Cosmological Constraints from Galaxy Clusters in the 2500 Square-degree SPT-SZ Survey. *Astrophysical Journal*, 832:95, 2016.

de Jong, J.T.A. et al. The first and second data releases of the Kilo-Degree Survey. *Astronomy and Astrophysics*, 582:A62, 2015.

de Jong, J.T.A. et al. The third data release of the Kilo-Degree Survey and associated data products. *Astronomy and Astrophysics*, 604:A134, 2017.

de Jong, R.S. et al. In *Proceedings of the Society of Photo-Optical Instrumentation Engineers*, volume 8446 of *Society of Photo-Optical Instrumentation Engineers (SPIE) Conference Series*, page 84460T, September 2012. doi: 10.1117/12.926239.

DESI Collaboration et al. The DESI Experiment Part I: Science,Targeting, and Survey Design. *arXiv e-prints*, art. arXiv:1611.00036, October 2016.

Dicke, R.H. et al. Cosmic Black-Body Radiation. *Astrophysical Journal*, 142:414–419, July 1965.

Dietrich, J.P. et al. Sunyaev-Zel'dovich effect and X-ray scaling relations from weak lensing mass calibration of 32 South Pole Telescope selected galaxy clusters. *Monthly Notices of the Royal Astronomical Society*, 483(3):2871–2906, March 2019.

Dodelson, S. *Modern cosmology*. 2003.

Duffy, A.R. et al. Dark matter halo concentrations in the Wilkinson Microwave Anisotropy Probe year 5 cosmology. *Monthly Notices of the Royal Astronomical Society*, 390(1):L64–L68, October 2008.

Dunkley, J. et al. Five-Year Wilkinson Microwave Anisotropy Probe Observations: Likelihoods and Parameters from the WMAP Data. *Astrophysical Journal, Supplement*, 180(2):306–329, February 2009.

Dvornik, A. et al. Unveiling galaxy bias via the halo model, KiDS, and GAMA. *Monthly Notices of the Royal Astronomical Society*, 479:1240–1259, 2018.

EBEX Collaboration et al. The EBEX Balloon-borne Experiment—Gondola, Attitude Control, and Control Software. *Astrophysical Journal, Supplement*, 239(1):9, November 2018.

Efstathiou, G. Myths and truths concerning estimation of power spectra: the case for a hybrid estimator. *Monthly Notices of the Royal Astronomical Society*, 349(2): 603–626, April 2004.

Eisenstein, D.J. and Hu, W. Baryonic Features in the Matter Transfer Function. *Astrophysical Journal*, 496(2):605–614, Mar 1998.

Eisenstein, D.J. et al. Detection of the Baryon Acoustic Peak in the Large-Scale Correlation Function of SDSS Luminous Red Galaxies. *Astrophysical Journal*, 633 (2):560–574, November 2005.

Eriksen, H.K. et al. Power Spectrum Estimation from High-Resolution Maps by Gibbs Sampling. *Astrophysical Journal, Supplement*, 155(2):227–241, December 2004.

Fenech Conti, I. et al. Calibration of weak-lensing shear in the Kilo-Degree Survey. *Monthly Notices of the Royal Astronomical Society*, 467:1627–1651, May 2017.

Foreman-Mackey, D. et al. emcee: The MCMC Hammer. *Publications of the Astronomical Society of the Pacific*, 125:306, March 2013.

Freedman, W.L. Correction: Cosmology at a crossroads. *Nature Astronomy*, 1:0169, June 2017.

Freedman, W.L. et al. Carnegie Hubble Program: A Mid-infrared Calibration of the Hubble Constant. *Astrophysical Journal*, 758(1):24, October 2012.

Friedmann, A. Über die Möglichkeit einer Welt mit konstanter negativer Krümmung des Raumes. *Zeitschrift fur Physik*, 21(1):326–332, December 1924.

Fu, L. et al. Very weak lensing in the CFHTLS wide: cosmology from cosmic shear in the linear regime. *Astronomy and Astrophysics*, 479(1):9–25, February 2008.

García-García, C., Alonso, D. and Bellini, E. Disconnected pseudo-$C_\ell$ covariances for projected large-scale structure data. *arXiv e-prints*, art. arXiv:1906.11765, June 2019.

Geach, J.E. et al. A Direct Measurement of the Linear Bias of Mid-infrared-selected Quasars at z $\approx$ 1 Using Cosmic Microwave Background Lensing. *Astrophysical Journal, Letters*, 776(2):L41, October 2013.

George, M.R. et al. Galaxies in X-Ray Groups. II. A Weak Lensing Study of Halo Centering. *Astrophysical Journal*, 757(1):2, September 2012.

Giannantonio, T. et al. CMB lensing tomography with the DES Science Verification galaxies. *Monthly Notices of the Royal Astronomical Society*, 456(3):3213–3244, March 2016.

Górski, K.M. et al. HEALPix: A Framework for High-Resolution Discretization and Fast Analysis of Data Distributed on the Sphere. *Astrophysical Journal*, 622(2): 759–771, April 2005.

Górski, K.M. On Determining the Spectrum of Primordial Inhomogeneity from the COBE DMR Sky Maps: Method. *Astrophysical Journal*, 430:L85, August 1994.

Graff, D.S. and Freese, K. The Mass Function of Low-Mass Halo Stars: Limits on Baryonic Halo Dark Matter. *Astrophysical Journal, Letters*, 467:L65, August 1996.

Guth, A.H. Inflationary universe: A possible solution to the horizon and flatness problems. *Physical Review D*, 23(2):347–356, January 1981.

Hall, A. and Taylor, A. Intrinsic alignments in the cross-correlation of cosmic shear and cosmic microwave background weak lensing. *Monthly Notices of the Royal Astronomical Society*, 443:L119–L123, September 2014.

Hand, N. et al. First measurement of the cross-correlation of CMB lensing and galaxy lensing. *Physical Review D*, 91(6):062001, Mar 2015.

Hansen, F.K., Górski, K.M. and Hivon, E. Gabor transforms on the sphere with applications to CMB power spectrum estimation. *Monthly Notices of the Royal Astronomical Society*, 336(4):1304–1328, November 2002.

Hanson, D. et al. Detection of $b$-mode polarization in the cosmic microwave background with data from the south pole telescope. *Physical Review Letters*, 111: 141301, September 2013.

Harnois-Déraps, J. et al. CFHTLenS and RCSLenS cross-correlation with Planck lensing detected in fourier and configuration space. *Monthly Notices of the Royal Astronomical Society*, 460(1):434–457, July 2016.

Harnois-Déraps, J. et al. KiDS-450: tomographic cross-correlation of galaxy shear with Planck lensing. *Monthly Notices of the Royal Astronomical Society*, 471(2): 1619–1633, October 2017.

Harrison, E.R. Fluctuations at the Threshold of Classical Cosmology. *Physical Review D*, 1(10):2726–2730, May 1970.

Hasselfield, M. et al. The Atacama Cosmology Telescope: Sunyaev-Zel'dovich selected galaxy clusters at 148 GHz from three seasons of data. *Journal of Cosmology and Astro-Particle Physics*, 2013:008, 2013.

Henson, M.A. et al. The impact of baryons on massive galaxy clusters: halo structure and cluster mass estimates. *Monthly Notices of the Royal Astronomical Society*, 465 (3):3361–3378, March 2017.

Heymans, C. et al. CFHTLenS: the Canada-France-Hawaii Telescope Lensing Survey. *Monthly Notices of the Royal Astronomical Society*, 427(1):146–166, November 2012.

Heymans, C. et al. CFHTLenS tomographic weak lensing cosmological parameter constraints: Mitigating the impact of intrinsic galaxy alignments. *Monthly Notices of the Royal Astronomical Society*, 432(3):2433–2453, July 2013.

High, F.W. et al. Weak-lensing Mass Measurements of Five Galaxy Clusters in the South Pole Telescope Survey Using Magellan/Megacam. *Astrophysical Journal*, 758:68, 2012.

Hikage, C. et al. Cosmology from cosmic shear power spectra with Subaru Hyper Suprime-Cam first-year data. *Publications of the Astronomical Society of Japan*, 71(2):43, April 2019.

Hildebrandt, H. et al. KiDS-450: cosmological parameter constraints from tomographic weak gravitational lensing. *Monthly Notices of the Royal Astronomical Society*, 465(2):1454–1498, February 2017.

Hildebrandt, H. et al. KiDS+VIKING-450: Cosmic shear tomography with optical+infrared data. *arXiv e-prints*, art. arXiv:1812.06076, December 2018.

Hill, J.C. and Spergel, D.N. Detection of thermal SZ-CMB lensing cross-correlation in Planck nominal mission data. *Journal of Cosmology and Astroparticle Physics*, 2014(2):030, February 2014.

Hilton, M. and ACT Collaboration. The Atacama Cosmology Telescope: A Catalog of 1500+ Sunyaev-Zel'dovich Effect Selected Galaxy Clusters from the AdvACT 14,000 Square Degrees Survey. in prep.

Hirata, C. and Seljak, U. Shear calibration biases in weak-lensing surveys. *Monthly Notices of the Royal Astronomical Society*, 343(2):459–480, August 2003.

Hirata, C.M. and Seljak, U. Intrinsic alignment-lensing interference as a contaminant of cosmic shear. *Physical Review D*, 70(6):063526, September 2004.

Hirata, C.M. et al. Correlation of CMB with large-scale structure. II. Weak lensing. *Physical Review D*, 78(4):043520, August 2008.

Hivon, E. et al. MASTER of the Cosmic Microwave Background Anisotropy Power Spectrum: A Fast Method for Statistical Analysis of Large and Complex Cosmic Microwave Background Data Sets. *Astrophysical Journal*, 567(1):2–17, Mar 2002.

Hoekstra, H. et al. The Canadian Cluster Comparison Project: detailed study of systematics and updated weak lensing masses. *Monthly Notices of the Royal Astronomical Society*, 449(1):685–714, May 2015.

Hofmann, F. et al. eROSITA cluster cosmology forecasts: Cluster temperature substructure bias. *Astronomy and Astrophysics*, 606:A118, October 2017.

Hojjati, A. et al. Cross-correlating Planck tSZ with RCSLenS weak lensing: implications for cosmology and AGN feedback. *Monthly Notices of the Royal Astronomical Society*, 471(2):1565–1580, October 2017.

Holder, G.P. et al. A Cosmic Microwave Background Lensing Mass Map and Its Correlation with the Cosmic Infrared Background. *Astrophysical Journal, Letters*, 771(1):L16, July 2013.

Holder, G., Haiman, Z. and Mohr, J.J. Constraints on $\Omega_m$, $\Omega_\Lambda$, and $\sigma_8$ from Galaxy Cluster Redshift Distributions. *Astrophysical Journal, Letters*, 560(2):L111–L114, October 2001.

Hu, W. Dark synergy: Gravitational lensing and the CMB. *Physical Review D*, 65 (2):023003, January 2002.

Hu, W. and Okamoto, T. Mass Reconstruction with Cosmic Microwave Background Polarization. *Astrophysical Journal*, 574(2):566–574, August 2002.

Humphreys, E.M.L. et al. Toward a New Geometric Distance to the Active Galaxy NGC 4258. III. Final Results and the Hubble Constant. *Astrophysical Journal*, 775 (1):13, September 2013.

Ilbert, O. et al. Accurate photometric redshifts for the CFHT legacy survey calibrated using the VIMOS VLT deep survey. *Astronomy and Astrophysics*, 457(3):841–856, October 2006.

Ilbert, O. et al. Cosmos Photometric Redshifts with 30-Bands for 2-deg$^2$. *Astrophysical Journal*, 690(2):1236–1249, January 2009.

Itoh, N., Kohyama, Y. and Nozawa, S. Relativistic Corrections to the Sunyaev-Zel'dovich Effect for Clusters of Galaxies. *Astrophysical Journal*, 502(1):7–15, July 1998.

Ivezić, Ž. et al. LSST: From Science Drivers to Reference Design and Anticipated Data Products. *Astrophysical Journal*, 873(2):111, Mar 2019.

Jee, M.J. et al. Weighing "El Gordo" with a Precision Scale: Hubble Space Telescope Weak-lensing Analysis of the Merging Galaxy Cluster ACT-CL J0102-4915 at z = 0.87. *Astrophysical Journal*, 785:20, 2014.

Johnston, H. et al. KiDS+GAMA: Intrinsic alignment model constraints for current and future weak lensing cosmology. *Astronomy and Astrophysics*, 624:A30, April 2019.

Joudaki, S. et al. KiDS+VIKING-450 and DES-Y1 combined: Cosmology with cosmic shear. *arXiv e-prints*, art. arXiv:1906.09262, June 2019.

Joudaki, S. et al. KiDS-450: testing extensions to the standard cosmological model. *Monthly Notices of the Royal Astronomical Society*, 471(2):1259–1279, October 2017.

Kaiser, N. Evolution and clustering of rich clusters. *Monthly Notices of the Royal Astronomical Society*, 222:323–345, September 1986.

Kaiser, N. Evolution of Clusters of Galaxies. *Astrophysical Journal*, 383:104, December 1991.

Kaiser, N. and Squires, G. Mapping the Dark Matter with Weak Gravitational Lensing. *Astrophysical Journal*, 404:441, Feb 1993.

Kaiser, N., Squires, G. and Broadhurst, T. A Method for Weak Lensing Observations. *Astrophysical Journal*, 449:460, August 1995.

Keisler, R. et al. Measurements of Sub-degree B-mode Polarization in the Cosmic Microwave Background from 100 Square Degrees of SPTpol Data. *Astrophysical Journal*, 807(2):151, July 2015.

Kilbinger, M. Cosmology with cosmic shear observations: a review. *Reports on Progress in Physics*, 78(8):086901, Jul 2015.

Kirk, D. et al. Cross-correlation of gravitational lensing from DES Science Verification data with SPT and Planck lensing. *Monthly Notices of the Royal Astronomical Society*, 459(1):21–34, June 2016.

Kirk, D. et al. Galaxy Alignments: Observations and Impact on Cosmology. *Space Science Reviews*, 193(1-4):139–211, November 2015.

Kodama, Y. et al. Gamma-ray bursts in 1.8 < z < 5.6 suggest that the time variation of the dark energy is small. *Monthly Notices of the Royal Astronomical Society*, 391(1):L1–L4, November 2008.

Komatsu, E. and Seljak, U. The Sunyaev-Zel'dovich angular power spectrum as a probe of cosmological parameters. *Monthly Notices of the Royal Astronomical Society*, 336(4):1256–1270, November 2002.

Komatsu, E. and Kitayama, T. Sunyaev-Zel'dovich Fluctuations from Spatial Correlations between Clusters of Galaxies. *Astrophysical Journal, Letters*, 526(1):L1–L4, November 1999.

Kuijken, K. et al. The fourth data release of the Kilo-Degree Survey: ugri imaging and nine-band optical-IR photometry over 1000 square degrees. *Astronomy and Astrophysics*, 625:A2, May 2019.

Leauthaud, A. et al. Lensing is low: cosmology, galaxy formation or new physics? *Monthly Notices of the Royal Astronomical Society*, 467(3):3024–3047, May 2017.

Lemaître, G. L'Univers en expansion. *Annales de Société scientifique de Bruxelles*, 53:51, January 1933.

Lesgourgues, J. The Cosmic Linear Anisotropy Solving System (CLASS) I: Overview. *arXiv e-prints*, art. arXiv:1104.2932, April 2011.

Lesgourgues, J. and Pastor, S. Massive neutrinos and cosmology. *Physics Reports*, 429(6):307–379, July 2006.

Lewis, A. and Challinor, A. Weak gravitational lensing of the CMB. *Physics Reports*, 429(1):1–65, June 2006.

Liddle, A. *An Introduction to Modern Cosmology, Second Edition*. 2003.

Liddle, A.R. and Scherrer, R.J. Classification of scalar field potentials with cosmological scaling solutions. *Physical Review D*, 59(2):023509, January 1999.

Liu, J. and Hill, J.C. Cross-correlation of Planck CMB lensing and CFHTLenS galaxy weak lensing maps. *Physical Review D*, 92(6):063517, September 2015.

López-Caniego, M. et al. The QUIJOTE CMB Experiment: status and first results with the multi-frequency instrument. *arXiv e-prints*, art. arXiv:1401.4690, January 2014.

Louis, T. et al. The Atacama Cosmology Telescope: cross correlation with Planck maps. *Journal of Cosmology and Astroparticle Physics*, 2014(7):016, July 2014.

Louis, T. et al. The Atacama Cosmology Telescope: two-season ACTPol spectra and parameters. *Journal of Cosmology and Astroparticle Physics*, 2017(6):031, June 2017.

Lyth, D.H. and Liddle, A.R. *The Primordial Density Perturbation*. 2009.

MacCrann, N. et al. Cosmic discordance: are Planck CMB and CFHTLenS weak lensing measurements out of tune? *Monthly Notices of the Royal Astronomical Society*, 451(3):2877–2888, August 2015.

Madhavacheril, M.S. and Hill, J.C. Mitigating foreground biases in cmb lensing reconstruction using cleaned gradients. *Physical Review D*, 98:023534, Jul 2018.

Mandelbaum, R. et al. Systematic errors in weak lensing: application to SDSS galaxy-galaxy weak lensing. *Monthly Notices of the Royal Astronomical Society*, 361(4): 1287–1322, August 2005.

Mandelbaum, R. et al. Weak lensing shear calibration with simulations of the HSC survey. *Monthly Notices of the Royal Astronomical Society*, 481(3):3170–3195, Decemberember 2018.

Mantz, A.B. et al. Cosmology and astrophysics from relaxed galaxy clusters - II. Cosmological constraints. *Monthly Notices of the Royal Astronomical Society*, 440: 2077–2098, May 2014.

Mantz, A.B. et al. Weighing the giants - IV. Cosmology and neutrino mass. *Monthly Notices of the Royal Astronomical Society*, 446:2205–2225, 2015.

Marriage, T. et al. In *American Astronomical Society Meeting Abstracts #223*, volume 223 of *American Astronomical Society Meeting Abstracts*, page 245.15, January 2014.

Mather, J.C. et al. A Preliminary Measurement of the Cosmic Microwave Background Spectrum by the Cosmic Background Explorer (COBE) Satellite. *Astrophysical Journal, Letters*, 354:L37, May 1990.

McInnes, R.N. et al. First lensing measurements of SZ-detected clusters. *Monthly Notices of the Royal Astronomical Society*, 399:L84–L88, 2009.

Medezinski, E. et al. Planck Sunyaev-Zel'dovich cluster mass calibration using Hyper Suprime- Cam weak lensing. *Publications of the Astronomical Society of Japan*, 70: S28, 2018.

Mehrtens, N. et al. The XMM Cluster Survey: optical analysis methodology and the first data release. *Monthly Notices of the Royal Astronomical Society*, 423(2): 1024–1052, June 2012.

Meszaros, P. The behaviour of point masses in an expanding cosmological substratum. *Astronomy and Astrophysics*, 37(2):225–228, December 1974.

Miller, L. et al. Bayesian galaxy shape measurement for weak lensing surveys - III. Application to the Canada-France-Hawaii Telescope Lensing Survey. *Monthly Notices of the Royal Astronomical Society*, 429(4):2858–2880, March 2013.

Miyatake, H. et al. Subaru weak lensing measurement of a z = 0.81 cluster discovered by the Atacama Cosmology Telescope Survey. *Monthly Notices of the Royal Astronomical Society*, 429:3627–3644, 2013.

Miyatake, H. et al. Weak-lensing Mass Calibration of ACTPol SunyaevZel'dovich Clusters with the Hyper Suprime-Cam Survey. *Astrophysical Journal*, 875(1):63, Apr 2019.

Mo, H.J. and White, S.D.M. An analytic model for the spatial clustering of dark matter haloes. *Monthly Notices of the Royal Astronomical Society*, 282(2):347–361, September 1996.

Naess, S. and ACT Collaboration. Combined CMB maps from ACT and Planck. in prep.

Naess, S. et al. The Atacama Cosmology Telescope: CMB polarization at 200 < l < 9000. *Journal of Cosmology and Astroparticle Physics*, 2014(10):007, October 2014.

Nagai, D. The Impact of Galaxy Formation on the Sunyaev-Zel'dovich Effect of Galaxy Clusters. *Astrophysical Journal*, 650(2):538–549, October 2006.

Namikawa, T. et al. Evidence for the Cross-correlation between Cosmic Microwave Background Polarization Lensing from Polarbear and Cosmic Shear from Subaru Hyper Suprime-Cam. *Astrophysical Journal*, 882(1):62, September 2019.

Navarro, J.F., Frenk, C.S. and White, S.D.M. A Universal Density Profile from Hierarchical Clustering. *Astrophysical Journal*, 490(2):493–508, December 1997.

Omori, Y. and Holder, G. Cross-Correlation of CFHTLenS Galaxy Number Density and Planck CMB Lensing. *arXiv e-prints*, art. arXiv:1502.03405, February 2015.

Omori, Y. et al. Dark Energy Survey Year 1 Results: Cross-correlation between Dark Energy Survey Y1 galaxy weak lensing and South Pole Telescope+P l a n c k CMB weak lensing. *Physical Review D*, 100(4):043517, Aug 2019a.

Omori, Y. et al. Dark Energy Survey Year 1 Results: Tomographic cross-correlations between Dark Energy Survey galaxies and CMB lensing from South Pole Telescope +Planck. *Physical Review D*, 100(4):043501, Aug 2019b.

Peacock, J.A. *Cosmological Physics*. 1999.

Peebles, P.J. and Ratra, B. The cosmological constant and dark energy. *Reviews of Modern Physics*, 75(2):559–606, April 2003.

Peebles, P.J.E. Primordial Helium Abundance and the Primordial Fireball. II. *Astrophysical Journal*, 146:542, November 1966.

Peebles, P.J.E. Recombination of the Primeval Plasma. *Astrophysical Journal*, 153: 1, July 1968.

Peebles, P.J.E. Statistical Analysis of Catalogs of Extragalactic Objects. I. Theory. *Astrophysical Journal*, 185:413–440, October 1973.

Peebles, P.J.E. *The large-scale structure of the universe*. 1980.

Peebles, P.J.E. and Yu, J.T. Primeval Adiabatic Perturbation in an Expanding Universe. *Astrophysical Journal*, 162:815, December 1970.

Peebles, P.J.E., Daly, R.A. and Juszkiewicz, R. The Masses of Rich Clusters of Galaxies as a Test of the Biased Cold Dark Matter Theory. *Astrophysical Journal*, 347:563, December 1989.

Penna-Lima, M. et al. Calibrating the Planck cluster mass scale with CLASH. *Astronomy and Astrophysics*, 604:A89, 2017.

Penzias, A.A. and Wilson, R.W. A Measurement of Excess Antenna Temperature at 4080 Mc/s. *Astrophysical Journal*, 142:419–421, July 1965.

Perlmutter, S. et al. Measurements of $\Omega$ and $\Lambda$ from 42 High-Redshift Supernovae. *Astrophysical Journal*, 517(2):565–586, June 1999.

Planck Collaboration. Planck 2015 results. XXIV. Cosmology from Sunyaev-Zeldovich cluster counts. *Astronomy and Astrophysics*, 594:A24, September 2016.

Planck Collaboration. Planck 2018 results. VI. Cosmological parameters. *arXiv e-prints*, art. arXiv:1807.06209, July 2018.

Polarbear Collaboration et al. A Measurement of the Cosmic Microwave Background B-mode Polarization Power Spectrum at Sub-degree Scales with POLARBEAR. *Astrophysical Journal*, 794(2):171, October 2014.

Polnarev, A.G. Polarization and Anisotropy Induced in the Microwave Background by Cosmological Gravitational Waves. *Soviet Astronomy*, 29:607–613, December 1985.

Prat, J. et al. Dark Energy Survey year 1 results: Galaxy-galaxy lensing. *Physical Review D*, 98(4):042005, August 2018.

Pratt, G.W. et al. The Galaxy Cluster Mass Scale and Its Impact on Cosmological Constraints from the Cluster Population. *Space Science Reviews*, 215(2):25, February 2019.

Rees, M.J. and Sciama, D.W. Large-scale Density Inhomogeneities in the Universe. *Nature*, 217(5128):511–516, February 1968.

Remazeilles, M. et al. Can we neglect relativistic temperature corrections in the Planck thermal SZ analysis? *Monthly Notices of the Royal Astronomical Society*, 483(3):3459–3464, March 2019.

Rephaeli, Y. Comptonization Of The Cosmic Microwave Background: The Sunyaev-Zeldovich Effect. *Annual Review of Astronomy and Astrophysics*, 33:541–580, January 1995.

Riess, A.G. et al. A 2.4% Determination of the Local Value of the Hubble Constant. *Astrophysical Journal*, 826(1):56, July 2016.

Robertson, H.P. Kinematics and World-Structure. *Astrophysical Journal*, 82:284, November 1935.

Rozo, E. et al. Cosmological Constraints from the Sloan Digital Sky Survey maxBCG Cluster Catalog. *Astrophysical Journal*, 708:645–660, 2010.

Rubin, V.C., Ford, W. K., J. and Thonnard, N. Rotational properties of 21 SC galaxies with a large range of luminosities and radii, from NGC 4605 (R=4kpc) to UGC 2885 (R=122kpc). *Astrophysical Journal*, 238:471–487, June 1980.

Sachs, R.K. and Wolfe, A.M. Perturbations of a Cosmological Model and Angular Variations of the Microwave Background. *Astrophysical Journal*, 147:73, January 1967.

Schaan, E. et al. Looking through the same lens: Shear calibration for LSST, Euclid, and WFIRST with stage 4 CMB lensing. *Physical Review D*, 95(12):123512, June 2017.

Schmidt, B.P. et al. The High-Z Supernova Search: Measuring Cosmic Deceleration and Global Curvature of the Universe Using Type IA Supernovae. *Astrophysical Journal*, 507(1):46–63, November 1998.

Schmitz, H.A. In *2nd Crisis in Cosmology Conference*, volume 413 of *Astronomical Society of the Pacific Conference Series*, page 98, December 2009.

Schrabback, T. et al. Cluster mass calibration at high redshift: HST weak lensing analysis of 13 distant galaxy clusters from the South Pole Telescope Sunyaev-Zel'dovich Survey. *Monthly Notices of the Royal Astronomical Society*, 474:2635–2678, 2018.

Sehgal, N. et al. The Atacama Cosmology Telescope: Cosmology from Galaxy Clusters Detected via the Sunyaev-Zel'dovich Effect. *Astrophysical Journal*, 732:44, May 2011.

Seljak, U. Analytic model for galaxy and dark matter clustering. *Monthly Notices of the Royal Astronomical Society*, 318(1):203–213, October 2000.

Sereno, M. et al. PSZ2LenS. Weak lensing analysis of the Planck clusters in the CFHTLenS and in the RCSLenS. *Monthly Notices of the Royal Astronomical Society*, 472:1946–1971, 2017.

Sheldon, E.S. et al. The Galaxy-Mass Correlation Function Measured from Weak Lensing in the Sloan Digital Sky Survey. *The Astronomical Journal*, 127(5):2544–2564, May 2004.

Sherwin, B.D. et al. The Atacama Cosmology Telescope: Cross-correlation of cosmic microwave background lensing and quasars. *Physical Review D*, 86(8):083006, October 2012.

Sherwin, B.D. et al. Two-season Atacama Cosmology Telescope polarimeter lensing power spectrum. *Physical Review D*, 95(12):123529, June 2017.

Sifón, C. et al. The Atacama Cosmology Telescope: Dynamical Masses and Scaling Relations for a Sample of Massive Sunyaev-Zel'dovich Effect Selected Galaxy Clusters. *Astrophysical Journal*, 772(1):25, July 2013.

Sifón, C. et al. The galaxy-subhalo connection in low-redshift galaxy clusters from weak gravitational lensing. *Monthly Notices of the Royal Astronomical Society*, 478 (1):1244–1264, July 2018.

Singh, S. et al. Galaxy-galaxy lensing estimators and their covariance properties. *Monthly Notices of the Royal Astronomical Society*, 471(4):3827–3844, November 2017.

Smith, K.M., Zahn, O. and Doré, O. Detection of gravitational lensing in the cosmic microwave background. *Physical Review D*, 76(4):043510, August 2007.

Smith, R.E. et al. Stable clustering, the halo model and non-linear cosmological power spectra. *Monthly Notices of the Royal Astronomical Society*, 341(4):1311–1332, June 2003.

Smoot, G.F. et al. Structure in the COBE Differential Microwave Radiometer First-Year Maps. *Astrophysical Journal, Letters*, 396:L1, September 1992.

Spergel, D.N. et al. First-Year Wilkinson Microwave Anisotropy Probe (WMAP) Observations: Determination of Cosmological Parameters. *Astrophysical Journal, Supplement*, 148(1):175–194, September 2003.

Springel, V. et al. Simulations of the formation, evolution and clustering of galaxies and quasars. *Nature*, 435(7042):629–636, June 2005.

Starobinskiĭ, A.A. Spectrum of relict gravitational radiation and the early state of the universe. *Soviet Journal of Experimental and Theoretical Physics Letters*, 30: 682, December 1979.

Stern, C. et al. Weak-lensing analysis of SPT-selected galaxy clusters using Dark Energy Survey Science Verification data. *Monthly Notices of the Royal Astronomical Society*, 485(1):69–87, May 2019.

Stompor, R. and Efstathiou, G. Gravitational lensing of cosmic microwave background anisotropies and cosmological parameter estimation. *Monthly Notices of the Royal Astronomical Society*, 302(4):735–747, February 1999.

Sunyaev, R.A. and Zeldovich, Y.B. Small-Scale Fluctuations of Relic Radiation. *Astrophysics and Space Science*, 7(1):3–19, April 1970.

Sunyaev, R.A. and Zel'dovich, Y.B. The Observations of Relic Radiation as a Test of the Nature of X-Ray Radiation from the Clusters of Galaxies. *Comments on Astrophysics and Space Physics*, 4:173, November 1972.

Szapudi, I., Prunet, S. and Colombi, S. Fast Analysis of Inhomogenous Megapixel Cosmic Microwave Background Maps. *Astrophysical Journal*, 561(1):L11–L14, November 2001.

Takahashi, R. et al. Revising the Halofit Model for the Nonlinear Matter Power Spectrum. *Astrophysical Journal*, 761(2):152, December 2012.

Taylor, J.F., Ashdown, M.A.J. and Hobson, M.P. Fast optimal CMB power spectrum estimation with Hamiltonian sampling. *Monthly Notices of the Royal Astronomical Society*, 389(3):1284–1292, September 2008.

Tegmark, M. How to measure CMB power spectra without losing information. *Physical Review D*, 55(10):5895–5907, May 1997.

Tegmark, M. and de Oliveira-Costa, A. How to measure CMB polarization power spectra without losing information. *Physical Review D*, 64(6):063001, September 2001.

Tristram, M. et al. XSPECT, estimation of the angular power spectrum by computing cross-power spectra with analytical error bars. *Monthly Notices of the Royal Astronomical Society*, 358(3):833–842, April 2005.

Troxel, M.A. et al. Dark Energy Survey Year 1 results: Cosmological constraints from cosmic shear. *Physical Review D*, 98(4):043528, August 2018.

Vallinotto, A. The Synergy between the Dark Energy Survey and the South Pole Telescope. *Astrophysical Journal*, 778(2):108, December 2013.

van Engelen, A. et al. The Atacama Cosmology Telescope: Lensing of CMB Temperature and Polarization Derived from Cosmic Infrared Background Cross-correlation. *Astrophysical Journal*, 808(1):7, July 2015.

van Uitert, E. and Joachimi, B. Intrinsic alignment of redMaPPer clusters: cluster shape-matter density correlation. *Monthly Notices of the Royal Astronomical Society*, 468(4):4502–4512, July 2017.

Van Waerbeke, L. et al. Detection of correlated galaxy ellipticities from CFHT data: first evidence for gravitational lensing by large-scale structures. *Astronomy and Astrophysics*, 358:30–44, June 2000.

Van Waerbeke, L. et al. CFHTLenS: mapping the large-scale structure with gravitational lensing. *Monthly Notices of the Royal Astronomical Society*, 433(4):3373–3388, August 2013.

Van Waerbeke, L., Hinshaw, G. and Murray, N. Detection of warm and diffuse baryons in large scale structure from the cross correlation of gravitational lensing and the thermal Sunyaev-Zel'dovich effect. *Physical Review D*, 89(2):023508, January 2014.

Vanderlinde, K. et al. Galaxy Clusters Selected with the Sunyaev-Zel'dovich Effect from 2008 South Pole Telescope Observations. *Astrophysical Journal*, 722:1180–1196, 2010.

Vanneste, S. et al. Quadratic estimator for CMB cross-correlation. *Physical Review D*, 98(10):103526, November 2018.

Velander, M. et al. CFHTLenS: the relation between galaxy dark matter haloes and baryons from weak gravitational lensing. *Monthly Notices of the Royal Astronomical Society*, 437(3):2111–2136, January 2014.

Vikhlinin, A. et al. Chandra Cluster Cosmology Project III: Cosmological Parameter Constraints. *Astrophysical Journal*, 692:1060–1074, 2009.

Voit, G.M. Tracing cosmic evolution with clusters of galaxies. *Reviews of Modern Physics*, 77:207–258, 2005.

von der Linden, A. et al. Robust weak-lensing mass calibration of Planck galaxy clusters. *Monthly Notices of the Royal Astronomical Society*, 443:1973–1978, 2014.

Wagoner, R.V., Fowler, W.A. and Hoyle, F. On the Synthesis of Elements at Very High Temperatures. *Astrophysical Journal*, 148:3, April 1967.

Walker, A.G. On Milne's Theory of World-Structure. *Proceedings of the London Mathematical Society*, 42:90–127, January 1937.

Wandelt, B.D. and Hansen, F.K. Fast, exact CMB power spectrum estimation for a certain class of observational strategies. *Physical Review D*, 67(2):023001, January 2003.

Wandelt, B.D., Hivon, E. and Górski, K.M. Cosmic microwave background anisotropy power spectrum statistics for high precision cosmology. *Physical Review D*, 64(8): 083003, October 2001.

Weinberg, S. The cosmological constant problem. *Reviews of Modern Physics*, 61(1): 1–23, January 1989.

Wittman, D.M. et al. Detection of weak gravitational lensing distortions of distant galaxies by cosmic dark matter at large scales. *Nature*, 405(6783):143–148, May 2000.

Wright, A.H. et al. KiDS+VIKING-450: A new combined optical & near-IR dataset for cosmology and astrophysics. *arXiv e-prints*, art. arXiv:1812.06077, December 2018.

Wright, C.O. and Brainerd, T.G. Gravitational Lensing by NFW Halos. *Astrophysical Journal*, 534(1):34–40, May 2000.

Zaldarriaga, M. and Seljak, U. All-sky analysis of polarization in the microwave background. *Physical Review D*, 55(4):1830–1840, February 1997.

Zel'dovich, Y.B. Reprint of Gravitational instability: an approximate theory for large density perturbations. *Astronomy and Astrophysics*, 500:13–18, Mar 1970.

Zel'dovich, Y.B., Kurt, V.G. and Syunyaev, R.A. Recombination of Hydrogen in the Hot Model of the Universe. *Soviet Journal of Experimental and Theoretical Physics*, 28:146, January 1969.

Zel'dovich, Y.B. A hypothesis, unifying the structure and the entropy of the Universe. *Monthly Notices of the Royal Astronomical Society*, 160:1P, January 1972.

Zhai, Z. et al. The Clustering of Luminous Red Galaxies at z  0.7 from EBOSS and BOSS Data. *Astrophysical Journal*, 848(2):76, October 2017.

Zhang, Y. et al. Dark Energy Surveyed Year 1 results: calibration of cluster mis-centring in the redMaPPer catalogues. *Monthly Notices of the Royal Astronomical Society*, 487(2):2578–2593, August 2019.

Zwicky, F. Die Rotverschiebung von extragalaktischen Nebeln. *Helvetica Physica Acta*, 6:110–127, January 1933.

Zwicky, F. On the Masses of Nebulae and of Clusters of Nebulae. *Astrophysical Journal*, 86:217, October 1937.